DEVELOPMENT OF LABEL-FREE COLORIMETRIC PLASMONIC SENSOR FOR BIOMEDICAL APPLICATIONS

BY

ABID AMEEN

DISSERTATION

Submitted in partial fulfillment of the requirements
for the degree of Doctor of Philosophy in Materials Science and Engineering
in the Graduate College of the
University of Illinois at Urbana-Champaign, 2017

Urbana, Illinois

Doctoral Committee

Professor John A. Rogers, Chair
Associate Professor Gang Logan Liu, Director of Research
Professor Jian-Min Zuo
Associate Professor Shen J. Dillon

ABSTRACT

Biosensor technology is making strides due to its association with detection and quantification of a wide array of physiological profile makers, biomarkers, for the early detection of diseases. The newest technologies encompasses both qualitative as well as quantitative measurement of such markers. Colorimetric sensing, a method that enables the detection of target analytes via 'color change', lays the foundation of a user-friendly, economical and most of all, it's accessibility to draw inference for the detection of notorious critical conditions such as, carcinomas, and other significant environmental monitoring. Therefore, the impact of colorimetric sensing on the clinical detection of diseases at earlier stages can be enormous, provided the gap between the accuracy of lab-equipment to point-of-care testing tools is approximated. This thesis discusses the design, fabrication and characterization of a label-free plasmonic-based colorimetric sensor on a flexible plastic substrate consisting of periodic nano cups, also referred a nano Lycurgus cups, in an array covered with metal nanoparticles on the side walls and have sub-wavelength openings to provide refractive index sensing. It is also anticipated that the colorimetric sensor can be applied to point-of-care diagnostics by utilizing proper surface functionalization techniques, which is one of the current limiting factors.

Chapter 1, is an overview on the existing biosensor technologies with the requirement of the next generation label free biosensor based on nanohole arrays. Chapter 2, describes the recent development of nanoscale Lycurgus cup Array (nanoLCA) with design, fabrication and characterization of the nanoplasmonic device. Chapter 3 starts with the discussion on the influence of adhesion layer on the optical properties of the nanoLCA device followed by layer by layer deposition of polyelectrolyte layers to identify the decay length of the device. Furthermore, this

chapter also describes the deposition of different polymers using micro contact printing and compares the spectral results with the colorimetric properties of the device. Chapter 4 gives a demonstration of detection of drug bindings with cytochrome P450-2J2 using the nanoLCA device. Cytochrome P450-2J2 is the most common enzyme found in human heart and it is involved in drug metabolism. All bio-molecular detections are done using nanoLCA based on the shift in resonance peak wavelength with respect to change in the refractive index on the surrounding medium of the device. However, there is a constraint in using nanoLCA device to detect the lower concentration of bio-marker. Therefore, in Chapter 5, we have introduced 3D plasmonic nano cavity structure of the device in which an optical resonant cavity is combined with the plasmonic resonance in one device. This device is a modification of the previously studied nanoLCA device with additional layers, referred as multilayer nanoscale Lycurgus cup array (ML-nanoLCA device). The ML-nanoLCA device is based on a semiconductor material such as cadmium sulfide (CdS) layer, which has a high refractive index and very low extinction coefficient, sandwiched between two gold (Au) layers. This method allows intensity based bio-sensing with the help of a simple bandpass filter to allow certain wavelengths to be transmitted in the visible region at normal incidence illumination. The multilayer plasmonic substrate results in further improvement in the refractive-index sensing, DNA hybridization detection, protein-protein interaction, and detection of lower concentration of cancer biomarker, carcinoembryonic antigen (CEA) with higher sensitivity, which is discussed in chapter 6. The summary of the thesis with future outlook of the nanoplasmonic biosensor is discussed in chapter 7.

ACKNOWLEDGEMENT

I would like to express my sincere gratitude to Professor Gang Logan Liu, for his continual support and guidance in my doctoral research and preparation of this thesis. I am very thankful to him for introducing me to the exciting and interesting field of plasmonics. I am also grateful to my co-advisor Professor John A. Rogers for his guidance and support throughout my graduate student period. I would like to thank my dissertation committee members, Professor Jian-Min Zuo and Professor Shen Dilon for their helpful feedback. I would also like to thank my colleagues, Austin Hsiao, Manas Gartia, Sujin Seo, Lisa Plucinski, Xinhao Wang, Zhida Xu, Jing Jiang, Te-Wei Chang and Yemaya Bordain for their valuable suggestions to solve the problems during the research work. I would like to acknowledge the staff members of Materials Research Laboratory, Micro and Nanotechnology Laboratory, and the Beckman Institute at the University of Illinois at Urbana-Champaign. Last, but not least, I would like to acknowledge my parents for their understanding, love, support and encouragement throughout my life.

TABLE OF CONTENTS

CHAPTER 1

INTRODUCTION

1.1 Existing technologies and the next generation biosensors

The development in the field of genomics and proteomics significantly bridged the gap between the cascades of events that alter the physiology of normal cells leading to pathological states.[1, 2] Over the recent years, a wide array of physiological profile markers, known as 'biomarkers' are discovered that indicate any alteration beyond physiological cut-off limits, thus, serving as basis for 'early detection of diseases. It is very important to achieve the early detection of diseases. A report from the lung cancer foundation of US states that the cancer is one of the major cause of deaths in United states as more than half of the new patients are diagnosed with the cancer when the cancer is already spread and less than 10 percent of them survived for five years.[3] Another report from world health organization (WHO) predicts a significant increase in the number of patients diagnosed with cancer, from 14 million annually to 22 million within two decades.[4] This shows the gravity with which this problem needs to be addressed and the core to address this problem is to detect the lower concentration of the biomarker for analytes at earlier states. Earlier detection and treatment of the diseases improve the survival rate and maximize the quality of life for the patients.[5]

An overview of the existing technologies for biomolecular detection include the bench top models which has higher functionality and specificity systems such as Surface Plasmon-Resonance based sensors from GE healthcare and DNA sequencer to point-of-care sensors with lower sensitivity and functionality systems such as home pregnancy tester and blood glucometer. The

characteristics of the point-of-care sensors are to detect the single and relatively high concentration of analytes with the minimal sample preparation, handling and easy to read out the results either numerical or colorimetric. These kind of sensors are relatively inexpensive and can be operated by the end user as there is no specialized training is required to operate. However, these sensors cannot be used to detect the lower concentration of biomarker analytes because of lower sensitivity. On the other hand, bench top models can be used to detect multiple analytes with high sensitivity and high specificity, however, these systems are very expensive and can only be operated by the special trained personnel. Furthermore, these systems require additional sample preparation with the complex detection and analysis mechanism. Therefore, there is a high need for the next generation biosensors with whom the functionality similar to the bench top systems can be achieved through higher sensitivity and high specificity and at the same time it can improved the accessibility via portability, low cost and ease of use as indicated in Figure 1.1.

1.2 Label-free biosensors

Most biochemical assay or sensing methods require labels such as fluorescent, radioactive or enzymes (e.g. in enzyme-linked immunosorbent assays (ELISAs)) to detect biomolecules.[6] The label molecule is attached to the target molecule and it is the label molecule that is detected rather than the target molecule. Label-free sensing does not need any label but can directly detect the presence of target molecules.[7] One group of label-free method for biomolecular detection is based on the optical properties of biomolecules. Particularly, these sensors are operated how the light is interacted with the substrate and superstrate and other electromagnetic radiations and scatterings. These radiations and scatterings are typically in the wavelength range of visible to infrared range (i.e. 300 nanometers to 1000 nanometers) with specific biomolecules. When the

light is incident on the molecules which are attached to the surface of the sensor, there is a transient re-distribution of the charges occurred with the electric field component of the light. The electric field also polarize the molecules with the separation of positive and negative charges. This separation of charges induce secondary electric field which is opposite to the applied electric field which hinders the propagation of light through the molecules. Plasmonics take advantage of the coupling of light to bound charges like electrons in metals, and allow breaking the diffraction limit for the localization of light into subwavelength dimensions enabling strong field enhancements.[8] The shape of the nanoparticle extinction and scattering spectra, and in particular the peak wavelength λ_{max}, depends on the nanoparticle composition, size, shape, orientation and local dielectric environment so it can be used for sensing applications.[9] For the surface plasmon resonance (SPR) sensor, the peak wavelength at plasmon resonance is shifted by different refractive index of the environment but complicated instrumentation such as Otto setup, Kretschmann configuration, and spectrometer are required to detect the shift of the resonance peak.[10] Early in 1983, Liedberg, Nylander, and Lundström proposed using the plasmon sensor for label-free immunoassay.[11] In recent years, different types of sensors using surface plasmon have been implemented, including the surface plasmon resonance (SPR) sensor for cell adhesion studies [12], detection of metal ion [13] and clinical diagnosis of type I allergies [14]; localized surface plasmon resonance (LSPR) of a single particle for detection of proteins [15], colorimetric visualization of concentration of glucose [16] and colorimetric enzyme-linked immunosorbent assay [17]; surface enhanced Raman scattering (SERS) sensors for detection of DNA molecule[18], water contaminants[19], melamine[20] and yeast cells[21]. Compared to chemical-based sensors, surface plasmon-based sensors have the advantages of versatility, high sensitivity, reusability and a label-free property. Generally, surface plasmon sensors are divided into two

categories: localized surface plasmon sensor (LSPR), and propagating surface plasmon sensor (SPR). LSPR sensors are composed of discrete nanoparticles (ordered or random) either in solution or on solid substrates. In literature, several excellent review articles exist that deals with LSPR biosensor design, their underlying physics and application for sensing of biomolecules.[22-29] as shown in the Figure 1.2. Conventional prism coupled SPR sensors have already entered the realm of commercial market and detail of working principle can be found on recent literature reviews.[30, 31] Another form of SPR sensors involving extraordinary optical transmission (EOT) which is composed of periodic array of nanoholes, has been widely used for biosensing applications. Recently, nanohole sensors integrated with microfluidics using spectroscopic-based measurements has been reviewed.[32] Another recent review also deals with use of plasmonic sensors to point of care applications.[33]

1.3 Extraordinary optical transmission (EOT)

Ebbesen et al. was the first to propose extraordinary optical transmission (EOT) of light through subwavelength holes in silver films due to the excitation of surface plasmon resonance (SPR) as shown in Figure 1.3 (a).[34] The incident light coming from top first couple to SPR at the top due to the periodic hole array and then the light tunnels through the hole to couple to SPR at the bottom surface of metallic film. Finally, the light is reemitted from the bottom surface with multiple resonance peaks as shown in Figure 1.3 (b). The resonance peak position of the transmission spectrum at normal incidence can be approximately calculated using the surface plasmon dispersion relation as [35, 36]:

$$\lambda_{\max} = \frac{a_0}{\sqrt{i^2 + j^2}} \sqrt{\frac{\varepsilon_m \varepsilon_d}{\varepsilon_m + \varepsilon_d}} \quad \text{(square lattice)} \qquad (1)$$

$$\lambda_{\max} = \frac{a_0}{\sqrt{\frac{4}{3}\left(i^2 + ij + j^2\right)}} \sqrt{\frac{\varepsilon_m \varepsilon_d}{\varepsilon_m + \varepsilon_d}} \quad \text{(triangular lattice)} \qquad (2)$$

where a_0 is the period of the nanohole array, ε_m and ε_d are the permittivity of the metal and the dielectric material in contact with the metal respectively, and i and j are the scattering orders from the hole array. As shown in equation (1) and (2), the resonance peak position is proportional to the periodicity of the nanohole array. Hence, sensor resonance properties can be tuned by adjusting the periodicity of the hole array. For example, the color transmitted by the sensor can be tuned from blue to red by varying the periodicity of the nanoholes from 230 nm to 410 nm as shown in Figure 1.4 (a) and 1.4 (c). Figure 1.4 (b) shows a SEM image of the sensor with lattice constant of 330 nm and the corresponding microscopic image at the inset transmitting green light. With the increase in the distance between the holes (that is, increasing the lattice constant a_0), the transmission resonance peak are generally red shifted as shown in Figure 1.4 (d).

The theoretical research of EOT is still discussing the main mechanism to influence the optical properties of the nanohole array such as physical parameters, maximum transmission wavelength etc. through choice of metal, shape, size and pitch of nanohole array. There are several literature review articles on the nanohole arrays which particularly focused on design, fabrication, characterization and their applications.[37-41] As shown in Figure 1.3 (b), the EOT structures are associated with appearance of multiple peaks in the visible range due to coupling of resonances among holes and asymmetric boundary conditions (low dielectric materials like air on top, and high dielectric materials like glass/quartz at the bottom of the metallic film). For colorimetric sensor it is advantageous to have single peak. Generally, the diameter of the nanohole in the plasmonic devices is large, at least 100 nanometers, in comparison with the conventional solid

state nanoholes. The hole diameter is selected based on the application, but also selected because of the limitation in the fabrication procedure. Colloidal patterning is suitable if the desired diameter of the nanohole is lower than 100 nanometers, however, these kind of sensors application are not possible with plasmonic nanoholes.[42] As for the optical sensing, the nanohole diameter on the order 100 nanometers are preferable for better coupling efficiency of the incident light with the plasmon modes.[43]

In order to investigate the effect of dielectric constant of metal on the transmission efficiency of nanohole array which perform extraordinary transmission phenomenon, deposition of noble metals (such as Au, Ag and Cu) and transition metals (such as Co, Ni and W) can be performed.[44] Refractive index consist of two parts; i.e. real and imaginary part. As the noble metals have higher absolute value of the real part and lower value of the imaginary part of the refractive index, they have higher transmission efficiency as compare to the transmission metals for a given shape, size, periodicity and the thickness of metal deposition. These characteristics of the nanohole array for different metals are confirmed with the finite-difference time-domain (FDTD) simulation.[39]

1.4 Overview of thesis

In this thesis, I will first explain the design, fabrication and characterization of label free plasmonic nanohole array for biomedical application. In particular, different types of plasmonic sensors will be described in chapter 2, followed by the recent development of the nano Lycurgus cup array (nanoLCA) sensor and its characterization. In chapter 3, the influence of the substrate and superstrate of the physical material for the colorimetric and spectral sensing is studied. Also, in chapter 3, several surface based characterization, in particular, layer by layer deposition of

polyelectrolyte layers are deposited to measure the decay length of the device and micro contact printing of poly-L-lysine and different alkanethiols on the surface of the nanoLCA to study the colorimetric and spectral sensing. In chapter 4, detection of different drugs binding with cytochrome P450-2J2, which is the most common enzyme found in human heart is investigated using nanoLCA device. In chapter 5, a new device design of 3D plasmonic nano-cavity structure is introduced which allows to perform intensity based measurement instead the peak wavelength shift. Finally, in chapter 6, detection of the cancer biomarker, carcinoembriyonic antigen (CEA) using 3D plasmonic nano-cavity structure.

1.5 Figures

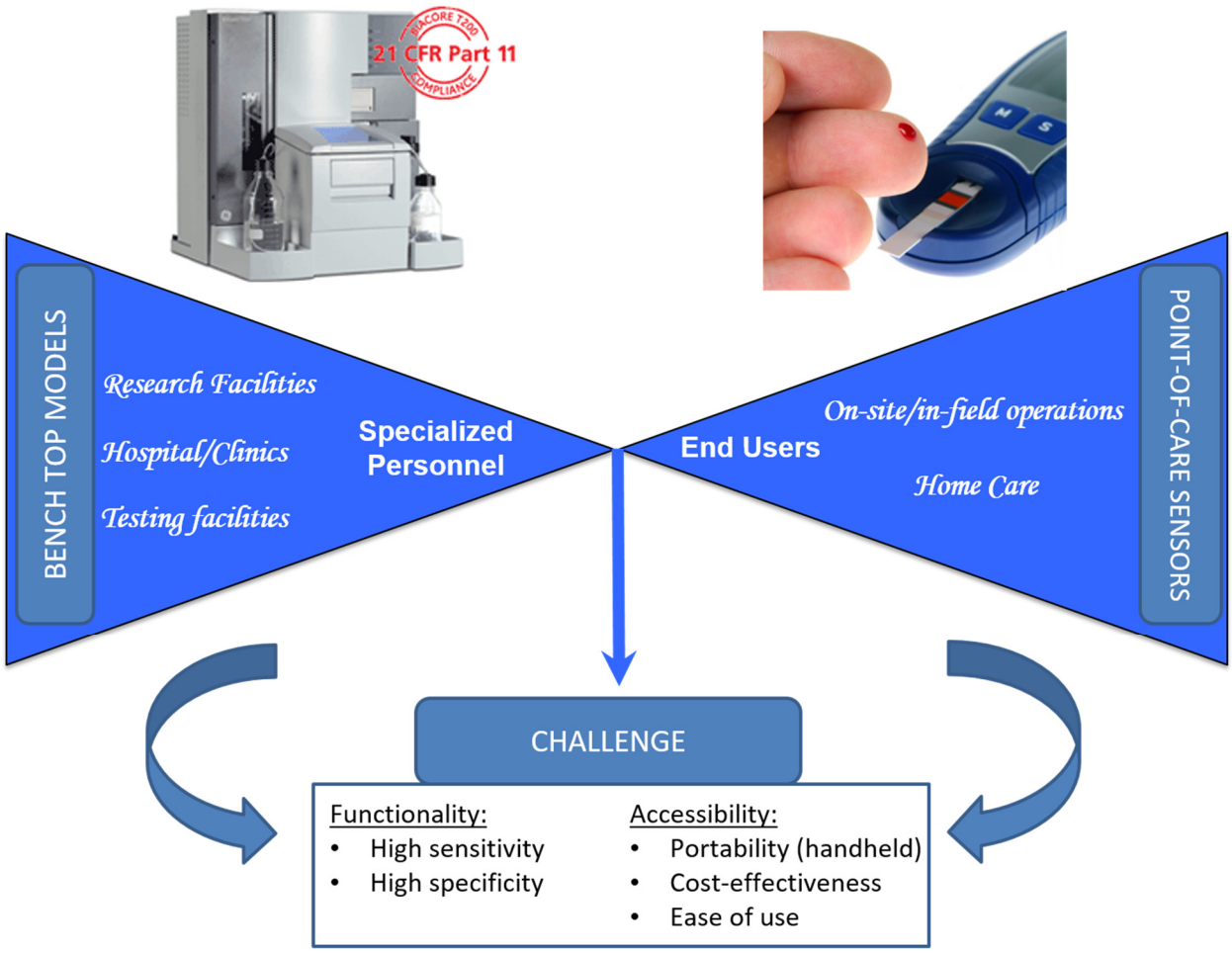

Figure 1.1 Existing technologies and the need for the next generation biosensor with high functionality and high accessibility for the earlier detection of diseases.

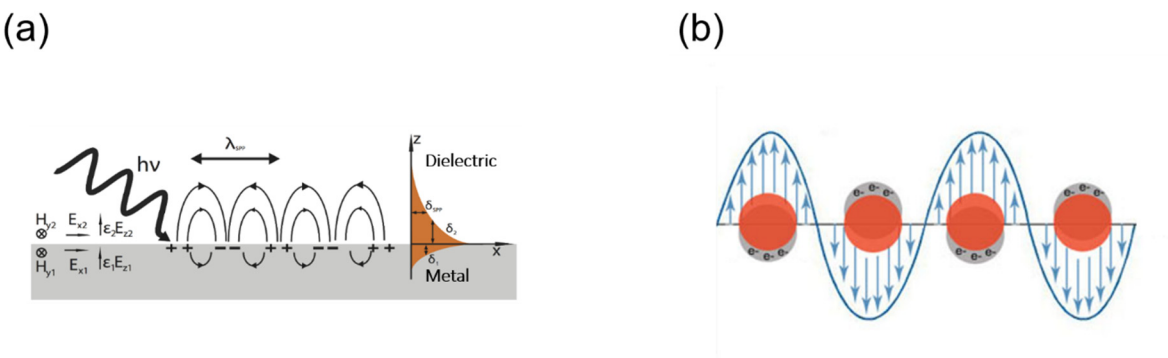

Figure 1.2 Schematic representation of the generation of (a) surface plasmon polaritons (SPPs) at metal and dielectric interface and (b) localized surface plasmon. Adapted from [45].

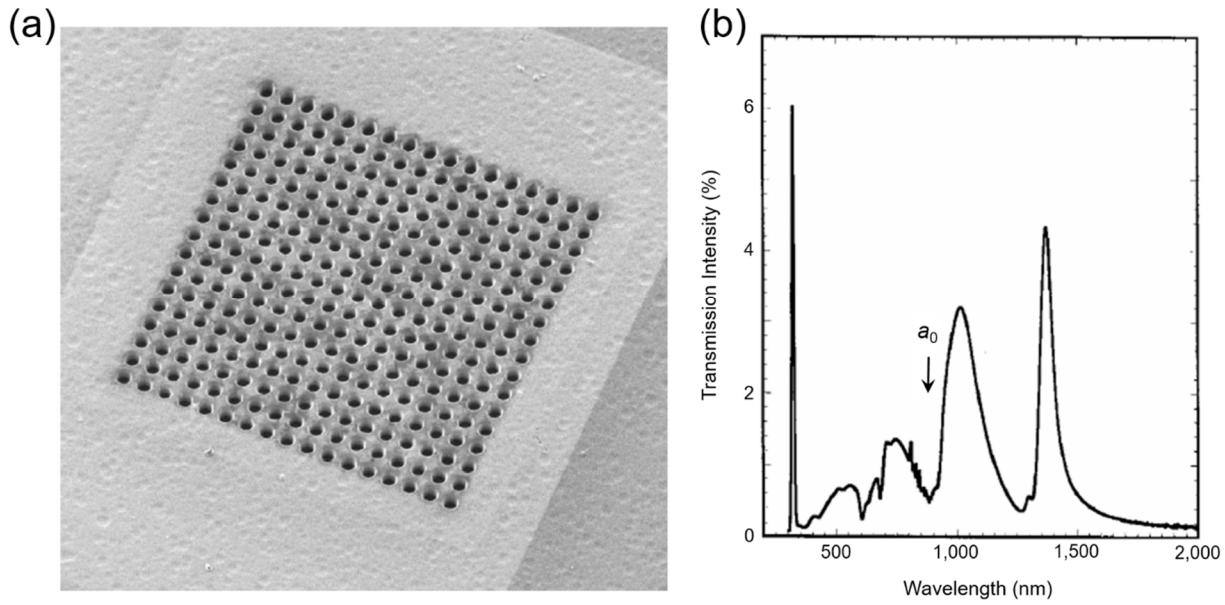

Figure 1.3 (a) Periodic nanohole arrays with square array of holes shows EOT.[34] (b) Transmission spectrum of EOT sensor using Ag film of thickness 200 nm, hole diameter 150 nm, and periodicity, a_0 = 900 nm.[41, 46]

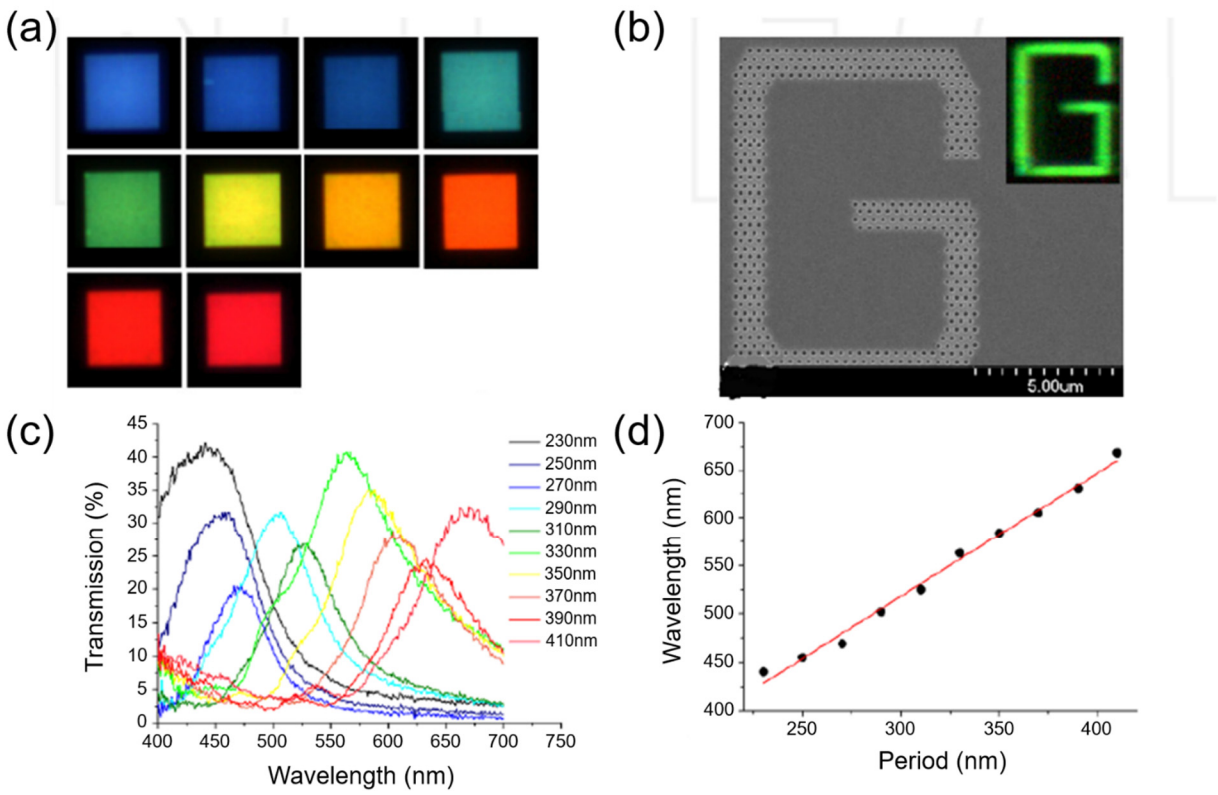

Figure 1.4 Plasmonic nanohole array transmitting different colors based on periodicity of the holes. (a) Images of various nanohole array in transmission mode under a white light illumination. (b) A SEM image of holes composing the letter 'G' with periodicity of 330 nm. The transmitted light image of the structure is shown in the inset. (c) Transmission spectra of the nanohole arrays shown in (a). (d) Dependence of transmission peak of the nanohole array on the period of the holes. Adapted from [41, 47, 48].

CHAPTER 2

FABRICATION AND CHARACTERIZATION OF PLASMONIC DEVICES

2.1 Fabrication of plasmonic sensors

Plasmonic structures can be referred as free-standing metal structures or metal is deposited over nanophotonics structures, have gain interests recently because of it can able to guide the light and manipulate it at nanoscale dimensions. Chemical Synthesis procedures have been used to attain metal nanoparticle with different shapes and sizes such as rods, boxes, cubes, spheres, rice, bowls, cages and pyramids.[49, 50] However, there is a limitation in order to achieve uniformity and periodicity in the shape and sizes between different structures of nanoparticles in a pattern while using solution-based methods.[51] This issue can be resolved by using direct writing methods and higher resolution nanostructures (i.e. 10nanometers) for plasmonic sensing can be achieved using equipment like focused ion beam (FIB) and electron beam lithography (EBL).[52] As this method is a serial process which cause it very slow and expensive. Moreover, there can be electron or ionic scattering during the ablation process of the FIB and resist polymer material can be swelled during the development process which will further introduce constrained to achieve consistency in nanostructures. The resolution can also be limited by additional processing steps in the fabrication which includes patterning and deposition of the metal layer because the deposited films, either using sputtering methods for better step coverage or by using electron beam evaporation which create side wall nanoparticles, are intrinsically polycrystalline in nature and the rough-grain boundaries in the surface of the metals initiate unwanted ohmic losses and scattering in the plasmonic devices.

Recently, Teri Odom's lab at Northwestern University has introduced a new methadology which is reffered as PEEL (combining PSP (phase-shifting photolithography), etching, electron-beam deposition, and lift-off) to make well-defined patterend structures in a photoresist into free-standing materials (Figure 2.1).[53] The key attributes of using EBL and FIB to generate plasmonic nanostructures are high resolution, controllability in design and shape and also fewer defects (Figure 2.2).[54, 55] However, tools like EBL, FIB or deep-UV projection lithography are very expensive and are difficult to scale for large-scale fabrication of plasmonic structures because of the low throughput due to the serial process.

The ablation mechanism in FIB is a complex combination of the photochemical and photo-thermal processes. The etch rate selection of different materials for ablation is also a challenge as the etched fragments can re-deposited on the projection lens which can damage the optics. To overcome these problems various soft lithography techniques such as replica molding, microtransfer printing, and nanoimprint lithography (NIL) [56-59] are used in which the master mold is physically pressed into a ultraviolet (UV) cure polymer material, which is the target substrate, to transfer the features from the master mold followed by curing of the polymer material under the UV light. Furthermore, a new method called template stripping is also being used to achieve ultrasmooth nanoplasmonic surfaces as shown in Figure 2.3.[60] In this method, first the silicon wafer is patterned followed by the metal deposition which is attached with epoxy or other adhesive backing layer. The noble metals have good wettability but very bad adhesion with the clean substrate such as silicon wafer. Therefore, the deposited metal can easily be released from the template (silicon wafer) having similar feature on the metal surface with the help of the backing layer.

2.2 Nanoscale Lycurgus cup arrays

A plasmonic nanostructure know as nanoscale Lycurgus cup array (nanoLCA) has developed by Logan Liu's group using the replica molding process. This process is very cost effective as we need to design and fabricate the master mold and replicate as many devices as possible from that single mold. Therefore the fabrication is started with the master mold, which consist of periodic nanocone pattern which is done using laser interference lithography technique followed by deep-RIE (reactive ion etching). In order to study the effect of nanocones size and shape, a range of different heights is fabricated (i.e. h = 250, 500 and 1000 nm).[61, 62] Figure 2.4 shows the SEM images with different sizes of nanocones structures in the master mold on the glass substrate with 350nm center-to-center distance between two adjacent nanocones. Figure 2.5 shows the schematic diagrams for the fabrication process of nanoLCA using replica molding method. The master mold is first cleaned and silanized followed by evenly spread of UV-curable polymer (UVcP) (NOA-61, Sigma Aldrich) on the top of it (Fig. 2.5 (a)). Then, PET sheet is carefully put on top of the polymer, to avoid the bubble formation and to act as a substrate, and exposed to UV-light (105 mW cm^{-2}) (Fig. 2.5 (b)). The PET substrate with nanohole arrays was peeled off carefully from the master mold (Fig. 2.5 (c)) and then in order to make the structure surface plasmon active, 90 nm of metal layer of gold is deposited (Fig. 2.5 (d)). Figure 2.6 shows the SEM images of the nanoLCA plasmonic device fabricated using replica a molding process indicates that the features from the master mold can be transferred to the UVcP with high fidelity. This process, using replica molding, is used to make a low-cost, wafer-scale plasmonic device with a simple methodology and high resolution and also opens up opportunity for biosensing applications. However, due to imperfect replica molding, defects can be introduced on the plasmonic device which can broaden the resonance.

2.3 Sensitivity of plasmonic sensors

As shown in Table 2.1, the sensitivity of plasmonic sensors are limited to about 1000 nm/RIU in the visible range. High sensitivity of more than 1500 nm/RIU are shown in the IR and nearIR region using plasmonic array sensor.[63] Recently, Gartia et al. reported a surface plasmon-based sensors using cup shaped nanohole array (also known as nanoLCA)).[64] NanoLCA enables detection of reactions that induce a small change of the refractive index such as DNA hybridization even by naked eye. Figure 2.7 presents a comparison of geometrical differences between common EOT structures and the nanoLCA structure for enhancing the plasmonics characteristics.[64] First, due to the tapered design of the nanohole structure, photons from the incident light are focused on the bottom of the nanohole which induce the radiative coupling of surface plasmons cause the enhancement in the localized electric field and EOT. Secondly the localized resonance supported by 3D nanoLCA will enable broadband tuning of optical transmission through controlling the shape, size, and period of holes as well as the shape, size, and period of metallic particles decorated at the side walls. Moreover, the LSPs mediated transmissions in nanoLCA are expected to be of higher magnitude than the SPPs mediated transmission in typical 2D hole arrays. Figure 2.8 shows how the nanocup array sensor changes color when different liquids are dropped on its surface. Figure 2.8 (a) shows the white light transmitted by a hole with the shape of wavefunction "ψ". Figure 2.8 (b) shows the same hole with the nanocup array sensor on top of it. The image is taken in transmission mode, when air (n = 1) is present, the surface of nanoLCA sensor appears green. Similarly, Figure 2.8 (c) shows an array of holes and Figure 2.8 (d) shows the corresponding transmission image of nanoLCA on top of it. The scale bars for both the images are 100 μm. The dotted area in Figure 2.8 (d) shows the color orange when sodium chloride solution partially covers the surface of the nanoLCA. Figure 2.8 (e) shows the vibrant color produced by the nanoLCA

when the different solutions (with refractive indices $n > 1$) are dropped on the surface. The transmission spectrum will redshift and it will redshift more with larger n values. In Figure 2.8 (e), oil with larger n values appear redder compared to that of the sodium chloride (NaCl) solution.

Due to longer decay length (200-300 nm for SPR [65], 5-10 nm for LSPR [66]) of the evanescent surface plasmon wave, SPR-based sensors have a higher sensitivity to bulk refractive index changes, whereas LSPR sensors are more sensitive to surface refractive index changes such as a molecular adsorption processes.[67] However, due to longer decay length of the evanescent wave, the results obtained from the SPR sensor is a convolution of both surface and solution-based refractive index changes. In general, LSPR-based sensors are at least an order of magnitude less sensitive than SPR sensors.[68] In addition, the smaller propagation lengths (or lifetimes) in typical LSPR sensors lead to broad resonance line width. This limits the Figure of merit (FOM) achievable by LSPR sensors. However, in the nanoLCA sensor design the mirror-like structures such as Bragg reflectors was used to produce Fano resonances from the interference of evanescent (dark) and propagating (bright) modes (Fig. 2.8).[64] This allowed the sensor to have higher FOM in spite of using LSPR. True colorimetric sensing on subwavelength hole structures (also known as EOT devices) is challenging because of the appearance of multiple transmission peaks due to multiple interferences and diffraction of light generally known as the surface plasmon polariton-Bloch wave (SPP-BW) and Wood's anomaly. The so-called quasi 3D plasmonic crystals [69] utilize the change in the transmission intensities (none or minimal shift in the resonance peak wavelength) for analyte detection and quantification. However, the resonance of such devices has only been demonstrated in near infrared and far infrared wavelengths [69] making it difficult to use conventional bright field microscopes and color photography for colorimetric sensing. On the other hand, the reported nanoLCA sensor demonstrates an improvement in the biosensing platform by combining LSPR

and SPR. In this design LSPR scattering modes of the metal nanoparticles on the nanocup side walls are selectively transmitted by the nanohole array to achieve higher sensitivity.

The sensitivity (S) of the SPR sensor is defined as the ratio between the resonance wavelength shift to the variation of the refractive index of the surrounding medium,

$$S = \frac{\Delta\lambda(nm)}{\Delta n(RIU)} \quad (2.1)$$

and the FOM of the sensor is defined as the ratio between sensitivity and the line width of the resonance ($\delta\lambda$):

$$FOM = \frac{S(nm \cdot RIU^{-1})}{\delta\lambda(nm)} \quad (2.2)$$

Research studies are primarily pursued to increase the sensitivity (increasing the wavelength shift) and improve FOM (decreasing the linewidth) of the SPR sensor in addition to develop various biosensing applications. Table 2.1 presents a comparison of sensitivity of different plasmonic sensors. As shown in the table, one of the ways to increase sensitivity is by increasing the aspect ratio as the aspect ratio is directly proportional to the dipolar polarizability. For example, by increasing the aspect ratio from sphere to disk and to nanorods, the sensitivity generally improves. Similarly, the sensitivity can be improved by introducing multipolar resonances, for example using nanocrescents [70, 71], instead of dipolar resonances (for example, nanospheres). Peter Nordlander recognized that plasmon hybridization can be utilized, such as using nanorings, to increase the sensitivity of the SPR sensor.[72] Fano resonance, where weak coupling and interference occurs between dark and bright plasmon modes, has emerged as another method to improve the sensitivity. In 1998, Ebbesen showed that periodic nanohole arrays in thick metal film can be utilized to observe extraordinary optical transmission (EOT).[73] Since then, the EOT

structure has been extensively used for surface-based biosensing as oppose to colloidal-based sensing. In order to improve the sensitivity of EOT structures, LSPR, colloidal particles and mirror like structures have been incorporated.[64]

Even though the naked eye sensing is implemented with plasmon-based colorimetry, it is for qualitative detection only. To make a biosensor which can do point-of-care detection and accurately perform quantitative analysis, especially for lab-on-chip applications, peripheral facilities and packaging is indispensable. The lab-on-a-chip-based sensor has the advantages of miniaturization, portability, automation, low cost and negligible consumption of reagents. In recent decades, the development of microfluidic-based technology has greatly advanced the progress of micro total analysis systems.[32] The simultaneous rise of plasmonics and microfluidics has enabled the researchers in the fields enthusiastically explore for plasmonic sub-wavelength optics and rapid-prototyping of lab-on-a-chip devices, forging a new field named plasmo-fluidics.[74] Among the plasmo-fluidic devices, ordered arrays of nanoholes in metal films facilitate resonance-induced field enhancement with no need of additional optical instrumentation.[75] Using nanohole arrays as sensing elements has the advantages of high reproducibility, small footprint, multiplexing capabilities and the possibility for collinear optical integration.[76] These advantages make nanoholes particularly suitable for planar integration into on-chip microfluidic environments.[74]

2.4 Microfluidic on nanoLCA sensors

NanoLCA have been integrated with microfluidics to realize simple, portable, label-free optical sensors that have a small sample volume requirement, improved mass transport, and simplified optical illumination and detection systems. Microfluidics have been integrated with other types of label-free optical sensors such as surface plasmon resonance,[77] photonic

crystal,[78] and ring resonator[79]. Affinity capture assays performed on a photonic-crystal sensor demonstrated that the microfluidic format has the fastest analyte detection time, the lowest limit of analyte detection, and the largest binding of analyte compared to the same assays performed in a microplate format and a spot format.[80] Moreover, microfluidic format has the advantages of enabling kinetic measurements (e.g. association and disassociation of analyte) and low analyte consumption. In particular to nanoLCA sensors, microfluidics also allows for flow-through design, as opposed to flow-over, when the nanohole are open through holes; in this case, the nanoLCA acts not only as a sensing element but also as an analyte concentrator by confining the flow to the sensing area.[81] The integration of microfluidics to plasmonic-based sensors and more specifically, nanohole-array-based sensors has been extensively reviewed elsewhere.[32, 74]

(Poly)dimethylsiloxane (PDMS) is a common elastomer used to fabricate microfluidic devices due to its many advantages, including solvent compatibility, optical transparency, and feature replication (Figure 2.9 (a-c)).[82, 83] In fabrication, the precursor agents (base agent and curing agent) of PDMS are mixed and degassed, and the PDMS solution is poured over a master with microfluidic design, which can be fabricated by photolithography or stereolithography. The PDMS solution is then cured thermally, and after curing, the microfluidic design is replicated on the PDMS substrate. The PDMS can be used to replicate micro-scale features (e.g. channels and chambers) down to hundreds of nanometers in a lateral resolution reliably and the same master can be used to fabricate more PDMS devices repeatedly.[84] Most commonly, the PDMS devices are integrated with a SiO_2 surface, in which both surfaces are treated with O_2 plasma to form hydroxyl groups and to form chemical adhesion between the two surfaces.[85] However, nanoLCA sensors are typically coated with coinage metals, e.g. gold (Au) or silver (Ag), and these materials are not compatible with O_2 plasma treatment to integrate with the PDMS microfluidic device.

Other bonding techniques are available to integrate the PDMS microfluidic device with the nanoLCA sensors (Figure 2.9 (d-f)).[86] The desirable properties of the bonding method and materials are solvent compatibility, topographical compatibility, mechanical robustness, and optical transparency. A thin layer of silica has been deposited on top of the coinage metal for O_2-plasma-treatment adhesion and biological interfacing.[87] Optical adhesives, curable by photo- or thermal activation, can act as an adhesive layer between the PDMS device and the surface of the nanoLCA sensor.[86] For non-permanent adhesion, the PDMS device has been mechanically compressed *via* sandwiching between two rigid plates and clamping.[88] Likewise, the nanoLCA can be directly integrated into a flow cell, which can be fabricated with other materials beside PDMS.[89] Due to the flexibility in the channel designs and the ease of fabrication methods, the microfluidic device can be tailored to the applications ranging from simple fluid transport to fluid mixing using serpentine channels (Figure 2.10 and 2.11).

2.5 Optical illumination and detection of nanoLCA

An optical illumination source is required to observe the extraordinary transmission and to detect the changes in the intensity of the transmitted or reflect spectrum of the light as it transmits or reflects from the nanoLCA. The optical illumination source is typically a broadband source (e.g. tungsten-halogen lamp, xenon arc lamp) with light production in the visible wavelength range (λ ~ 450–750 nm) and in the near-infrared range (λ ~ 750–1000 nm). A broad range of wavelength is required to detect the change in the wavelength at which there is maximum intensity. Alternatively, a monochromatic illumination source (e.g. laser, light emitting diode) can be utilized to illuminate the nanoLCA but only the variations in the intensity of transmitted/reflected light can be detected. With monochromatic illumination sources, the choice of wavelength is limited due to

the discretized nature of the light that can be produced (e.g. laser lines are limited wavelengths such as 532 nm and 633 nm). An important property for an illumination source for nanoLCA is high spectral irradiance (given in units of W/m^2 nm) in the relevant range of wavelengths or high irradiance (W/m^2) for monochromatic sources. Even with extraordinary transmission, nanoLCA sensors typically transmit less than ten percent of the illuminated light; in addition, the area of the sensor may be limited to hundreds of micrometer squared, which requires high magnification objectives with a small field of view that reduces the amount of the transmitted light to be collected.

Accordingly, several optical detection systems have been used in conjunction with the aforementioned illumination sources. For spectral measurement, a grating is required in the detection system to disperse the broadband transmitted light and a charge-coupled detector is used to quantify the dispersed light according to its wavelength, for example in a spectrophotometer (Figure 2.12 (a)). Photomultiplier tubes may be used for quantifying the transmitted light from monochromatic illumination sources. Additional optical components such as high pass, low pass, and band pass filters, dichromatic mirrors may be employed to further distinguish the spectral or intensity changes in the transmitted light through the nanoLCA sensor. For imaging, charge-coupled detectors overlaid with a color filter array (e.g. Bayer filter that has 50% green, 25% blue, and 25% red components) can be used to visualize the nanoLCA sensor with some spectral distinction (Figure 2.12 (b)). In our study, both form of instruments schematically shown in Figure 2.12 was utilized.

2.6 Analysis of detection using nanoLCA sensors

In the case of broadband illumination, the spectrum of transmitted light through a nanoLCA is quantified using a spectrophotometer. In the measured spectrum, there may be single or multiple

peak wavelengths, which is the wavelength at which the transmitted intensity is global or local maximum (Figure 2.13). The peak wavelength can be identified by simply searching the intensity maxima and the peak wavelength shift ($\Delta\lambda$) can be quantified by determining the change in wavelength when the nanoLCA is exposed to different refractive indices (Figure 2.13(a)). This peak wavelength shift can be correlated with the change in the refractive index (Δn) on or adjacent to the surface of nanoLCA sensor. The peak wavelength shift sensitivity (S) of the nanoLCA sensor can be calculated as $S=\Delta\lambda/\Delta n$. Other metrics can be used to quantify the changes in the transmission spectrum (spectral or intensity). One method is to integrate the area under the transmitted spectrum under a range of wavelengths to obtain an integrated response sensitivity (R).[90] For a given spectrum, R can be calculated as $R(n) = \sum_{\lambda_1}^{\lambda_2} \left|\frac{I(n,\lambda)-I(n_0,\lambda)}{I(n_0,\lambda)}\right| \times 100\%$, where $I(n,\lambda)$ is the measured intensity at wavelength λ for a given refractive index n (n_0 is the reference refractive index), and λ_1 and λ_2 is the wavelength range over which the spectrum is integrated (Figure 2.13(b)) . This method of sensitivity measurement can have a higher signal-to-noise ratio compared to the peak wavelength shift measurement.[90] For intensity variation measurement interrogated by a monochromatic light source, a single value is obtained for a single point measurement and a time trace can be obtained by recording the intensity over a course of time period (Figure 2.13(c)). For colorimetric imaging measurement, the red, green, and blue (RGB) channels from a color image can be obtained. Each channel represents a portion of the transmission spectrum, that is the intensity in the red channel is from the transmitted light in a longer wavelength range and the intensity in the blue channel is from the transmitted light in a shorter wavelength range. Similar to intensity variation measurement, the change in the intensity from each channel can be correlated with the change in the transmission spectrum. Unlike intensity variation

measurement, RGB contains three values for a single point measurement and it may have higher sensitivity than that of intensity variation measurement.[91]

2.7 Figures and tables

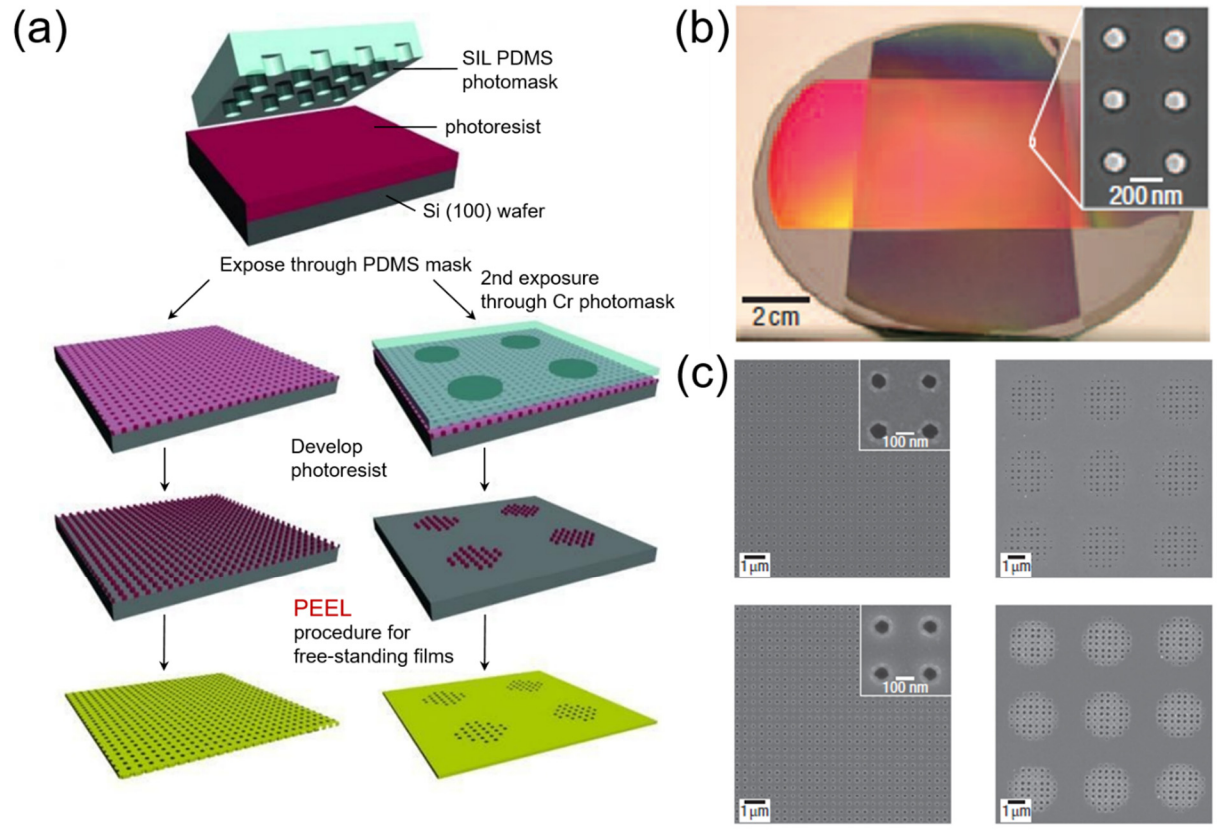

Figure 2.1 Soft interference lithography. (a) Schematic showing the PEEL (Photolithography, Etching, Electron-beam deposition and Lift-off of the film) process. (b) Optical image of master mold used in the PEEL process. The area of the mold is about 14 cm x 14 cm and it consist of array of Si post with diameter = 100 nm, height = 400 nm, and pitch = 400 nm. A SEM image of the post is shown in the inset. (c) SEM image of the replicated nanohole array from the master mold. Adapted from [92].

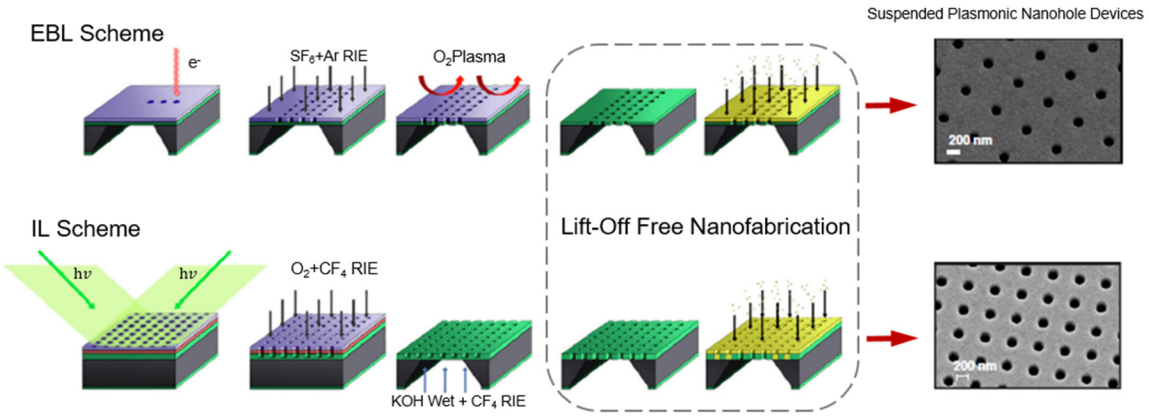

Figure 2.2 Lift-off free evaporation (LIFE) method of forming nanoholes. The method involves making holes on the underlying SiNx membrane instead of the PMMA resist. The back-etching of Si supporting substrate enables a suspended plasmonic nanohole structure. Both electron-beam lithography (EBL) and interference lithography (IL) was used to make the nanohole structures. SEM images on the right shows fabricated devices shows nanohole array with period of 600 nm, and diameter of 180 nm made using EBL process; Using IL process the periodicity was 580 nm and the diameter of the holes were 230 nm. Adapted from [93].

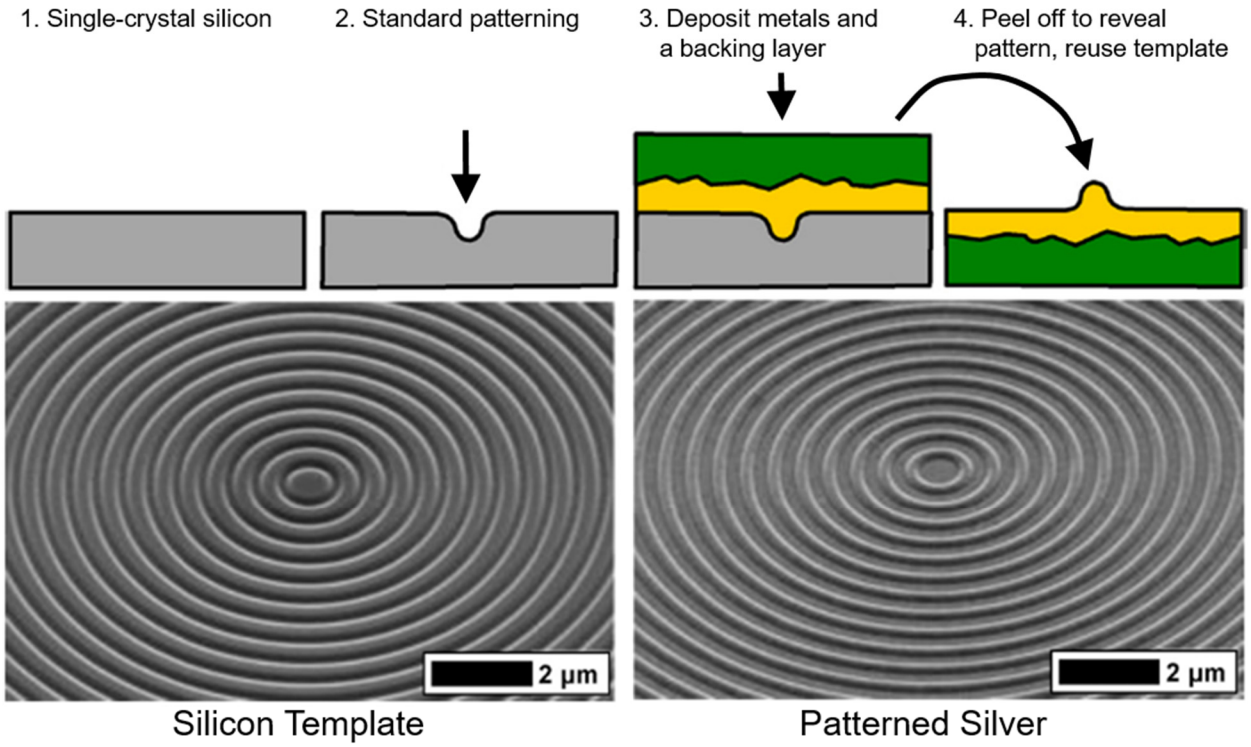

Figure 2.3 Schematic of template stripping methods to make plasmonic devices with smooth surfaces. This process takes advantage of the poor adhesion and good wettability of noble metals on silicon. SEMs of the silicon template and template stripped silver device is shown at the bottom. Adapted from [94].

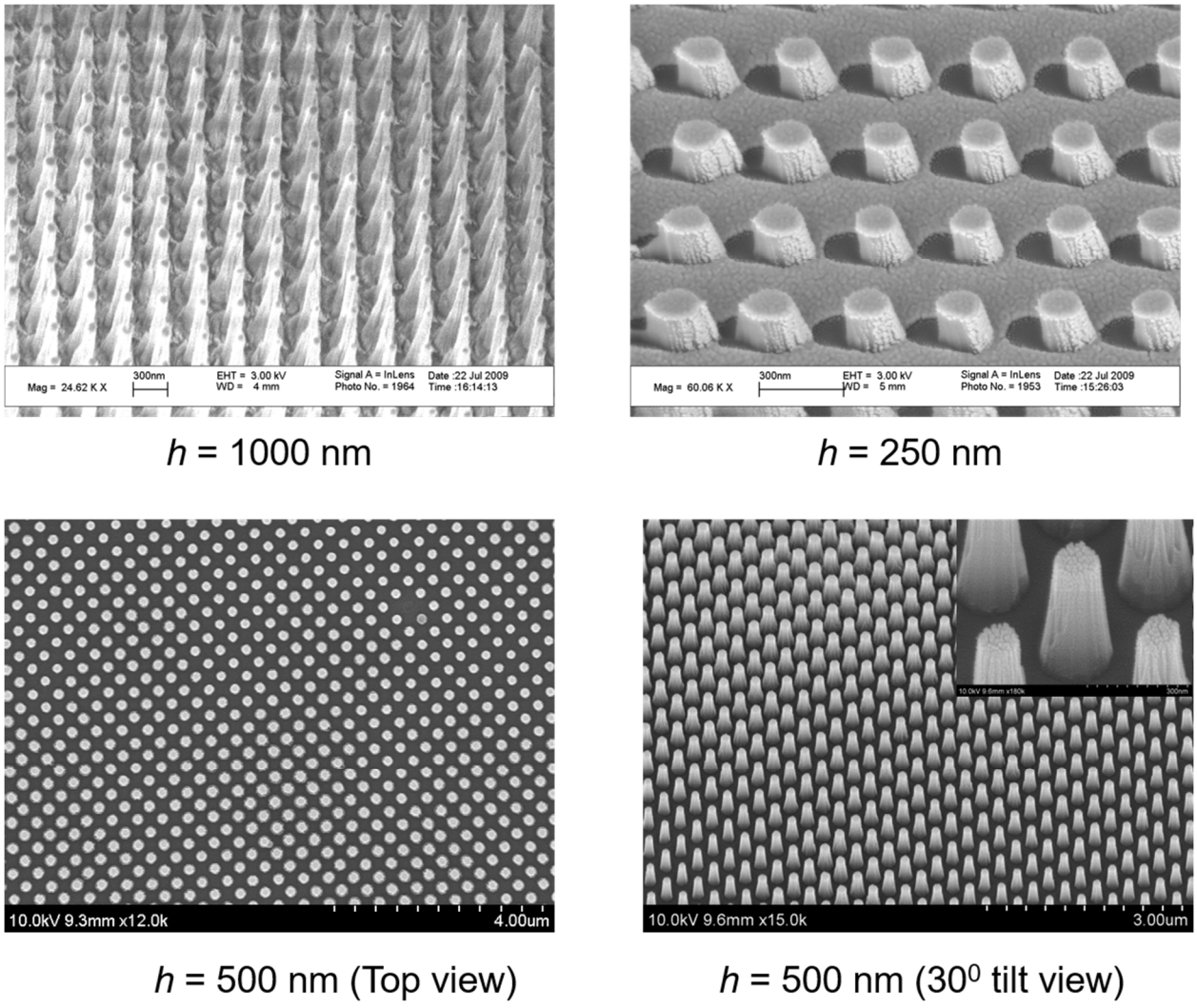

Figure 2.4 SEM images of the master mold used for the fabrication of nanoLCA device. The master mold is fabricated on a glass substrate using laser interference lithography technique [95, 96] with a range of different heights; h = 1000 nm (top left), h = 250 nm (top right), h = 500 nm top view (bottom left) and h = 500 nm 30^{o} tilted view (bottom right).[64]

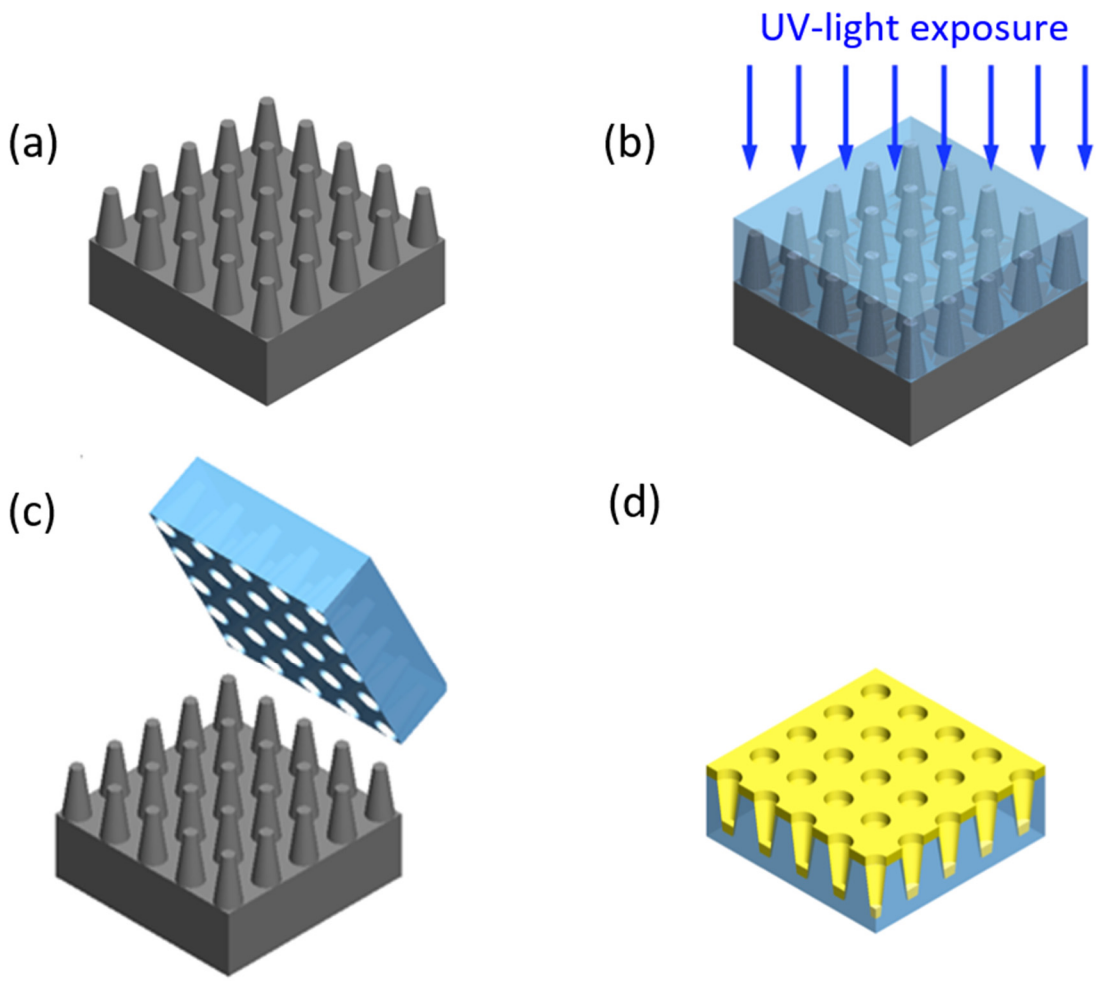

Figure 2.5 Schematic overview of the replica molding fabrication process. (a) The nanocone master mold made on glass substrate is first cleaned and silanized for 30 min followed by ethanol and deionized water rinse. (b) 2000 µL of UV-curable polymer (NOA-61) is evenly spread on the top of the nanocone master and a PET sheet is carefully, to avoid the bubble formation, put on top of the polymer to act as a substrate. The master with the polymer and PET sheet then exposed to UV-light (105 mW cm^{-2}) for 60 sec. (c) The PET substrate with nanohole arrays is peeled off carefully from the master mold. (d) Then and then in order to make the structure surface plasmon active, 90 nm of metal layer of gold is deposited.[64]

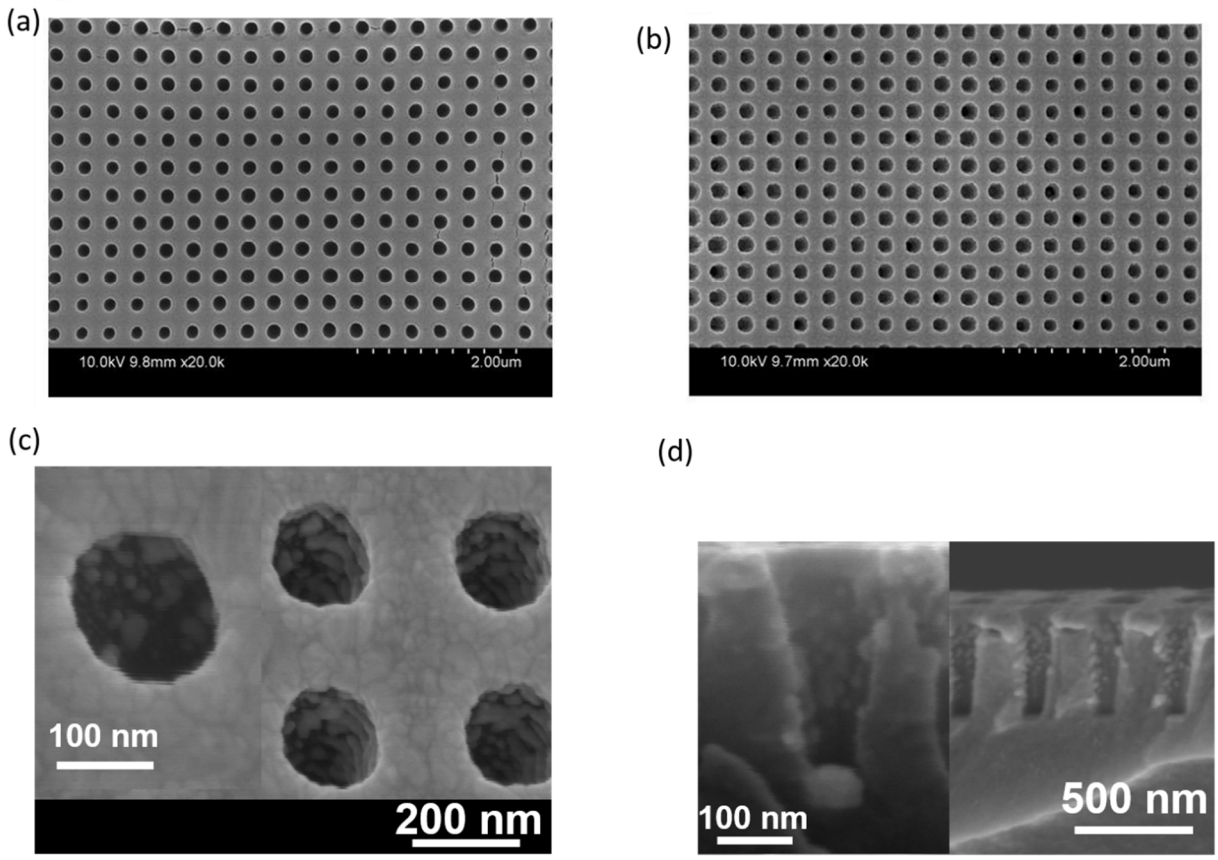

Figure 2.6 SEM image of the nanoLCA device using replica molding method. (a) SEM (top view) image of nanohole array in the polymer without metal deposition. (b) SEM (top view) image of nanohole array after gold (Au) deposition of 90 nm. Top (c) and cross-sectional (d) view SEM images of nanoLCA device exhibiting the metal (Au) nanoparticles on the sidewalls of the nanocup structures.[64]

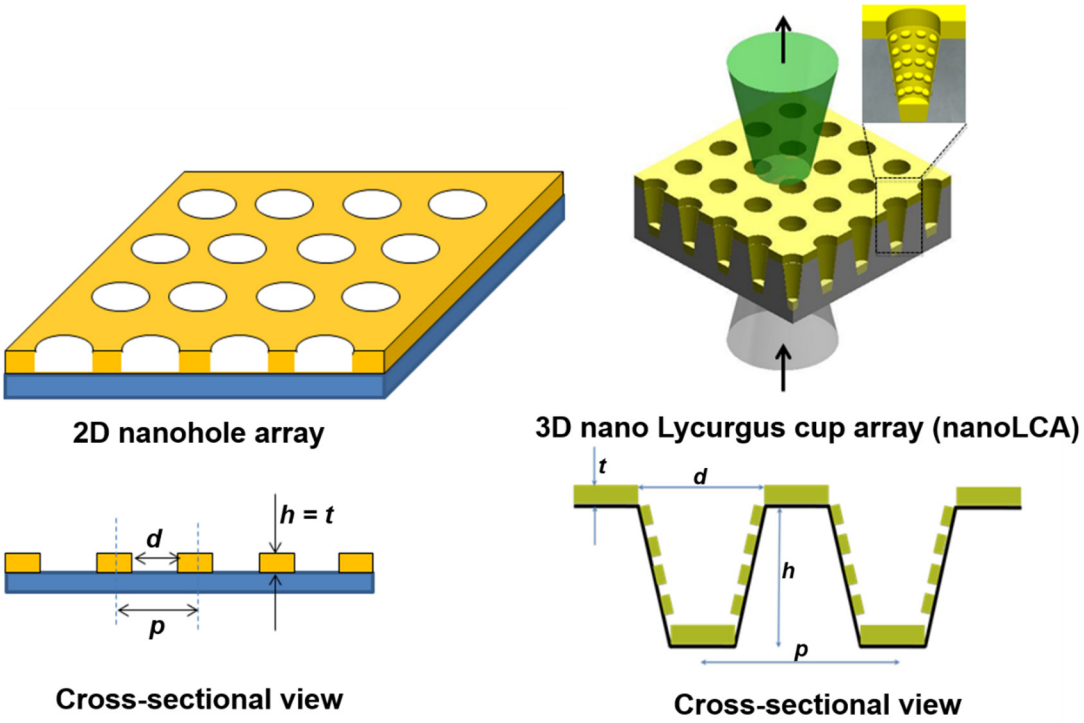

Figure 2.7 Geometrical comparison of conventional 2D nanohole plasmonic substrate vs. 3D nano Lycurgus cup array (nanoLCA)-based plasmonic substrate.[64]

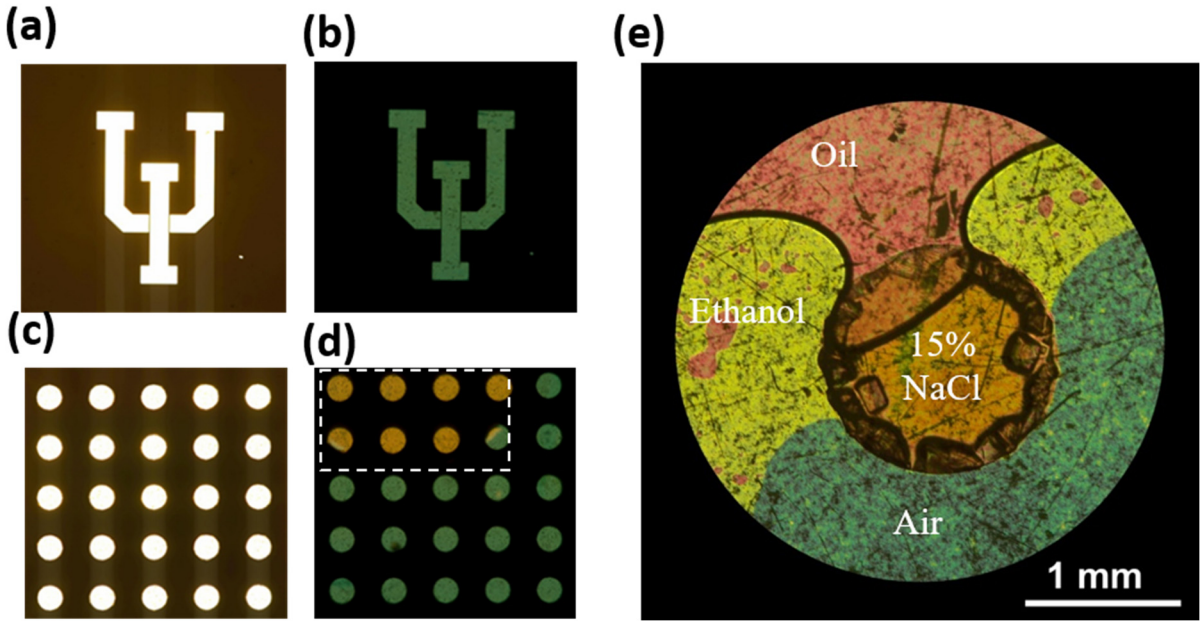

Figure 2.8 Colorimetric plasmonic sensing with nanocup array device. Bright field image (a, c) without, and (b, d) with the sensor. The green color is with air (n = 1) and the orange color (inside the dotted area) is due to NaCl solution on top of the sensor. (e) Mixture of ethanol, oil and NaCl shows distinctive colors on the sensor.

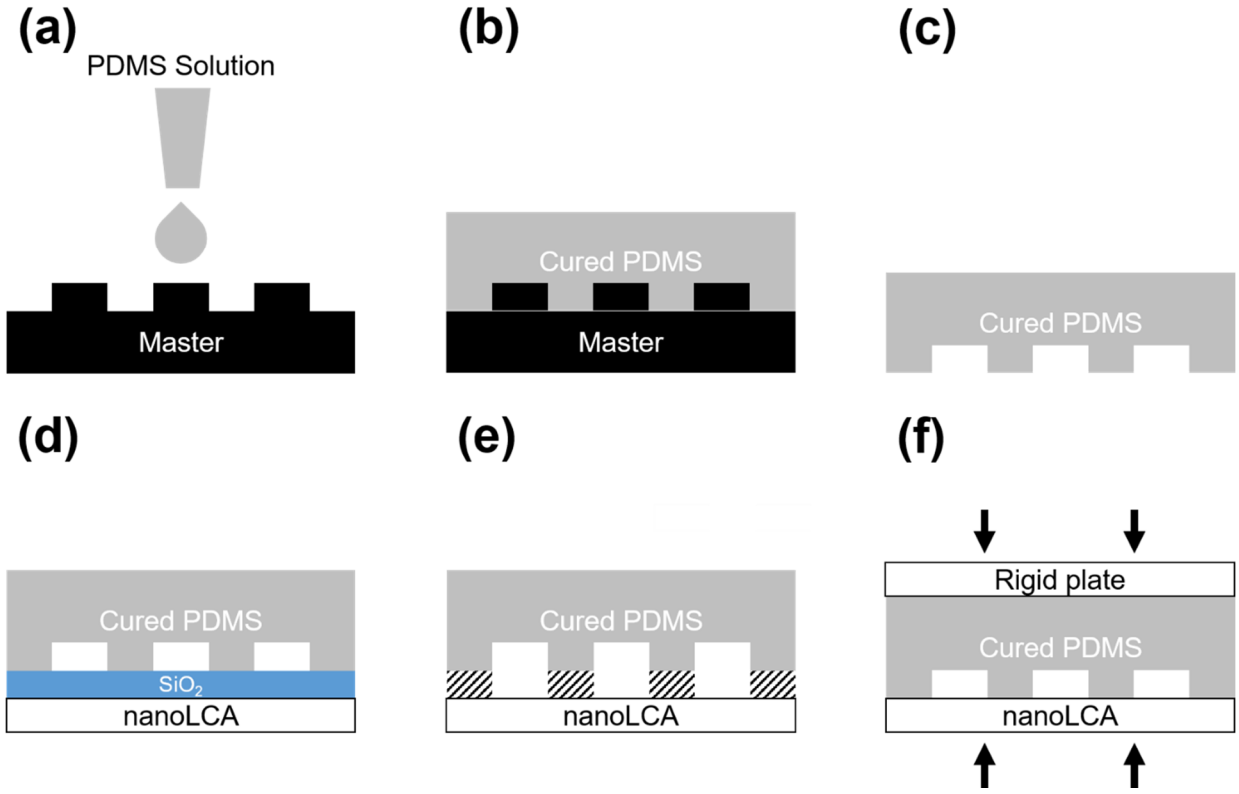

Figure 2.9 Schematic overview of fabrication and integration of PDMS-based microfluidic device with nanoLCA sensor. (a) (Poly)dimethylsiloxane (PDMS) solution, consisted of the base agent and the curing agent, is poured over a master mold. (b-c) The solution is cured thermally and when cured, the PDMS device is excised and removed from the master mold. The PDMS-based microfluidic device can be integrated with the nanoLCA sensor *via* (d) deposition of thin layer of SiO_2, (e) stamp of thin layer of adhesive (indicated by diagonal lines), (f) compression between rigid plates. Note the deposited layers are not drawn to scale.

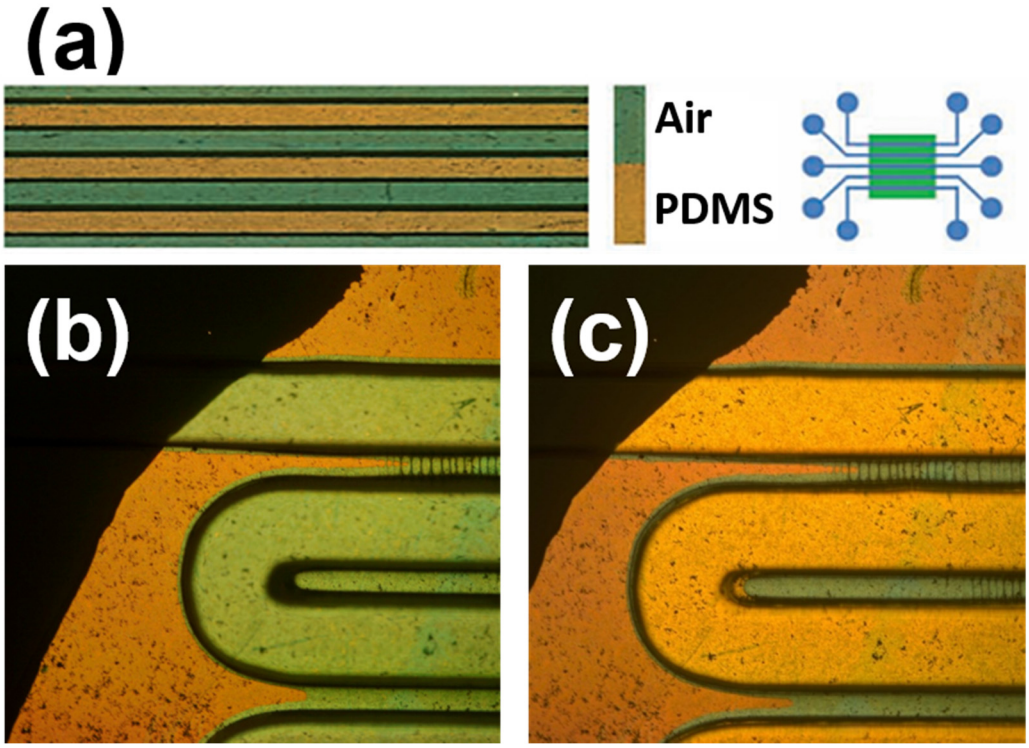

Figure 2.10 Overview of different microfluidic designs integrated on nanohole array sensor. (a) Parallel microfluidic channels with a width of 500 µm. (b) Serpentine microfluidic channels on a nanohole sensor array empty and (c) the same channel filled with water. (Channel width: 500 µm). Modified from [97].

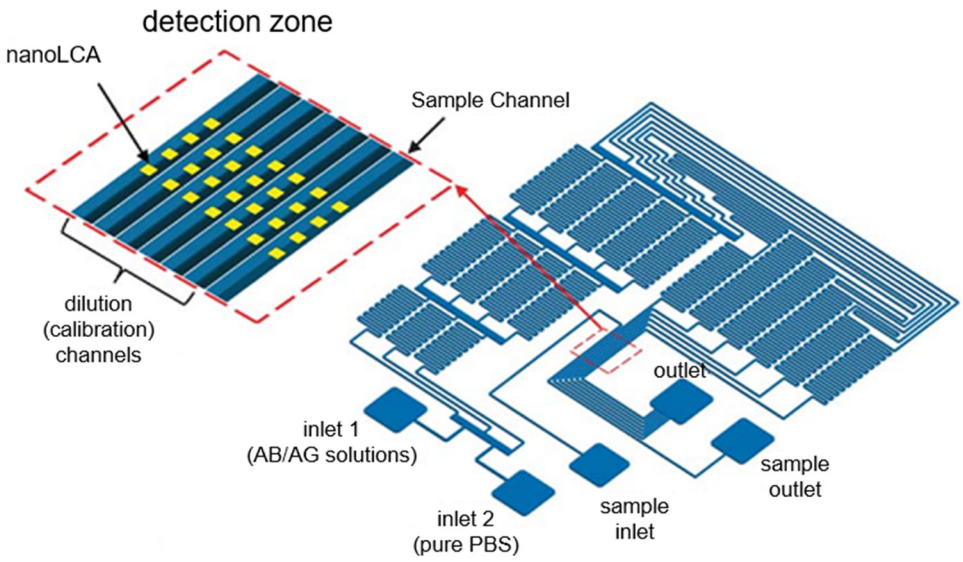

Figure 2.11 Overview of different microfluidic designs integrated on nanohole array sensor. (a) Parallel microfluidic channels with a width of 500 µm. Microfluidic concentration gradient generator using serpentine channels integrated with nanoLCA sensors. Modified from [97].

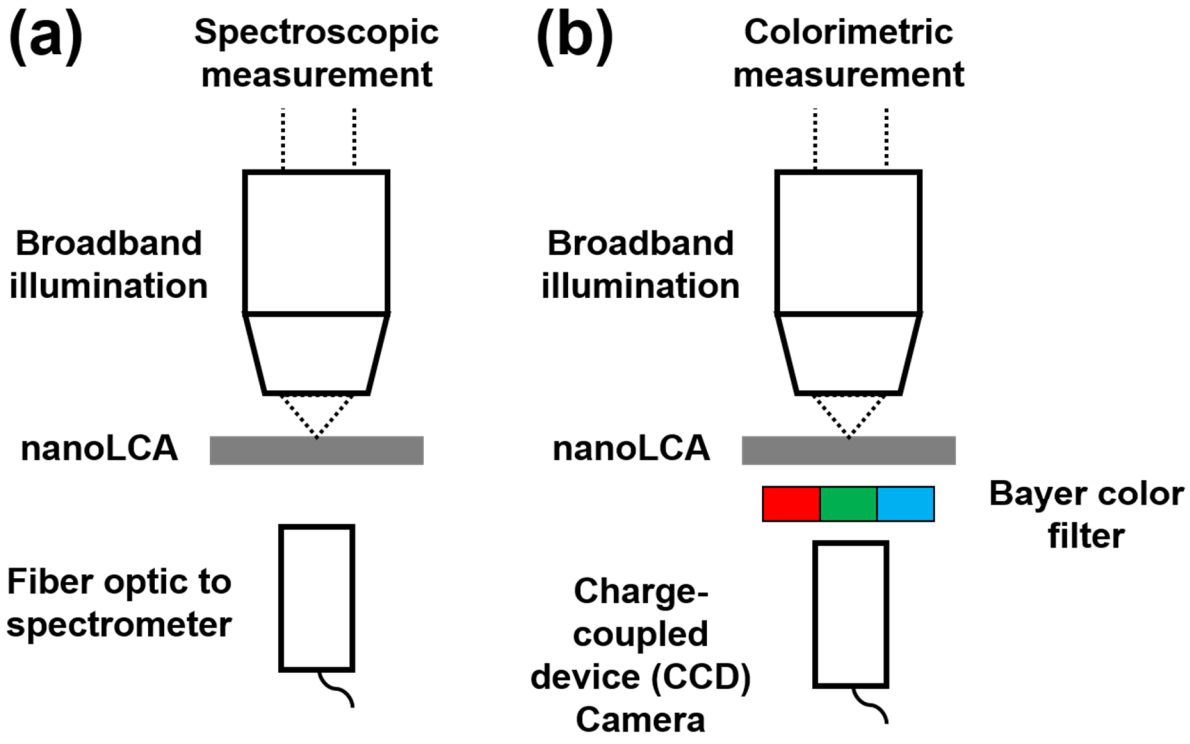

Figure 2.12 Typical optical setup for the measurement of transmission through nanoLCA sensor. (a) In spectroscopic measurement, in which the spectrum of the transmitted light is acquired, a broadband illumination is incident on the nanoLCA sensor and the transmitted light is collected using a fiber optic coupled to a spectrometer. (b) In colorimetric measurements, in which the intensity of the transmitted light through a color filter (e.g. Bayer color filter) is acquired, a broadband illumination is incident on the nanoLCA sensor and the transmitted light is passed through a color filter and imaged using a charge-coupled device (CCD) camera.

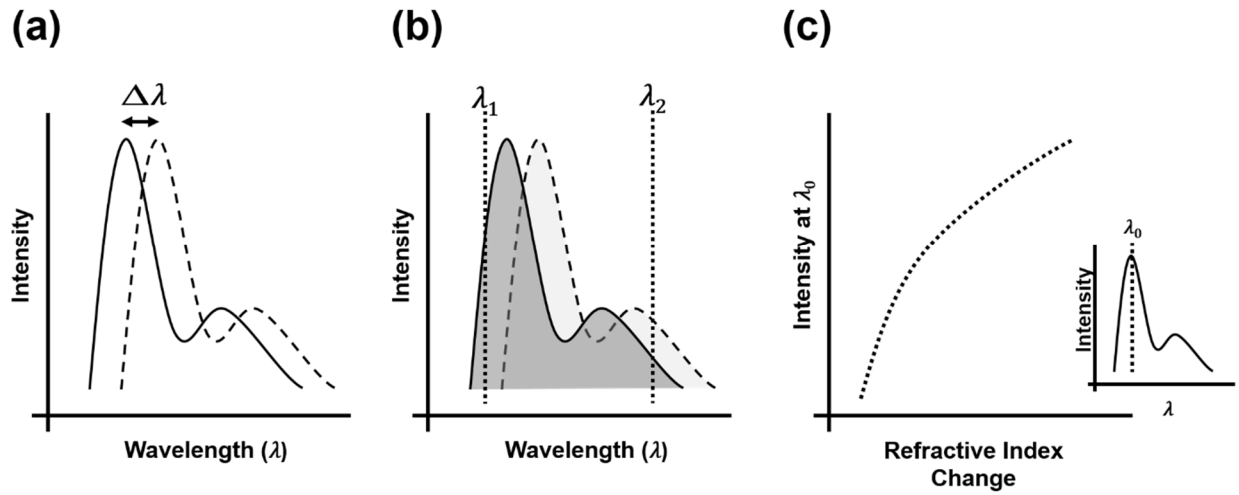

Figure 2.13 Schematic representative of the optical response of nanoLCA sensor to refractive index change. (a) The change in the wavelength of maximum transmission intensity, also known as peak wavelength shift, can be quantified when comparing the transmission spectrum of nanoLCA sensor exposed water (refractive index=1.33) (solid) and water with glucose added (refractive index=1.34) (dashed). (b) Integrated sensor response can be obtained from integrating the area under the transmission spectrum over a defined range of wavelengths (e.g. λ_1 to λ_2). (c) Intensity variations at a single wavelength from the transmission spectrum (inset) can also be monitored in response to changes in the refractive index on the nanoLCA sensor.

Table 2.1. Sensitivity compariosn between different plasmonic-based sensors. *d*: diameter; *h*: height; *p*: period; *t*: thickness; *W*: width; *L*: length; *a*: length of the side of cube; AR: aspect ratio; C-C: center-to-center; EOT: extra-ordinary optical transmission; LSPR: localized surface Plasmon resonance.

Nanostructure	Wavelength (nm)	Structural Dimensions (nm)	Characteristics	Sensitivity (nm/RIU)	RI range	Ref.
Gold colloidal nanoparticles	450–600	*d*: 30	Shape-dependent LSPR	70.9	1.32–1.5	[98]
Arrays of gold nanodisk	500–1,000	*p*: 162, 340	Anisotropic property of gold nanodisk	167-327	1.32–1.42	[99]
Gold nano rods	800–1,000	AR- 3.5:1 *d*: 80	Size-dependent LSPR	650	1.34–1.7	[100]
Gold nanorings	900–1,500	*d*: 150 t_{Wall}: 20	Shape dependence on dielectric substrate	880	1.33–1.42	[101]
Nanocross and nanobar	1200–1,900	*L*: 380 *W*: 76 θ: 60°	Subradiant Fano resonances	710-1,000	1.333–1.38	[102]
Nanohole	450-950	*d*:200 *p*: 500 *t*:200 (Au)	EOT	481	1.33-1.36	[103]
Double-hole array	500-680	*d*:200 *C-C* spacing:190 *p*: 500-600 *t*: 100	EOT-LSPR	600	1-1.4	[104]
Silica sphere stripped nanowell	600-1000	*d*: 202-294 *h*:297-340 *p*: 280-370 *t*:60 (Au)	LSPR	1200-1600	1-1.6	[105]
Nano-Lycurgus cup array	300-1100	*d*: 170 *h*: 250-1000 *p*: 350±30 *t*: 60-120 (Ag)	Mie scattering-LSPR-EOT	46000	1-1.56	[64]

CHAPTER 3

INFLUENCE OF ADHESION LAYER ON THE OPTICAL PROPERTIES AND COLORIMETRIC IMAGING OF LAYER-BY-LAYER MOLECULAR DEPOSITION ON NANOPLASMONIC LYCURGUS CUP ARRAY

In this chapter, first, we will discuss the influence of the superstrate and substrate on the optical properties of the nanoLCA device. Then, a quantitative label-free colorimetric imaging of biochemical molecular thin film deposition at single molecule layer (2 nm thickness) resolution will be demonstrated on a nanoLCA sensor and the penetration depth of the nanoplasmonic sensor was accordingly determined. Colorimetric nanoplasmonic imaging technique provides significant advantages in direct visualization and quick identification of surface deposited molecules. We implement layer by layer deposition of alternating polyelectrolyte layers with controlled thickness on the nanoLCA device to show surface color changes and determine the decay length of the device derived from the sensor spectral response to the molecular layer thickness. The calculated decay length of the nanoLCA device is 193 nanometers which corresponds well with the decay length of other known surface plasmon sensors. In addition micro contact molecular printing and transferring on the nanoLCA surface is used to selectively deposit poly-L-lysine and different alkanethiol molecules and to demonstrate direct colorful visualization of surface patterned unlabeled molecules.

3.1 Introduction

Recently, a plasmonic nanostructure know as nanoscale Lycurgus cup array (nanoLCA), developed by Logan Liu's group using the replica molding process, has been demonstrated highly

sensitive refractive index sensing. [51, 94] This nanoLCA device exhibit extraordinary optical transmission phenomenon (EOT), however, unlike EOT substrate, which transmit multiple resonance wavelengths, this device transmit single prominent resonance peak wavelength in the refractive index range from 1 to 1.5 RIU. This optical property is very good for colorimetric sensing as we can correlate color with that specific peak.[106-110] While the surrounding refractive index is changed, the resonance wavelength is red-shifted in the visible wavelength range, results in the change of transmitting color, which allows not only the estimation of the refractive index of an unknown fluids introduced on the surface of the device but also allow colorimetric sensing of the target molecules.[62]

Adhesion layers, such as titanium (Ti) and chromium (Cr), are most commonly used to provide adhesion to the deposited metal layer and the substrate, however, titanium is preferred in the optical based sensors due to its lower optical absorbance in the visible wavelength range.[111] In label-free bio-sensing application, adhesion layer has significant influence on the sensitivity and FOM.

Surface plasmon polaritons (SPPs), propagate along a metal-dielectric interface with an electric field that decays exponentially normal to the surface of the device. This decay refers as decay length or penetration depth, the typically in nanometer range, which define the sensing region of the device. There are many different method for the surface-based characterizations for SPR sensing but one simple and common method is to deposit well-defined controlled thickness of thin films with known optical properties (such as refractive index) and measure the optical response of the device with respect to the film deposited on superstrate. An analytical expression can be used to calculate the approximate decay characteristics of electric field of the plasmonic device with known thickness of the deposited films and their effective response from the device.

Mostly, under certain conditions, oppositely charged materials are used for layer by layer (LbL) deposition such as cationic and anionic, which are attracted and attached through electrostatic interaction. The thickness of the polymer film is controlled by the immersion (or exposure) time of the device in the polymer solution. Here, we demonstrated LBL deposition of polyelectrolyte layers on the surface of nanoLCA device and with the analysis of spectrum and colorimetric response of the nanoLCA device, we are able to estimate the decay length of the device. Furthermore, we have introduced micro contact printing to selectively deposit poly-L-lysine and different alkanethiol, which is used for surface functionalization to attach bio-molecule on the surface of nanoLCA device.

3.2 Materials and methods

3.2.1 NanoLCA device fabrication

As we have discussed earlier, the nanoLCA device is fabricated using the replica molding process which is very cost effective as we need to design and fabricate the master mold and replicate as many devices as possible from that single mold. Therefore the fabrication is started with the master mold, which consist of periodic nanocones pattern which is done using laser interference lithography technique followed by deep-RIE (reactive ion etching).[61, 62] The master mold is first cleaned and silanized followed by evenly spread of UV-curable polymer (UVcP) (NOA-61, Sigma Aldrich) on the top of it. Then, PET sheet is carefully put on top of the polymer, to avoid the bubble formation and to act as a substrate, and exposed to UV-light (105 mW cm^{-2}). The PET substrate with nanohole arrays was peeled off carefully from the master mold and then in order to make the structure surface plasmon active, 90 nm of metal layer of gold is deposited.

3.2.2 Deposition of titanium and gold on nanohole array

Temescal six pocket electron beam evaporation system is used to deposit thin layer of Titanium (Ti) and Gold (Au) at the rate of 0.3 Å/s and 0.5 Å/s respectively. In order to deposit smooth metals films of Ti and Au, the deposition is performed at slow rate. Initially, the thickness is estimated using the crystal monitor of the evaporation system, which is later verified using Gaertner ellipsometer.

3.2.3 Finite difference time-domain simulation of the nanohole array sensor

Commercial finite difference time-domain (FDTD) software from Lumerical Solutions, Inc. is used to perform simulation of the nanoLCA device. The illumination source (incident light) is an electromagnetic plane wave which is polarized in x-direction and propagating in z-direction with an incident angle normal to the nanoLCA device. 2.5 nanometers mesh is used in all three directions. The same geometrical information (as mentioned in the previous chapter) is applied to the FDTD model. To eliminate the interference from the boundary, perfectly matched layers (PMLs) boundary conditions are applied in the z-directions and periodic boundary conditions are applied in the x and y directions to simulate single and arrays of nanohole structure. Each of the material properties (RI and *k*) are taken from the *Handbook of Optical Constants of Solids*. The refractive index of the underlying substrate, UV-curable polymer, is set as 1.56 RIU. The hole diameter is 100-nanometer with periodicity of 350-nanometer and thickness of top Au layer is 100-nanometer with 1- micrometer thickness of the polymer. Different thicknesses of Ti layer are used in order to demonstrate the influence of the adhesion layer on the optical properties of plasmonic nanoLCA.

3.2.4 Layer-by-layer deposition

All of the chemicals and reagents for the polyelectrolyte layer-by-layer deposition are purchased from Sigma Aldrich (Milwaukee, WI). The nanoLCA device is incubated in 33mM of dithiodibutyric acid (DTBA) for 24 hours in order to form a self-assembled monolayer (SAM) with one end as a carboxyl group followed by thoroughly rinsing of the device with ethanol and then dried with nitrogen flow. For LBL deposition, the device is immersed in Poly(allylamine) (PAH) solution for 5 minutes followed by the immersion in Poly(sodium 4-styrenesulfonate) (PSS) for 1.5 mins. PAH and PSS solutions are prepared in Millipore water with concentrations of 3 mg mL^{-1} (pH 8.0) and 3 mg mL^{-1} (1 M $MnCl_2$, pH 2.0) respectively. The immersion step is repeated until the desired thickness of the film achieved.

3.2.5 Micro contact printing of poly-L-lysine and alkanethiols

Poly-L-lysine solution with concentration of 1 mg/mL (Sigma Aldrich, Milwaukee, WI) is achieved with dilution of Milli-Q water. Additionally, 6-mercapto-2-hexanol (MCH) ($SCH_2(CH_2)_4CH_2OH$) and decanethiol ($CH_3(CH_2)_8CH_2SH$) (Sigma Aldrich, Milwaukee, WI) are used as a linker molecule to form SAM in order to provide adhesion to polyelectrolyte layers. For contact printing the polymer layer on the nanoLCA device, Polydimethylsiloxane (PDMS) stamps are used, which are fabricated by soft lithography. These stamps consist of circular structures backing with flat PDMS sheet. For the contact printing, circular regions are immersed in the alkanethiols or poly-L-lysine solution for 30 seconds and access solution is removed with nitrogen flow. Then the stamp is placed in contact with the nanoLCA device for 5 seconds to print the polymer layer. For layer by layer deposition, unstamped areas are filled with DTBA solution via immersion as discussed earlier.

3.2.6 Spectral and colorimetric characterization

Multi-spectral imaging system is used to perform spectral measurement. This system is based on a similar setup as described in [112], which consist of a halogen lamp source that illuminate the device with the range of wavelengths (i.e. from 400 nanometers to 800 nanometers) with a monochromator to provide an increment of 1 nanometer in wavelength of the incident light. At each wavelength, transmitted and reflected light is accumulated by 5× objective lens and simultaneously an image is captured using charge-coupled device (CCD) based camera. A custom made LabVIEW program (National Instruments) is used to synchronize control of the monochromator and the camera. In LBL deposition, the transmission and reflection spectrum of the nanoLCA device are measured instantly after the rinse and dry step. The spectrum of the light source is used to normalized the measured spectra and it's intensity $I(\lambda)$, is calculated as

$$I(\lambda)_{normalized} = \frac{I(\lambda)_{sample}}{I(\lambda)_{lightsource}} X \frac{t_{lightsource}}{t_{sample}},$$

where $I(\lambda)_{lightsource}$ and $I(\lambda)_{sample}$ are the transmitted/reflected intensity of the light source and sample respectively at each wavelength, and $t_{lightsource}$ and t_{sample} are the exposure time for the measurement of the light source and the sample respectively. Bright-field upright microscope is used to perform colorimetric imaging using color CCD camera with 100W halogen lamp used for the transmission and reflection illumination.

3.2.7 Ellipsometry measurement

The thickness of the LBL deposited polyelectrolyte layers is measured using a single-wavelength (632.8 nm) at a fixed angle ellipsometer (Gaertner Scientific Corporation, Skokie, IL). The estimated effective refractive index of deposited film is used as 1.63. In order to minimize the surface roughness, ten layers of polyelectrolyte film are deposited on a flat gold film on a (100)

bare silicon wafer. To calculate the thickness variation on a single device, ellipsometry measurements are performed on five different locations on the sample with polymer layers.

3.3 Results and discussion

3.3.1 Influence of the adhesion layer on the optical properties of plasmonic nanoLCA device

As discussed earlier, adhesion layers, such as titanium (Ti) and chromium (Cr), are most commonly used to provide adhesion to the deposited metal layer and the substrate, however, titanium is preferred in the optical based sensors due to its lower optical absorbance in the visible wavelength range.[111] In label-free bio-sensing application, adhesion layer has significant influence on the sensitivity and FOM. Here, finite difference time domain (FDTD) simulation of nanoLCA device with and without the adhesion layer is performed and the findings with the experimental results are compared. Figure 3.1 shows the schematic illustration of the nanoLCA device model used for FDTD simulation.

In the simulation results, when there is no adhesion layer present (Ti=0), two prominent peaks, at 530nm and 650nm, in the transmission spectrum of the nanoLCA device are observed with air (n=1) as a surrounding media. However, when the superstrate (top of the sensor) is changed to higher refractive index (RI), (n=1.33, corresponds to water), three prominent peaks are observed at 520nm, 600nm and 675nm respectively as shown in Figure 3.2. The FDTD simulation for the electric field (E-field) distribution on the cross section of the device at 600nm and 675nm (corresponds to second and third peak of the transmission spectrum with water, n=1.33, as a surrounding media) is performed which indicates E-field confinement at the interface between Au and water and Au and UVcP respectively as shown in Figure 3.2. In the experimental results, the

transmission spectrum in air consists of one prominent peak wavelength at 533nm with full wave half maximum of 114nm. When the surrounding refractive index of the device is changed to higher values (i.e. n=1.33 for water and n=1.377 for IPA), multiple peaks in the transmission spectra are observed. The peak wavelength is around 600nm which corresponds to metal-superstrate interface and the peak wavelength is around 650nm corresponding to metal-substrate interface. When thin layer of titanium (i.e. 9nm to 20nm) is introduced, the peak wavelength around 650nm, in both simulation and experimental results, is no longer observable which indicates that the effect of the substrate material is reduced and only prominent peak wavelengths are observed at ~530nm and at ~600nm. The peak wavelength ~600nm is sensitive to the change in the superstrate RI as it shifts to higher wavelength (red-shift) with respect to increase in the RI of superstrate. Moreover, as expected, when the adhesion layer is introduced the overall maximum transmission intensity through the sensor is decreased, from approximately six percent to one percent due to absorbance of titanium layer.

Similarly, in the simulated reflection mode, in case of no adhesion layer, a dip in wavelength at around 650 nm is observed in all three superstrates (i.e. air, water and IPA) as shown in Figure 3.3. When an adhesion layer is introduced, the dip in wavelength at around 650 nm is no longer observable. In the experimental results, when there is no adhesion layer, only single dip is observed unlike in simulation where two dips are observed in case of higher RI of the superstrate. However, the single observed dip has much higher FWHM (60-70nm) which is covering the whole wavelength region where two dips are observed in the simulation result. With the addition of an adhesion layer in case of water as a superstrate, FWHM of the dip is decreased (43nm for 20nm Ti Thickness) and this dip is sensitive to the change of RI of superstrate.

In order to study the influence of an adhesion layer on the colorimetric properties of the nanoLCA device, bright-field optical microscope images for different thickness of Ti layer (i.e. 5nm and 20nm) in transmission and reflection mode is shown in Figure 3.4 and Figure 3.5. The peak wavelength of the transmission and reflection spectrum should have lower FWHM not only for increasing overall device sensitivity but also for better colorimetric sensing, to have more distinct color. In the case of no adhesion layer, the transmission spectrum is very broad (higher FWHM) which allows all the wavelengths in that region to be transmitted. However, when an adhesion layer is introduced, starting from the 5nm of Ti, FWHM of the transmission spectrum is decreased and the filter effect is more observable, which allows better colorimetric sensing. As discussed earlier, when the RI of superstrate is increased, there is a red-shift in the maximum peak wavelength observed, which cause the transmitted image appear increasingly red as the shorter wavelengths are suppressed and the longer wavelengths are transmitted through the sensor. By analyzing the individual color channels (red, green, and blue) of the transmitted and reflected images, colorimetric effect can be measured. From this study (experimental and simulation results), it is concluded that having an adhesion layer results in sharper resonance having higher intensity and lower FWHM which is desirable for both spectral and colorimetric sensing.

3.3.2 Layer by layer deposition of polyelectrolyte layers

Electrostatic LBL assembly of polyelectrolyte films presented a method of controlling thickness and composition on variety of surfaces with known optical properties (i.e. refractive index). The film deposition process include repetitive immersion of the nanoLCA device into the solution of polycationic and polyanionic molecules. Figure 3.6 shows the schematic of the LBL deposition process, where, a positively charge polyelectrolyte is added on the negatively charged

substrate followed by negative polyelectrolyte, which will adsorbed electrostatically on the former layer. [113, 114]

There are many cationic and anionic polyelectrolytes are available, such as poly(L-lysine), sulfonated poly(styrene), poly(diallyldimethylammoniumchloride), and utilized for polyelectrolyte films deposition.[115, 116] However, we have selected Poly(allalamine) (PAH) and poly(sodium 4-styrenesulfonate) (PSS) due to well-studied protocols which are suitable for the decay length characterization of nanoLCA. The selection of the different materials having cation and anion properties are dependent on the application and protocols, the bulk properties of the film, such as density, porosity and wettability, can be controlled. LBL is one of the common way to immobilize the appropriate molecules on the surface of nanoLCA due to the simplicity of the experimental procedure and minimum numbers of reagents requirement. Nowadays, commercially available SPR system from BIACore is using a similar molecule called dextran, [117, 118], in which a linker molecule (e.g. hydroxyalkanethiol) is first immobilized on the surface of the device followed by the attachment of dextran molecules to the linker molecule. In order to form carboxylic groups, dextran molecules are further modified with bromoacetic acid after the immobilization, which can provide covalent linkage in order to attach further molecules. With the increasing number of deposited polyelectrolyte layers, there can always be inconsistency as it is executed manually. Furthermore, the acidic property of PSS solution, introduces a constraint to the total number of layers to be deposited as it is reacted with the gold surfaces.

The following analytical expression is used to calculate the decay length of the nanoLCA device,

$$\Delta\lambda = m\Delta n\left[1-\exp\left(\frac{-2d}{l_d}\right)\right]$$

where $\Delta\lambda$ corresponds to the shift in the resonant peak wavelength, m is the bulk device sensitivity (nm RIU^{-1}), Δn is the change of refractive index from the deposited polymer film (n=1.63) and the superstrate (n=1 as all the measurement are carried out in air), d is the total thickness of the deposited polymer film, and l_d is the decay length.[119] As discussed earlier, the bulk sensitivity of the nanoLCA device is measured by changing the refractive index of the superstrate material from water (n=1.33) to IPA (n=1.377) and calculating the peak wavelength shift of the plasmon resonance wavelength. The representative transmission spectra is measured after every two layers of LBL deposition and the corresponding peak wavelength shift is shown in Figure 3.7 (a) and (b) whereas Figures 3.7 (c), (d) and (e) show the corresponding colorimetric images before LBL deposition and after deposition of layers 4 and 8. Ellipsometry is used to determine the thickness of the deposited film, *d*. In order to calculate the decay length, the analytical expression is rearranged in the form of $y = m * x$, $\log\left(1 - \frac{\Delta\lambda}{m\Delta n}\right) = \left(\frac{-2}{l_d}\right) * d$ where the slope "*m*" corresponds to $\left(\frac{-2}{l_d}\right)$ and shift in the resonance wavelength is plotted against the thickness of the deposited polymer film with linear fitting, as shown in Figure 3.7 (b) to calculate the fitted slope. In order to calculate the decay length of the nanoLCA device, ten layers of the PAH-PSS polyelectrolyte layers are deposited on the superstrate. The average thickness of the polymer film is calculated as 18.2 nanometers with 4.3 nanometer of standard deviation between multiple experiments. This implies that the estimated thickness of one polymer film layer is ~ 1.82 nanometers, which is very close with the reported value of thickness in the literature i.e. ~ 1-1.5 nanometers per layer.[119] By using the analytical expression, the decay length of the nanoLCA device is calculated in the range from 120 – 200 nanometers with corresponding thickness of the polymer film which is also very consistent with the reported literature values for similar nanohole array device (see Table

3.1).[119, 120] Furthermore, to verify the experimental results, the decay length of the nanoLCA device is also calculated by depositing thin film of (10 nm) of silicon dioxide (n=1.516) using electron beam deposition and has an average of 193 nanometers with 9.6 nanometers of standard deviation.[119] The decay length is a crucial parameter to characterize for nanoLCA device since it defines the sensing region from the surface of the sensor.

Additionally, nanoLCA device is treated with different alkanethiol molecules before the LBL deposition to elucidate the effect of linker molecules. We have used decanethiol ($CH_3(CH_2)_8CH_2SH$) and 6-mercapto-2-hexanol ($SCH_2(CH_2)_4CH_2OH$) (MCH) which has a methyl terminal group and a hydroxyl terminal group respectively. As we have discussed earlier, in order to initiate the deposition of the first polyelectrolyte layer in the LBL process, a linker molecule is required. Therefore, the carboxyl terminal group with negative charge in the DTBA allows the deposition of PAH layer through the electrostatic interaction-based, which is positively charged in solution. However, there is a constraint in the growth of the polymer film by using hydroxyl or methyl-terminated groups as there is no negatively charged group to attach PAH polymer film. Moreover, decanethiol and MCH are used as a blocking solution to protect the bare gold surface of the nanoLCA device. As the bare gold surface is negatively charged, PAH tends to bind the surface of the device without any linker molecule. [119] The comparative study between DTBA-immobilized and bare surface of the nanoLCA device for LBL deposition of the polyelectrolyte layers indicates that the residual negative charge of the gold surface of nanoLCA is sufficient for LBL deposition of polymer layers without using DTBA as a linker molecule. Furthermore, the linker molecules which has a methyl terminal group and a hydroxyl terminal group are not completely blocking the gold surface to hinder the growth of the polyelectrolyte film, however,

rate of growth is effected as compare to the linker molecule (DTBA) with thiol group (Figure 3.8 and Figure 3.9).

The experiment result shows that with the 10 layers deposition of the polymer films (approximate thickness of 20 nanometers), as shown in Figure 3.8 (b) and (c), the decanethiol and MCH immobilized regions of the nanoLCA has a peak wavelength shift of 73.14 nanometers and 40.35 nanometers respectively. Whereas, the nanoLCA region which is immobilized with DTBA solution for LBL deposition of 10 layers of polymer film has a peak wavelength shift of 120.21 nanometers (Figure 3.8(a)). The difference in the growth of the polymer films on the nanoLCA device treated with blocking solution as a linker molecules can also be observed with the colorimetric images as there is a small change in color appearance after 10 layers deposition of polyelectrolyte film (Figure 3.10). These results demonstrate the effect of the linker molecules on LBL deposition such as by changing the end group of the linker molecule the first layer of polyelectrolyte deposition can be enhanced or hindered. This technique can be used for the selectively deposit the polymer films on the nanoLCA device.

3.3.3 Micro-contact printing of poly-L-lysine on nanoLCA device

Furthermore, micro-contact printing is used to deposit thin layer of polymer using polydimethylsiloxane (PDMS) stamps with an array of circular features (500 μm of diameter and periodicity) which is fabricated using soft lithography. The schematic illustration of the process is shown in Figure 3.11. There are many advantages of micro-contact printing such as accurately localized deposition of molecules, the flexibility in the shape and design geometry, cost effective method and compatibility or versatility of the technique to print wide variety of molecules. Here, we presented the deposition of poly-L-lysine with micro contact printing on the surface of nanoLCA device. The process starts with the stamps inked with the poly-L-lysine (1 mg/mL

concentration) and instantly brought in contact with the surface of nanoLCA device. Spectral and colorimetric characterizations are performed to detect the response of nanoLCA after the deposition of poly-L-lysine film on the surface of the device as shown by the microscope images in Figure 3.12. The edges of each spot can be differentiated from the bare surface using colorimetric characterization. The region where poly-L-lysine is deposited appears as yellow in contrast to the green color for the region without the polymer deposition on the nanoLCA device, in the transmission mode. The deposition of the poly-L-lysine can also be observed using scanning electron microscope (SEM) images, however, the polymer deposition inside the nanoholes is not observed (Figure 3.13 (b) and (c)). Moreover, SEM images also indicated that the region with the polymer deposition appeared brighter than the bare nanoLCA region as shown by monochromatic transmission microscopy images (Figure 3.14 (b) and (c)) at 548 nm and 600 nm respectively showing transmitted light intensity differences between the bare and the poly-L-lysine deposited regions for visible distinction. This is caused by the non-conducting dielectric material (in this case poly-L-lysine). The deposition of poly-L-lysine can also be identified using spectral measurement and there is a 20.8 nanometers of peak wavelength shift is observed from the bare region of the nanoLCA device as shown in Figure 3.14 (a).

3.4 Conclusion

In this chapter first we have discussed the influence of adhesion layer on both spectral and colorimetric properties of the nanoLCA device in transmission and reflection mode. FDTD simulation is performed to investigate the localized electric field confinement at different interfaces of the nanoLCA device and presented the optimized thickness for better sensitivity. Furthermore, the nanoLCA plasmonic device has demonstrated high sensitivity for both spectral

and colorimetric measurement of monolayers of biomolecular interaction on the device surface. We used LBL deposition of alternating polyelectrolyte layers at 2nm resolution to determine the sensing depth (decay length) of the nanoLCA plasmonic device as ~193 nanometers. Furthermore, the nanoLCA plasmonic device was treated with different alkanethiol linker molecules layers and the growth of LbL polyelectrolyte films shows strong dependence on linker molecules. Finally, micro-contact printing was used to selectively transfer and create microscale patterns of poly-L-lysine molecules on the nanoplasmonic device and the label-free colorimetric imaging of the patterned molecular depositions was demonstrated. The nanoLCA device is proven to be a platform of direct visualization of various surface molecular interactions at monolayer thickness resolutions.

3.5 Figures and tables

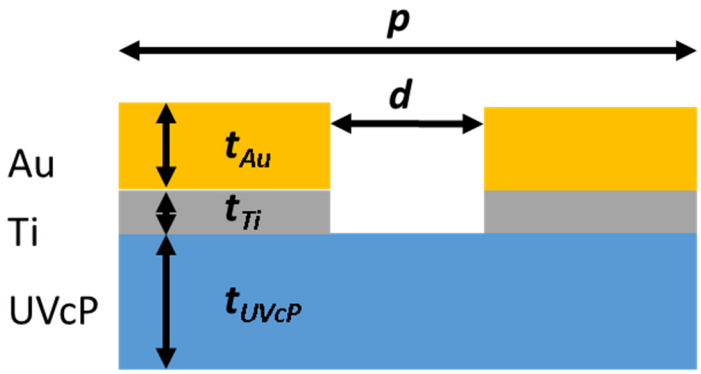

Figure 3.1 Schematic illustration of the nanohole array (in nanoLCA) with UV-curable polymer (UVcP), titanium (Ti) and gold (Au) layers. Thickness of each layer is indicated by t with subscript referred to the specific layer with the periodicity (*p*=350nm) and diameter (d=100nm) for FDTD simulation. Adapted from [121].

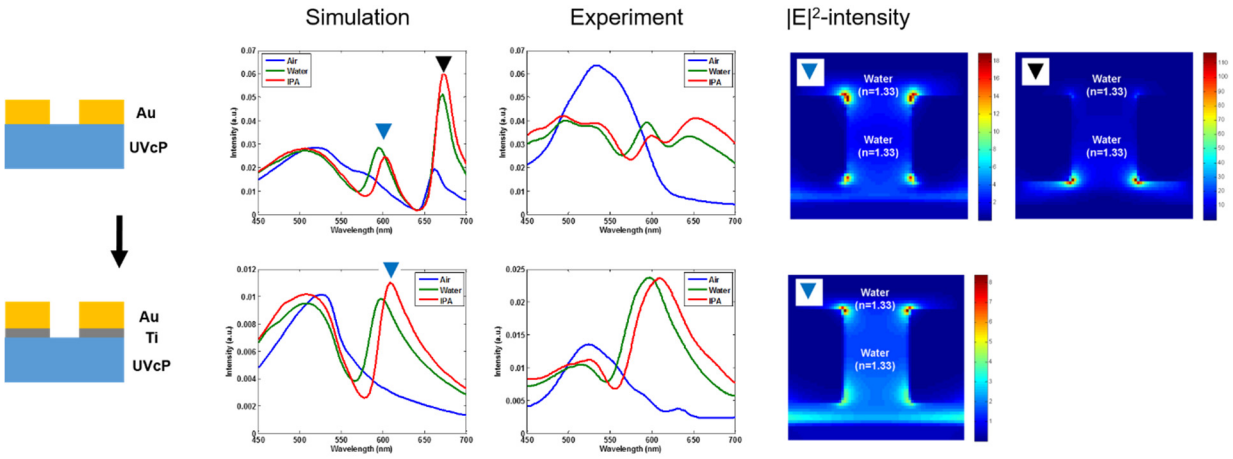

Figure 3.2 The transmission spectra of the nanoLCA with and without the adhesion layer is compared with simulation and experimental results and corresponding FDTD simulation for E-field distribution on the cross-section of the device at selected wavelengths (indicated by blue and black triangles). Adapted from [121].

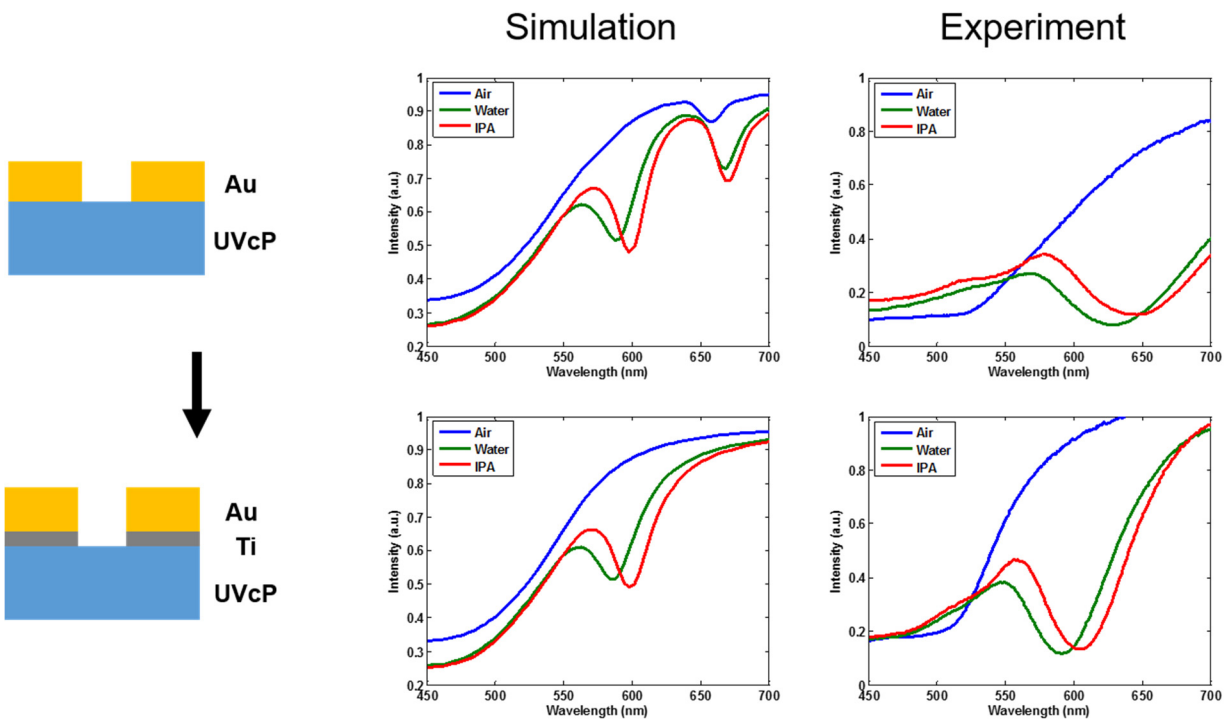

Figure 3.3 The reflection spectra of the nanoLCA with and without the adhesion layer is compared with simulation and experimental results. Adapted from [121].

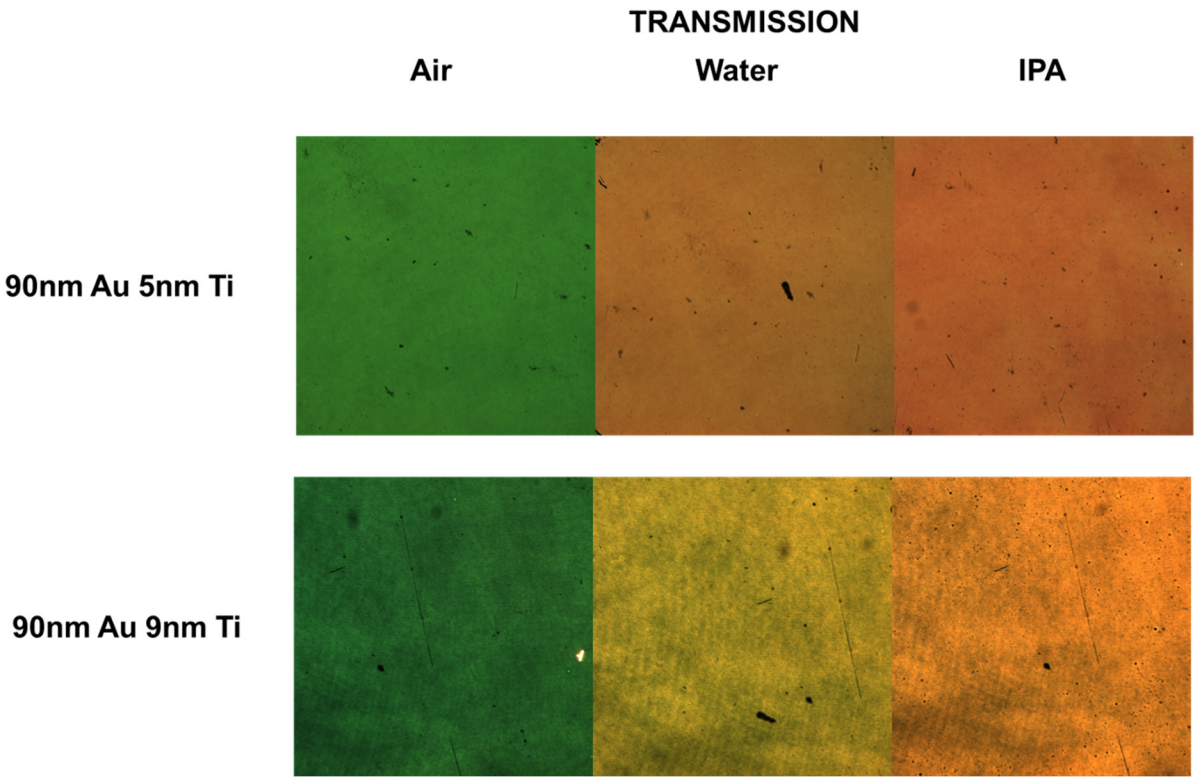

Figure 3.4 Colorimetric sensing is performed using bright-field optical microscope images of the nanoLCA device with different thickness of Ti layer. Transmission images of the device with 5 nm Ti layer and 9nm Ti layer are shown on top row and bottom row respectively, with the superstrate exposed to air, water, and isopropanol (IPA). Adapted from [121].

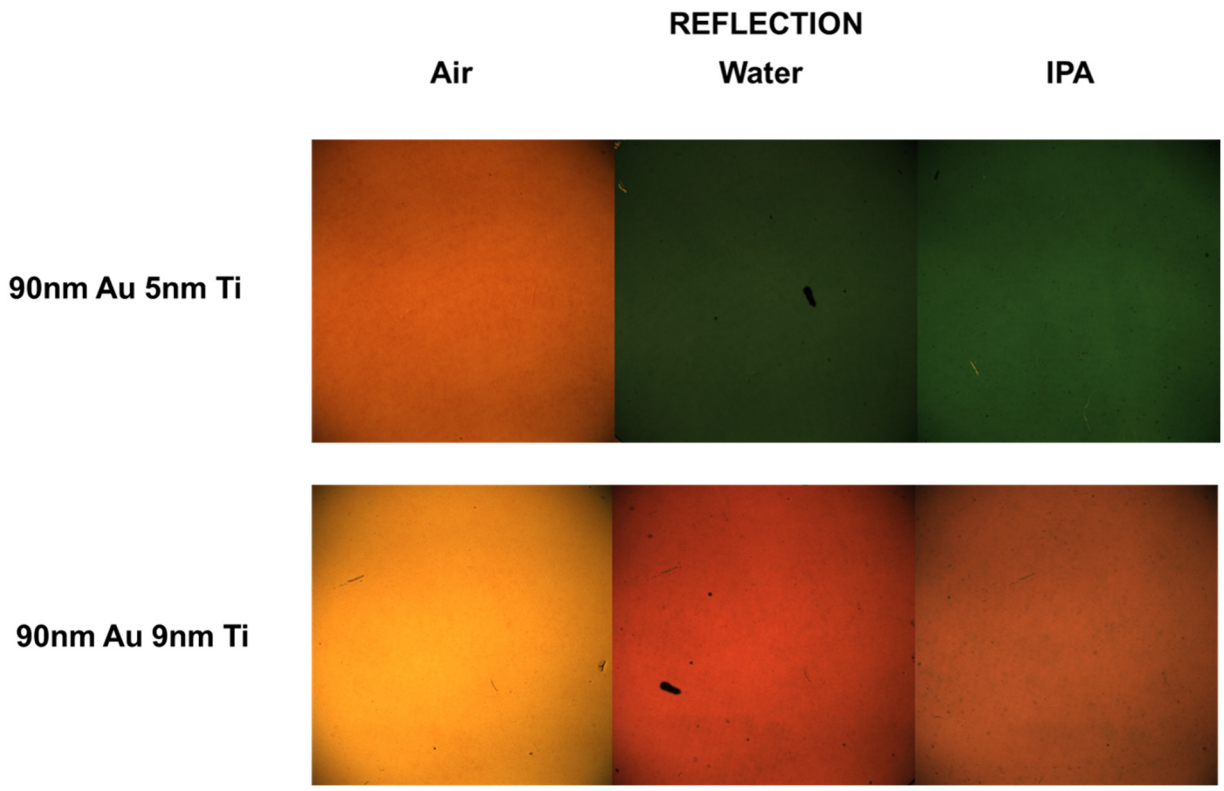

Figure 3.5 Colorimetric sensing is performed using bright-field optical microscope images of the nanoLCA device with different thickness of Ti layer. Reflection images of the device with 5 nm Ti layer and 9nm Ti layer are shown on top row and bottom row respectively, with the superstrate exposed to air, water, and isopropanol (IPA). Adapted from [121].

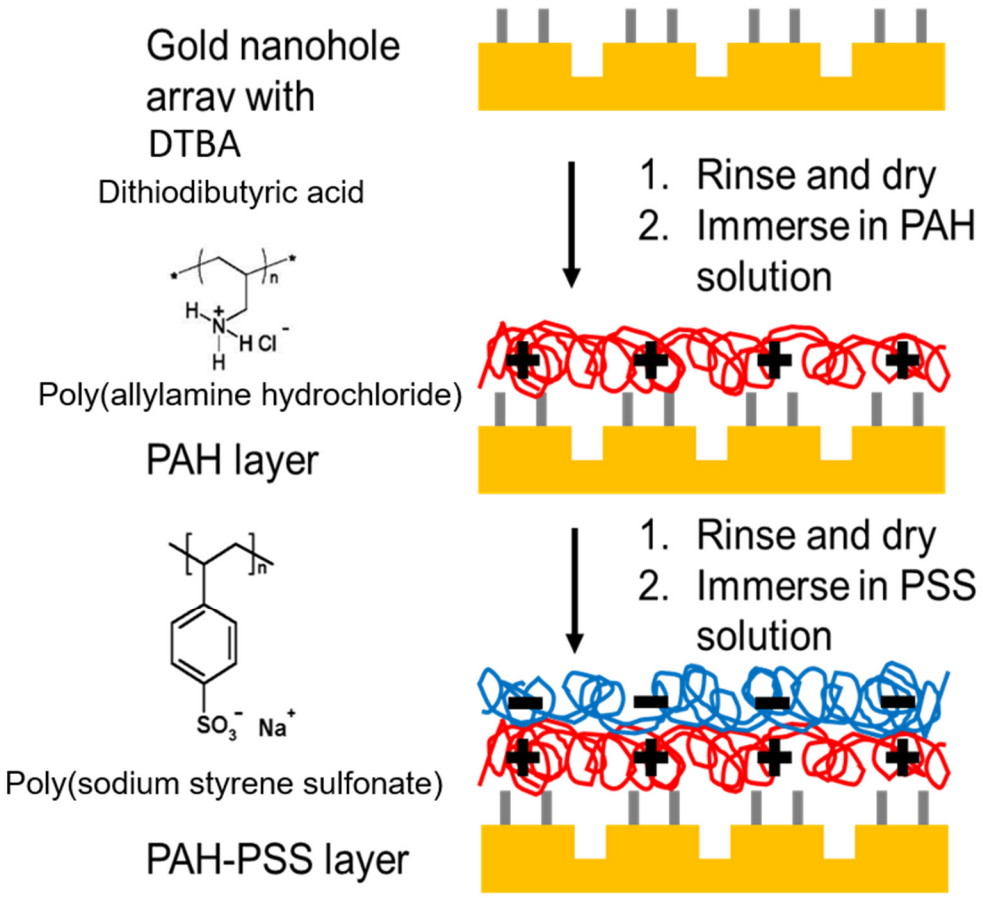

Figure 3.6 Schematic of the layer-by-layer (LbL) deposition process. The nanoLCA device is immersed in 33mM of dithiodibutyric acid (DTBA) in ethanolic solution for 24 hours to form a self-assembled monolayer with a carboxyl terminal. After the immersion, the device is rinsed thoroughly with ethanol and dried with Nitrogen flow. For LBL deposition, the device is immersed in Poly(allylamine) (PAH) solution for 5 minutes followed by the immersion in Poly(sodium 4-styrenesulfonate) (PSS) for 1.5 mins. The immersion step is repeated until the desired thickness of the film achieved. Adapted from [121].

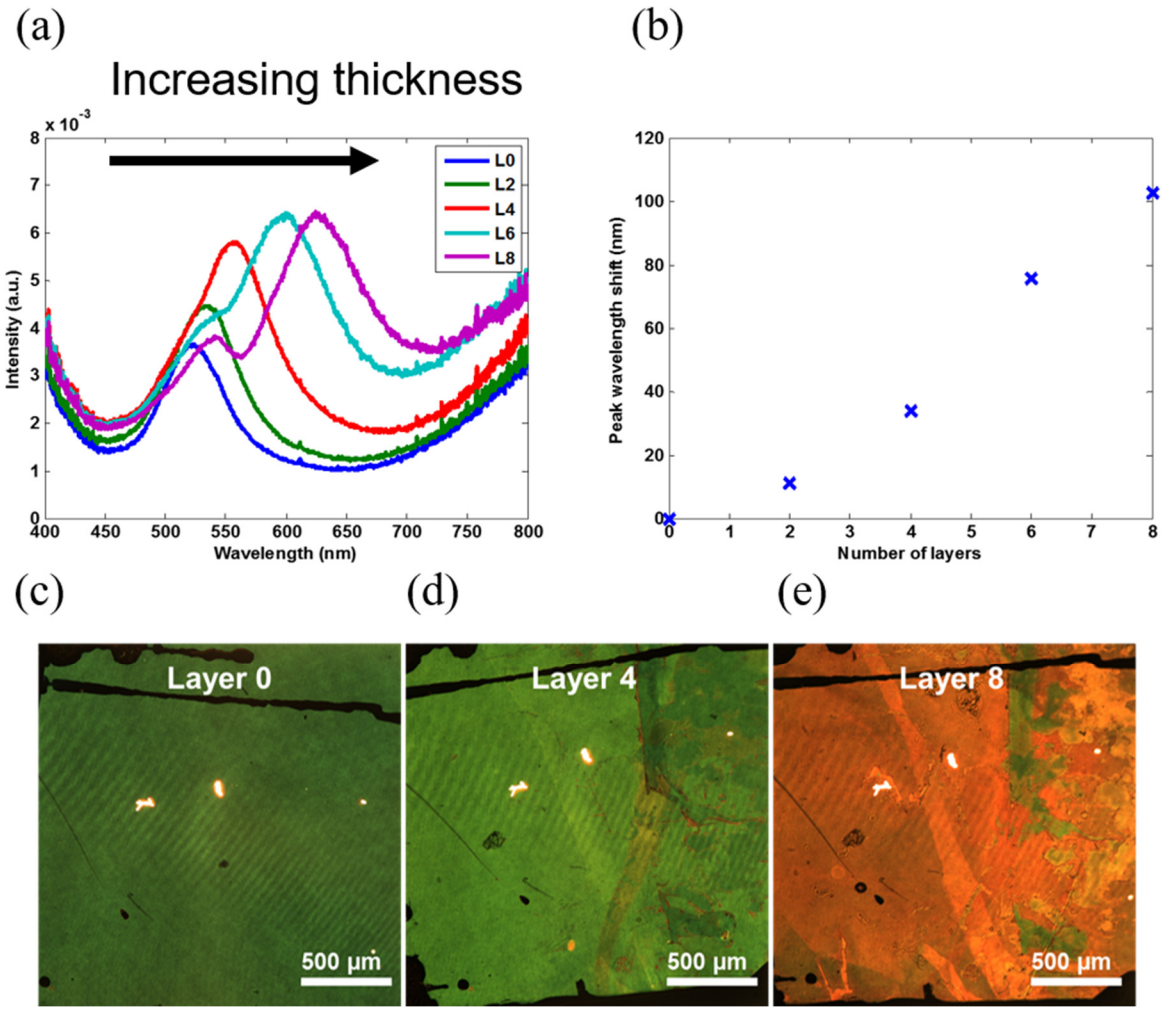

Figure 3.7 (a) Transmission spectra of nanoLCA device shows red-shift of the maximum transmission peak λ_{peak} by adding polyelectrolyte layers. (b) The shift in the resonance peak wavelength λ_{peak} of the maximum transmission is plotted as a function of the number of polyelectrolyte layers. (c), (d), and (e) shows colorimetric transmission microscope images of the nanoLCA device. It can be observed that the color appearance to be more red with the increase of polyelectrolyte layers. Adapted from [121].

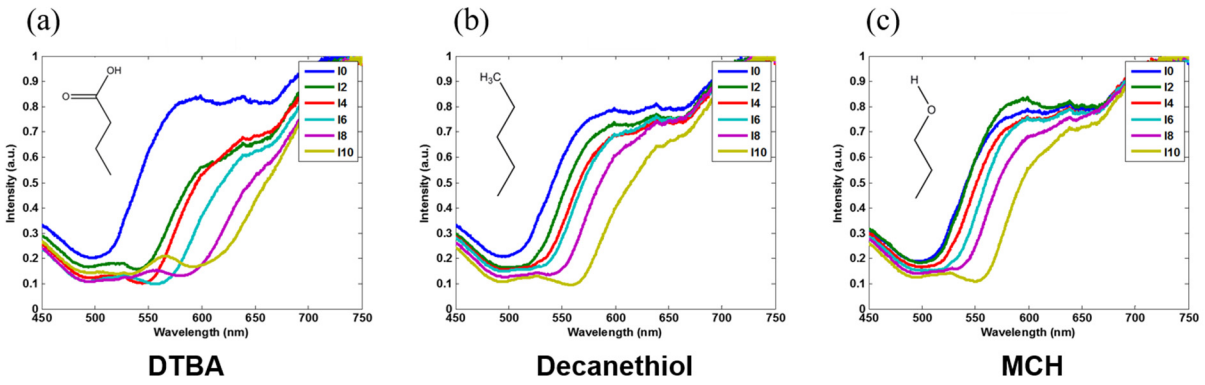

Figure 3.8 Reflection spectra of nanoLCA for LBL deposition exposed with DTBA (a), Decanethiol (b), and MCH (c) for the linker molecules. The spectra were taken after every two layers of polyelectrolyte layers deposition. Adapted from [121].

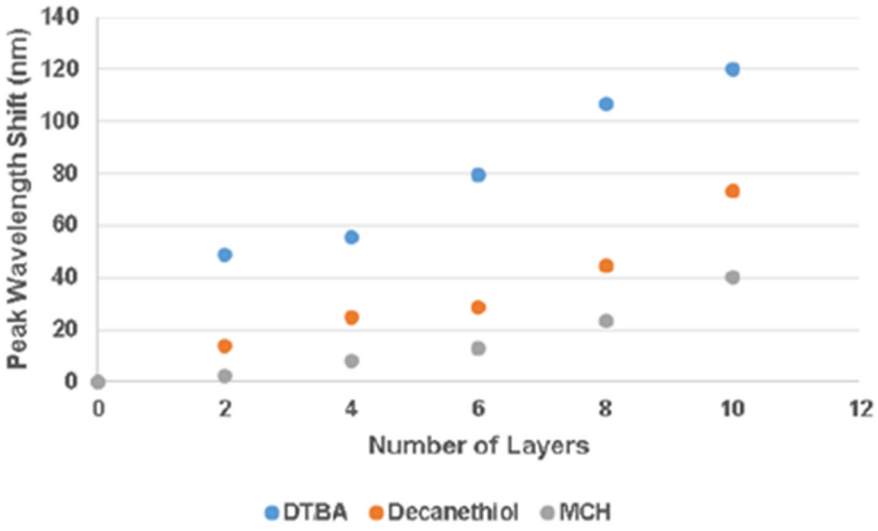

Figure 3.9 Shift in the resonant peak wavelength of the nanoLCA device due to the LBL deposition of polyelectrolyte layers after the treatment of DTBA, Decanethiol and MCH. Adapted from [121].

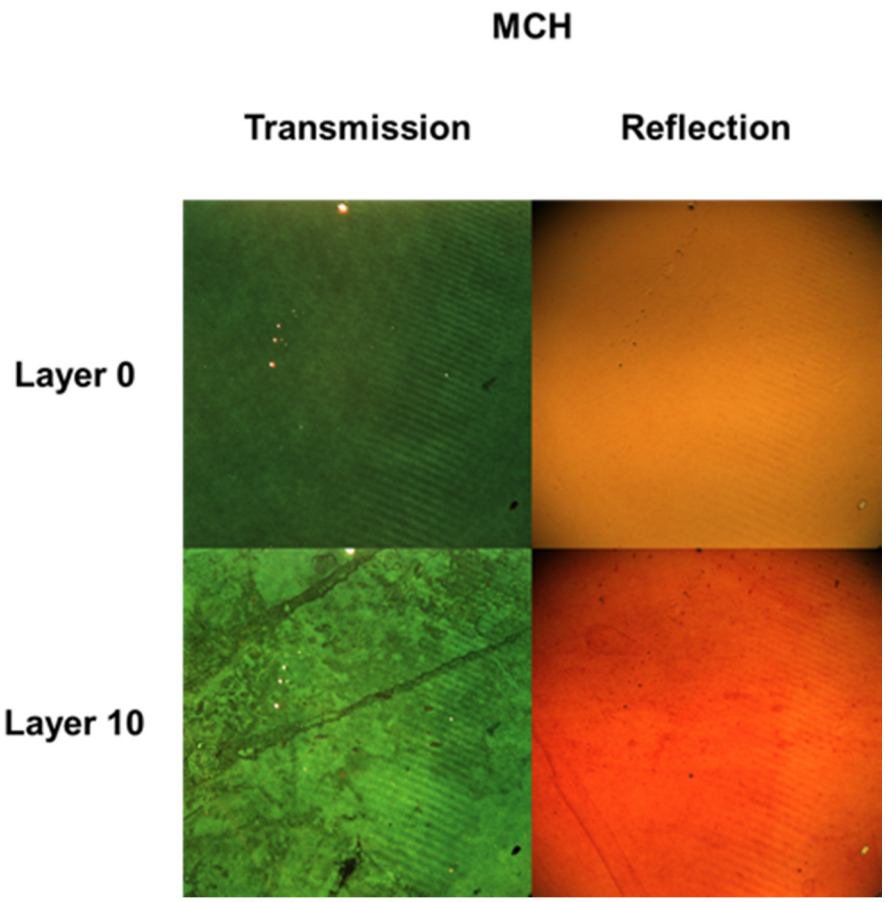

Figure 3.10 Colorimetric images of the nanoLCA device without LBL deposition (top row) and with 10 LBL deposition (bottom row) of polyelectrolyte layers after the treatment of MCH (blocking solution) as a linker molecule in both transmission and reflection mode. Adapted from [121].

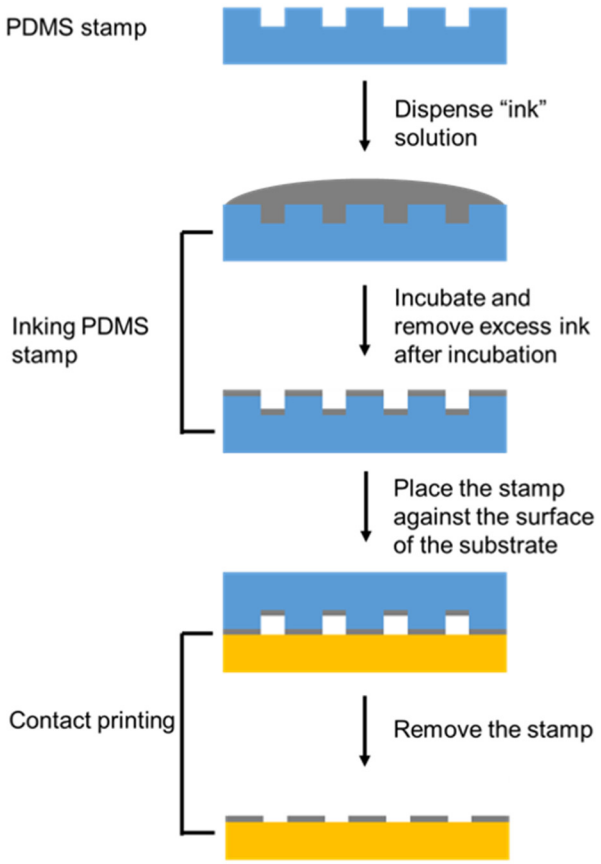

Figure 3.11 Schematic illustration for the process of micro-contact printing on nanoLCA device. Adapted from [121].

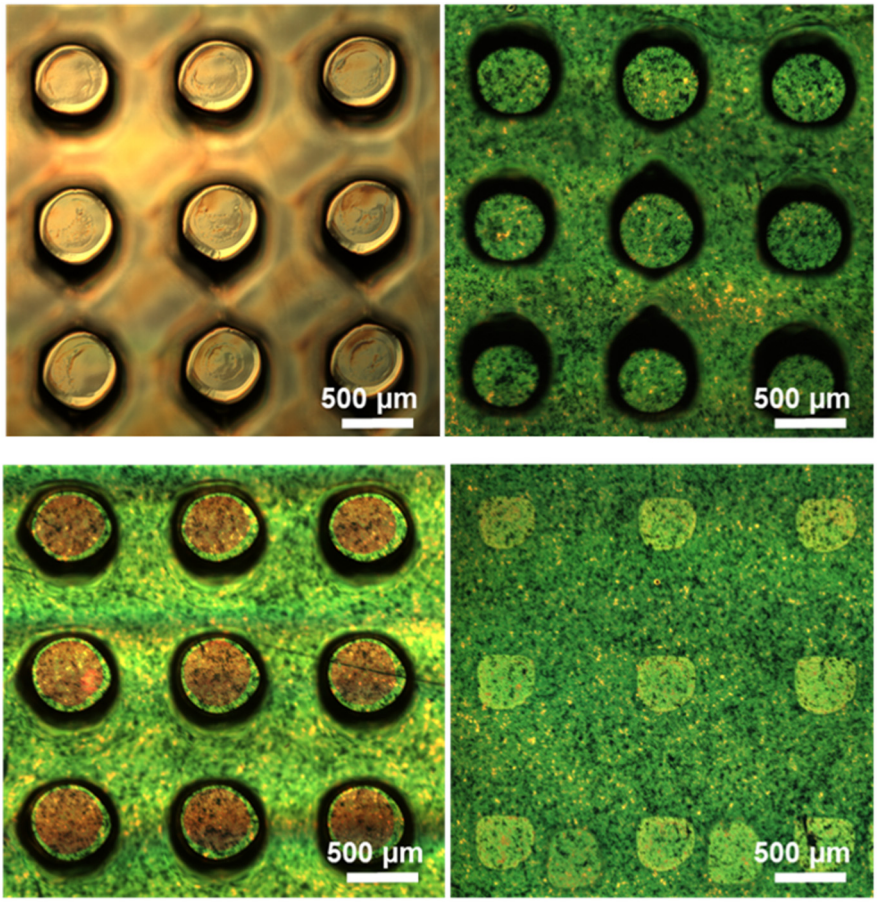

Figure 3.12 Optical microscope images of the micro-contact printing of poly(L-lysine) on nanoLCA device. (Top left) Polydimethylsiloxane (PDMS) stamp having 500-micron diameter circular structures same periodicity. (Top right) Bare PDMS stamp placed on the nanoLCA device without making in contact. (Bottom left) Bare PDMS stamp placed in direct contact with the surface of the nanoLCA device. (Bottom right) array of poly(L-lysine) deposited on the surface of the nanoLCA device by micro-contact printing and bright green areas referred to the poly(L-lysine) deposition.

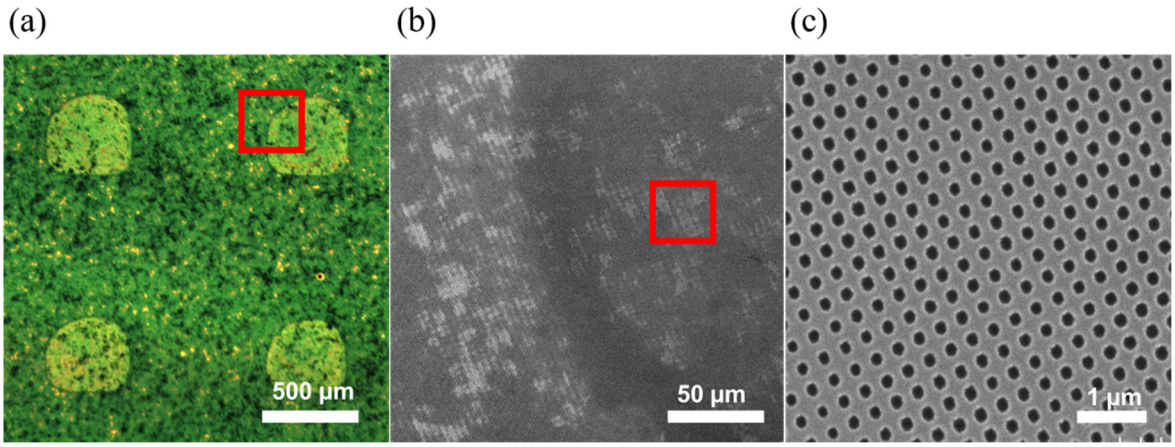

Figure 3.13 Microscope images for the characterization of the poly(L-lysine) deposited region on the nanoLCA device. (a) Optical microscope image of the poly(L-lysine) deposited region by micro-contact printing. (b) Scanning electron microscope (SEM) image at 400× magnification to show the boundary edge between bare and poly(L- lysine) deposited regions with the observation of distinct intensity contrast. (c) SEM image at 15k× magnification to identify the deposited region with poly(L-lysine) on the individual nanoholes of the nanoLCA device. Adapted from [121].

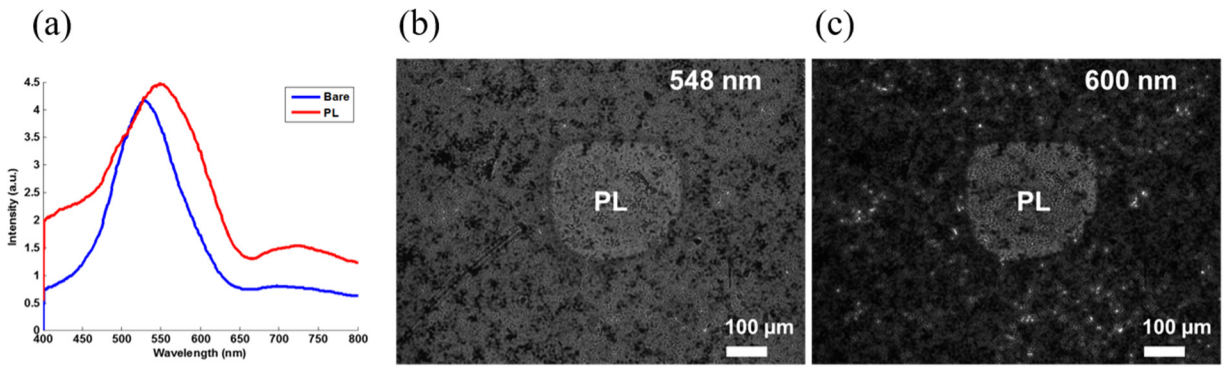

Figure 3.14 Comparison of spectral and colorimetric intensities between bare and poly(L-lysine) deposited regions on the nanoLCA device. (a) Transmission spectra of the bare and the poly-L-lysine deposited regions on the nanoLCA device, indicating a resonant peak wavelength shift to longer wavelengths range. (b and c) Monochromatic transmission microscopy images at 548 nm and 600 nm respectively showing transmitted light intensity differences between the bare and the poly-L-lysine deposited regions for visible distinction. Adapted from [121].

Tables 3.1 Decay length comparison between different surface plasmon resonance-based sensors. EOT: Extraordinary Optical Transmission, SPR: Surface plasmon resonance, LSPR: Localized surface plasmon resonance.

Type of sensor	**Periodicity (nm)**	**Decay length (nm)**	**Reference**
nanoLCA	350	120-200	Present study
EOT (Au)	1000	140	[119]
SPR on Au nanohole array	1000	200-300	[119]
Gold film	n/a	200-300	[119]
LSPR (Nanoparticles)	n/a	5-15	[122, 123]

CHAPTER 4

SUBSTRATE BINDING TO CYTOCHROME P450-2J2 IN NANODISCS DETECTED BY NANOSCALE LYGURCUS CUP ARRAYS

Cytochrome P450s are the primary enzymes involved in phase I drug metabolism and highly sought-after screening targets for early drug discovery research. However, high-throughput drug screening of P450s is limited by low protein stability and lack of consistent measurement of binding events. CYP2J2 is the most common P450 found in the human heart.[124, 125] Its primary responsibility is the metabolism of arachidonic acid. This produces epoxyeicosatrienoic acids (EETs), which are required for proper cardiovascular function due to their vasorelaxation, anti-inflammatory, pro-fibrinolytic, and pro-angiogenic effects.[126, 127] However, high-throughput drug screening of P450s is limited by low protein stability and lack of consistent measurement of binding events. All human cytochrome P450s are membrane bound and they tend to become unstable and inactive in solution or otherwise. In order to circumvent this challenge, Nanodiscs (ND) are used to stabilize CYP2J2 which consist of nanosized soluble lipid bilayers held together by two surrounding membrane scaffold proteins.[128, 129] Here we present the detection of substrate binding to cytochrome P450-2J2 (CYP2J2), using a combination of Nanodisc technology and nanoplasmonic Lycurgus cup array (nanoLCA). Absorption spectroscopy of seven different substrates binding to CYP2J2 in solution showed that they are all type I, resulting in shifting of the protein bands to lower wavelengths (blue shift). Detection on the nanoLCA sensor also showed spectral blue shifts of CYP2J2 following substrate binding. Finite Difference Time Domain (FDTD)-based electromagnetic simulation suggested that the blue shift is because of the hybridization of plasmon polariton Bloch wave and the electronic resonance of the heme group of

CYP2J2. We found the plasmonic properties of the nanoLCA sensor to be highly reproducible, which allowed comparisons among the different substrates at different concentrations. Further, due to the unique spectral properties of the nanoLCA sensor, including the transmission of a single color, we were able to perform colorimetric detection of the binding events. These results indicate that a resonance plasmonic sensing mechanism can be used to distinguish between different drugs at different concentrations binding to P450s and that the nanoLCA sensor has the potential to provide consistent high-throughput measurements of this system.

4.1 Introduction

The development of a high-throughput label-free method for detecting substrate binding to cytochrome P450s would have a significant impact on early stage drug discovery research. P450s are primarily membrane bound and responsible for phase I metabolism of approximately 75% of current pharmaceuticals.[130] In addition to their crucial roles in xenobiotic metabolism, P450s are responsible for important drug-drug interactions which can potentially lead to drug toxicity and fluctuations in protein enzymatic activity.[131-133] Several challenges limit the applicability of current methods for detecting drug binding to P450s. The first is that the proper expression, isolation, and purification of these proteins at a high yield is labor intensive.[134] A detection mechanism with a high sensitivity is therefore required in order to minimize the protein concentration and sample volume. In addition, most eukaryotic P450s are membrane-bound and outside the cellular environment they tend to denature and become unstable both in solution and when immobilized on surfaces.[135, 136]

Currently drug binding to P450s is detected using absorbance-based spectroscopic assays in solution.[137] Detection is based on the fact that after drug binding P450s can shift the

absorbance peak at 417nm (Soret band) to either shorter wavelength (blue shift, type I binding) or to higher wavelength (red shift, type II binding).[138-141] However, solution-based methods of detection require a high sample volume.[142] It is expected that a surface-based sensing mechanism has the potential to increase sensitivity and therefore decrease the required sample volume, allow for parallel on-chip detection, and provide a more stabilized detection method of substrate binding.

Among the currently available surface-based sensing mechanisms, label-free optical sensors, such as the photonic crystal [143], ring resonator [144], interferometer [145],and surface plasmon resonance (SPR) [146, 147] can be miniaturized due to breakthroughs in nanofabrication and therefore are especially promising for on-chip drug screening applications. However, these techniques remain limited by the complex and bulky external optical systems required for signal generation, detection, and analysis. SPR sensors measure a change in the resonance condition corresponding to a refractive index change due to interactions between an immobilized biomolecule on a metallic thin film and its binding partner. While SPR provides a sensitive detection mechanism for protein-protein and protein-molecule interactions, its application to high-throughput drug discovery research is limited due to the complex optical system required.

Plasmonic biosensing can also be accomplished using localized surface plasmon resonance (LSPR) or extraordinary optical transmission (EOT). In LSPR, the electric field near metal nanoparticles is amplified resulting in strong scattering spectra ideal for applications in protein biosensing.[148, 149] Because this relies on metal nanoparticles and not a metallic thin film, it does not require a complex optical system in order to couple the light source to the metal dielectric interface.[150] However, the resulting sensitivity is at least an order of magnitude less than SPR in the Kretschmann configuration. Considerable work has gone into the application of fabrication

methods with increasing precision, such as nanosphere lithography and electron beam lithography, to form 2D and 3D spatial arrangements of silver and gold nanoparticles, which has increased the sensitivity of LSPR sensors.[151, 152] However, the difficulty in fabricating uniform sensors over a large surface area leads to reduced reliability, inconclusive results, and limited applications.

EOT sensors consist of periodic arrays of nanoholes, typically fabricated by focused ion beam milling, in metallic thin films.[153] It has been shown that transmission through these films is orders of magnitude greater than that predicted by classical aperture theory partially due to the excitation of surface plasmon resonances.[40] This reliance on SPR allows the device to operate as a refractive index sensor and demonstrated applications include protein binding [154], exosome profiling [155], and virus detection [156]. Similar to LSPR-based measurements, these sensors do not require a complex optical setup, but it is difficult to fabricate uniform devices over a large surface area.

LSPR sensing has been applied previously to detect drug binding to P450s. In particular, it has been shown that if there is an overlap between the device resonance and the P450 molecular resonance, primarily due to the Soret band, then resonance LSPR can result in larger shifts that are easily identifiable.[157] Small molecule binding can then be detected by measuring the corresponding spectral shift due to the protein.[158] The ability to distinguish between type I and type II substrates has been previously demonstrated using silver LSPR sensors fabricated by nanosphere lithography.[159] The further development of LSPR detection of substrate binding to P450s requires nanoplasmonic sensors that are compatible with wafer-scale fabrication. The resulting devices must have minimum defects and therefore consistent spectral properties. In addition, while silver nanoparticles have a higher sensitivity to the local refractive index change,

gold nanoparticles are inert and therefore more compatible with high-throughput drug screening.[160, 161]

Herein we report the application of a gold nanoplasmonic Lycurgus cup array (nanoLCA) sensor to the detection of substrate binding to P450s. The tapered nanohole shape of the nanoLCA has a metal layer (90 nm) at the rim of the holes and at the bottom of the holes (90 nm), providing an intense electromagnetic field at the bottom and top of the nanohole due to LSPR.[64] The periodicity of nanohole structures also provide surface plasmon polariton-Bloch wave (SPP-BW) due to lattice plasmons. The nanoLCA sensor then operates based on a distinct combination of SPP-BW and LSPR plasmonic properties.

While the nanoLCA can be applied to measure drug binding to any P450, here the detection of substrate binding to cytochrome P450-2J2 (CYP2J2) is demonstrated. CYP2J2 is the most common P450 found in the human heart.[124, 125] Its primary responsibility is the metabolism of arachidonic acid. This produces epoxyeicosatrienoic acids (EETs), which are required for proper cardiovascular function due to their vasorelaxation, anti-inflammatory, pro-fibrinolytic, and pro-angiogenic effects.[126, 127] Additionally, CYP2J2 metabolizes drugs, many of which have been shown to be cardiotoxic. Therefore, it is of interest to ensure that drugs or xenobiotics do not interfere with the enzymatic activity of CYP2J2 with respect to arachidonic acid metabolism.

The first requisite is to develop a method to screen for substrate binding to CYP2J2 in a high-throughput fashion. It is important to note that the use of nanoLCA for detection of substrate binding to CYP2J2 is widely applicable to detect drug binding of any pharmaceutically relevant drug metabolized by P450s. All human cytochrome P450s are membrane bound and they tend to become unstable and inactive in solution and on surfaces. In order to circumvent this challenge, here we use Nanodiscs to stabilize CYP2J2. Nanodiscs consist of nanosized soluble lipid bilayers

held together by two surrounding membrane scaffold proteins.[128, 129] The use of Nanodiscs is critical for this study because they provide a bilayer to stabilize membrane-bound proteins in a native environment. This ensures that the CYP2J2 proteins will be immobilized on the nanoLCA sensor surface in an active conformation.

In addition to the Nanodisc technology, the mechanism reported here requires the nanoLCA sensor and resonance LSPR in order to detect the shift corresponding to the spectral change of CYP2J2 Nanodiscs (CYP2J2-NDs) following substrate binding. The resonance of the nanoLCA sensor occurs in the visible range, allowing detection of shifts in the transmission spectrum by a conventional halogen light source and portable spectrometer. Here we report the measurement of the spectral change in CYP2J2-NDs corresponding to the binding of seven different type I substrates at two different concentrations and the comparison of these results with conventional solution-based absorption spectroscopy. We also report the spectral reliability of the nanoLCA sensor, which allows for the assessment of substrate dependent and concentration dependent shifts. Finally, since the sensor spectral properties are characterized by a single transmission peak in the visible, we introduce the potential use of bright-field microscope images in order to detect substrate binding to CYP2J2-NDs on the nanoLCA device.

4.2 Materials and methods

4.2.1 Materials

Human CYP2J2 cDNA was obtained from OriGene (Catalog No. SC321730) and modified.[147] Ampicillin, arabinose, chloramphenicol, IPTG and Ni-NTA resin were obtained from Gold Biotechnology and Sigma. δ-aminolevulinic acid was bought from Frontier Scientific. 1-palmitoyl-2-oleoyl-sn-glycero-3-phosphocholine (POPC) and 1-hexadecanoyl-2-(9Z-

octadecenoyl)-sn-glycero-3-phospho-L serine (POPS) were purchased from Avanti Polar Lipids, Inc. AA, 2-AG, and MSPPOH were purchased from Cayman Chemical. Other drugs were purchased from the following companies: MP Biomedical (Danazol), Santa Cruz Biotechnology (Ebastine), and Gold Biotech (Doxorubicin). All other materials and reagents used were purchased from Sigma and Fisher Scientific.

4.2.2 Recombinant expression of CYP2J2 in E. coli

Recombinant expression of D34 CYP2J2 was prepared according to previous methods.[162, 163] Briefly, a starter culture of DH5α *E. coli* cells containing CYP2J2 and pTGro7 chaperonin plasmids were grown in 25 mL of Luria Bertani (LB) media containing the antibiotics chloroamphenicol (20 μg/mL) and ampicillin (100 μg/mL) at 37ºC and 220 rpm overnight. This culture was then used to inoculate 6 x 500 mL of Terrific Broth (TB) containing chloroamphenicol (20 μg/mL) and ampicillin (100 μg/mL). The culture was grown for 2.5 hours at 37ºC and 220 rpm. 0.1mM δ-aminolevulinic acid was added and the culture was grown at 26ºC and 160 rpm until OD_{600} = 1.0 was reached. Cells were induced with 1mM Isopropyl β-D-1-thiogalactopyranoside (IPTG) and 2 g of arabinose and left to grow for 44 hours. The cells were subsequently centrifuged at 8,000 rpm and 4ºC for 15 min. using a Sorvall GSA (Thermo Scientific, Pittsburg PA) rotor. The cells were resuspended in a lysis buffer containing 0.1mM DTT, 0.2mM phenylmethanesulfonylfluoride (PMSF), and 5 mg DNase, and then lysed via sonication (5 x 30 sec on/off cycles). The membrane fraction was isolated using ultracentrifugation at 35,000 rpm and 4ºC for 30 min. with a Ti-45 rotor (Beckman, Coulter, Brea, CA). The pellet was resuspended in 0.1M potassium phosphate buffer (KPi) containing 1.0% (w/v) sodium cholate, 20% glycerol, and 0.2M NaCl (column buffer) at 4ºC for four hours with stirring in order to extract the protein. The insoluble fraction was removed via a second ultracentrifugation at 35,000 rpm

and 4ºC for 30 min. and the supernatant was applied to a Ni-NTA column to purify His-tagged CYP2J2. Protein was eluted using column buffer containing 200mM imidazole. The yield of the protein was ~200nmol/L.

4.2.3 Incorporation of CYP2J2 into nanodiscs

Nanodiscs were prepared as previously described.[162] A lipid mixture of 20:80 POPS:POPC in $CHCl_3$ was dried under a flow of N_2 gas. The dried lipids were then reconstituted in buffer containing 0.1M KPi (pH 7.4) and 200mM cholate. Membrane scaffold protein MSP1E3D1 was added (1:130 MSP:lipids) and allowed to incubate for half an hour at 4ºC. Purified CYP2J2 was then added (0.1M Kpi (pH 7.4), 20% glycerol, and 0.1% cholate) in a 1:10 CYP2J2:MSP ratio and incubated for one more hour before the addition of Amberlite beads to remove the detergent. This mixture was incubated overnight. Discs were purified via size-exclusion chromatography using an Alliance 2695 analytical separation module (Waters, Milford, MA) coupled to a Waters 996 photodiode array detector (Waters) and a Superdex 10/200 column (GE Healthcare).

4.2.4 Drug binding to CYP2J2 nanodiscs in solution

Substrate binding was determined by monitoring the Soret shift from 420-390 nm. Absorbance spectra were taken using a Cary Bio 300 UV-Vis spectrophotometer (Agilent Tevhnologies, Santa Clara, CA). An initial spectrum of CYP2J2 Nanodiscs in 0.1M KPi (pH 7.4) was taken at 37ºC. Substrates were then titrated into this cuvette to saturating amounts. Total volume of organics remained <2% of the initial volume. To correct for the absorbance of the substrates, separate titration experiments were performed using empty Nanodiscs (without CYP2J2), and these readings were subtracted from the CYP2J2-Nanodisc spectra.

4.2.5 NanoLCA fabrication and characterization

The tapered nanohole array was made using a previously described method.[64] Briefly, the plasmonic structures were prepared using a replica molding process. The mold consisting of a two dimensional square array of nanocup structures with a lattice constant of ~ 350nm was first prepared on a glass substrate using laser interference lithography. The two-dimensional square array was transferred to a flexible and optically transparent polyethylene terephthalate (PET) film by nanoreplica molding. To prepare the master substrate for transfer, the mold was cleaned and silanized (Repel-silane ES GE Healthcare, Sigma) for 30 min. followed by ethanol and DI water rinse. A 2 mL drop of UV-curable polymer (NOA-61) was evenly spread on the top of the nanocone master and a supporting PET sheet was carefully put on top of the polymer. The master with the polymer and PET sheet was then exposed to UV-light (105mW cm^{-2}) for 60 sec. After curing, the complimentary nanohole structures were transferred onto the polymer, which was peeled off carefully from the master mold to complete the transfer process. In order to make the device surface plasmon active, 90 nm of gold along with a 5 nm titanium adhesive layer was deposited using electron beam deposition (Temescal six pocket E-Beam Evaporator).

4.2.6 Immobilization of CYP2J2-nanodiscs on nanoLCA and spectral measurements

A square device with a 2 cm side length was cut from the prepared nanoLCA and it was cleaned with isopropanol (IPA) and DI water followed by rinsing with IPA and drying with N_2. The sensor was then treated with oxygen plasma (PICO plasma cleaner) for 60 sec. and four separate circular wells were formed on the surface using PDMS applied with UV curable polymer. Each well held 45 µL of solution. To being CYP2J2-ND immobilization, each well was filled with a 10mM 11-MUA solution in 70% ethanol and incubation was done at room temperature for 24

hours. After immersion, each well was washed three times in 70% ethanol followed by drying with N_2. CYP2J2-ND immobilization to the MUA monolayer occurred by EDC activation. Each well was filled with 10mM EDC and 8μM CYP2J2-ND in 10mM potassium phosphate (KPi) buffer. The EDC and protein were mixed immediately before pipetting into the wells in order to minimize EDC self-reaction and CYP2J2-ND cross-linking. The sensor was incubated in the CYP2J2-ND solution for 1 hour at 37°C. After incubation, each well was rinsed three times with DI water and dried with N_2. Illumination and detection of binding events was accomplished with an upright microscope (Olympus BX51, PA, USA) with a halogen light source using a 20X objective and a portable spectrometer (Ocean Optics, Dunedin, FL). Successful immobilization of MUA and CYP2J2-ND was monitored by measuring the red shift in the transmission spectrum for each well of each device.

4.2.7 Substrate binding to CYP2J2-nanodiscs on nanoLCA

A device containing 4 PDMS wells was used for a single substrate. Two of the wells were replicates used for a high concentration of the substrate, one well was used for a low concentration of the substrate, and the fourth well was used for the vehicle control, which was 10mM KPi buffer. The seven substrates tested were the fatty acids Arachidonic Acid (AA) and 2-Arachidonoylglycerol (2-AG), and the drugs Doxorubicin (DOX), Ebastine, MSPPOH, Terfenadine (TFN), and Danazol (DAN). Incubation was done for 30 minutes at 37°C. The dissociation constants for all drugs with CYP2J2-ND were measured using solution-based titrations and the maximum value was 20μM. For the high concentration 300μM was used and for the low concentration we used a value that was half of the measured dissociation constant for each drug. After incubation, each well was rinsed with DI water three times and dried with N_2 before taking the transmission spectrum.

4.2.8 Data analysis

The light source transmission spectrum was measured after each binding step. Every transmission spectrum was then normalized with the light source spectrum for that step in order to obtain the transmissivity and was then smoothened by the Loess Method using OriginPro 9.1 (Origin Labs Inc., Northhampton, MA). It is expected that with a binding event there will be a corresponding shift in the plasmon resonance peak as well as a change in the peak intensity. Here the focus is on the spectral shift and not the intensity change; therefore all transmissivity data was normalized to one in order to better visualize the peak shifts. A Gaussian fit was then performed on each peak in order to obtain the plasmon resonance peak wavelength for each step using OriginPro 9.1 (Origin Labs Inc., Northhampton, MA). The solution-based absorbance data was processed using Matlab R2014a (Mathlab Inc., MI) by subtracting the substrate-free spectrum from each titration spectra. The resulting peak and trough differences were then plotted and fitted to the Michaelis-Menten equation using OriginPro 9.1 (Origin Labs Inc., Northhampton, MA).

4.2.9 3D-FDTD simulation

3D-FDTD (finite differential time domain) electromagnetic numerical computation was performed by using the FDTD software package from Lumerical Solutions. The total simulation region was set to 350 nm× 350 nm× 800 nm. The boundary conditions in x and y directions were set to be periodic to present the array effect of nanoLCA device. The perfect matching layer (PML) was applied in z-directional boundary condition to minimize the simulation error from boundary reflection. The x-axis polarized plane wave was set to propagate normal to the substrate (-z direction). The modeling of nanostructure was based on the observation of SEM images of nanoLCA device. The mesh size was set to be 5 nm in order to minimize stair-case and dispersion errors.

4.3 Results and discussion

4.3.1 Substrate binding to CYP2J2-nanodiscs

Detection of substrate binding to CYP2J2-ND on the nanoLCA sensor required immobilization of CYP2J2-ND with the active site of CYP2J2 available. Figure 4.1(a) shows a schematic of the immobilized CYP2J2-ND on the nanoLCA and Figure 4.1(b) shows a schematic of the binding of arachidonic acid to CY2J2's active site. Figure 4.1(c) shows a schematic of a single cup with a low concentration of CYP2J2-ND binding on the nanoLCA surface. The morphology of the nanoLCA device was confirmed by AFM as shown in Figure 4.1(d). Overall, the sensor top surface has uniform hole sizes with few defects After metal deposition, the nanohole diameter is 180nm and the periodicity of the holes (distance between two neighboring holes) is 350nm as measured from SEM images and AFM line scans as shown in Figure 4.2 (a) and (b).

The type of binding and dissociation constants of the substrates with CYP2J2-ND was determined by solution-based absorption spectroscopy titration assays. The binding titration data of TFN and DAN with CYP2J2-ND is shown in Figure 4.3(a) and 4.3(b), respectively. The absorbance difference spectra were measured at varying concentrations of the two drugs. The difference between the peaks and troughs of the absorbance difference spectra were then plotted for the increasing concentrations. The dissociation constant for the two drugs was then determined by fitting the plot to the Michaelis-Menten equation given as $A = \frac{A_{\max}[S]}{K_S+[S]}$, where A is the absorbance, A_{max} is the maximum absorbance, [S] is the concentration of the substrate, and K_s is the spin state constant. For P450s, the dissociation constant, $K_{D,}$ is approximated by K_S as determined by measuring the absorbance shift as substrates bind near the heme and change the spin state of the iron from low to high spin states in the case of type I binding. By titration assays, the dissociation constants of the substrates with CYP2J2-ND was found to be 20μM for AA, 18μM

for 2-AG, 12μM for ebastine, 10.8μM for MSPPOH, 5.6μM for TFN, and 1.44μM for DAN. The dissociation constants for AA, 2-AG, Ebastine, and MSPPOH with CYP2J2-ND matches well with previous results.[162] The dissociation constant of DOX with CYP2J2-ND remains unknown and cannot be determined by a conventional titration assay due to the spectral overlap.

4.3.2 Substrate response curves and CYP2J2 nanodisc surface coverage on nanoLCA sensor

Given these experimental values for the dissociations constants, we determined the response curve for the number of molecules on the sensor surface as a function of concentration of the substrate in solution, as shown in Figure 4.4. As can be seen, despite that the dissociation constants for the six measured substrates are the same order of magnitude; there is a detectable difference of the response of CYP2J2-ND at a wide range of substrate concentrations. The separation between two molecules (d) at a certain concentration was calculated as $d = 1.18C^{-\frac{1}{3}}$, where d is in nm and C is in M. At a concentration of ~μM, the distance between two CYP2J2-ND will be ~118 nm. Therefore, in 1 μM^2 area we can fit about 81 CYP2J2-ND (assuming a mass of 320kDa and a minimum diameter of 9nm for each CYP2J2-ND). The maximum coverage on our sensor is calculated to be Γ_{max} = 383pgcm^{-2}, which corresponds to monolayer of protein covering approximately 50% of the surface.

The binding and unbinding interactions between immobilized CYP2J2-ND and the target drug were modeled with the following equation:

$$d[CYP2J2-Drug]/dt = k_{on}[CYP2J2][Drug] - k_{off}[CYP2J2-Drug] \quad (4.1)$$

where k_{on} and k_{off} are the reaction coefficients for binding and release of drug molecules, respectively. In terms of surface coverage equation (4.1) can be written as:

$$\partial\Gamma(t)/\partial t = k_{on}\, C[\Gamma_{\max} - \Gamma(t)] - k_{off}\Gamma(t) \quad (4.2)$$

where $\Gamma_{\max}$ is the surface coverage when no more sites are available for analyte binding and C is the molecular concentration of the drug. Note that k_{on} and k_{off} have different units: $M^{-1}s^{-1}$ for k_{on} and s^{-1} for k_{off}.

Solving equation (4.2) with the boundary condition $\Gamma(0) = 0$ we obtain

$$\Gamma(t) = \frac{k_{on} C \Gamma_{\max}}{k_{on} C + k_{off}} \left[1 - \exp\left\{-\left(k_{on} C + k_{off}\right)t\right\}\right] \quad (4.3)$$

At equilibrium the rate of binding and release are equal. Hence, with the condition, $\Gamma(t \to \infty) = \Gamma_{eq}$ equation (4.3) can be written as:

$$\frac{\Gamma_{eq}}{\Gamma_{\max}} = \frac{C}{C + K_D}$$

where K_D is the dissociation constant ($K_D = k_{off}/k_{on}$) approximated as K_S for P450s.

4.3.3 FDTD simulation of substrate binding to cytochrome P450 in nanodiscs on the nanoLCA sensor

In order to predict the plasmonic peak shift of P450s on the nanoLCA sensor following substrate binding, FDTD was used to simulate three different conditions, i.e. P450 binding with (1) no substrate, (2) with type I substrate and (3) with type II substrate. The real part of refractive index was calculated from Kramers-Kronig relations for all three cases. The imaginary parts of these three cases, which corresponds to absorption coefficient, are based on measured data and shown in Figure 4.5(a). The measured absorbance spectra and the simulated transmission spectra of all three cases are shown in Figure 4.5 (b) and (c) respectively. It can be observed that the resonance peak at 465 and 605 nm of P450 with no drug binding performs blue shift to 462 and 598 nm with the binding of type I substrate. On the other hand, when a type II substrate was applied

to bind on the surface of the nanoLCA, these two resonance peaks were red shifted to 472 and 608 nm. These shifts agrees with previous results.[159] Figure 4.5 (d-f) shows the calculated electric field distribution in z-direction for P450, P450 with type-I drug, and P450 with type-II drug, respectively. The electric field for P450 without drug and with type-II drug are mostly dipolar in nature, whereas for type-I drug, the electric field is quadrupole in nature. Due to strong charge accumulation on top side of the nanohole rim (Fig. 4.5 (e)), the effective dipole moment of the system is increased for type-I drug case compared to without drug, and with type-II drug case. The increased dipole moment induces a higher restoring force for the plasmons, which leads to shift of plasmon resonance to higher energy (blue shift in the resonance wavelength).

4.3.4 CYP2J2-nanodisc immobilization and nanoLCA reliability

A representative red shift in the transmission peak for a single well corresponding to immersion of the nanoLCA sensor in MUA and the CYP2J2-ND/EDC solution is shown in Figure 4.6 (a). In order to assess the overall success of immobilization and the reliability of the nanoLCA sensor, the average and standard deviation of the plasmon resonance peak wavelength in air was determined for all 28 wells used in this study. The averages and standard deviations of the shifts after MUA and CYP2J2-ND/EDC immersion were also determined. The plasmon resonance wavelength in air was 536±3nm, as shown in Figure 4.6(b). The shift following MUA immobilization was 2±4nm and the shift from air following CYP2J2-ND binding was 5±2nm. The shift for the vehicle control, containing only the 10mM KPi buffer, never exceeded 1nm.

4.3.5 Spectral shifts of CYP2J2-ND after substrate binding

Table 4.1 gives a summary of the seven substrates tested for their solution-based and surface-based binding with CYP2J2-ND. From the solution-based absorbance data, it was determined that all seven substrates (AA, 2-AG, Ebastine, MSPPOH, TFN, DAN, and DOX) result

in a blue shift in the Soret band of CYP2J2-ND and therefore are classified as type I drugs for this cytochrome P450 protein. As expected for type I substrates, the spectral shift of immobilized CYP2J2-ND on the nanoLCA sensor following substrate binding was consistently to lower wavelengths (blue shift). Despite the fact that the dissociation constants of the seven substrates used here are similar, substrate-dependent shifts were measured in addition to concentration-dependent blue shifts. Figure 4.6 (c) shows a representative blue shift in the transmission spectrum plasmon resonance peak of CYP2J2-ND immobilized on the nanoLCA sensor following immersion in a solution containing a high concentration of Ebastine. For comparison, Figure 4.6 (d) and (e) show the shift after immersion in a low concentration of Ebastine, and the 10mM KPi buffer, respectively. The lower concentration of the substrate leads to a lower magnitude spectral blue shift on the nanoLCA an incubationnin the KPi buffer alone does not lead to a detectable shift. Figure 4.6 (f) gives a bar graph summary of the blue shifts corresponding to drug binding to CYP2J2-ND on the nanoLCA sensor for all seven substrates at high and low concentrations.

4.3.6 Colorimetric detection of substrate binding to CYP2J2-ND

The nanoLCA sensor has a single transmission peak in the visible range and therefore, brightfield microscope images can be used to qualitatively measure spectral shifts following drug binding. In order to carry out the image analysis, the original image of 2048x2048 pixels with 24 bit depth was first converted to an 8 bit image by separating the red, green, and blue channels in ImageJ software. Figure 4.7 (a) shows the intensity of the green channel for MUA, CYP2J2-ND, and Ebastine binding in sequence on the nanoLCA false colored in the intensity ranges of 0-255. The average intensity of the red, green, and blue color channels for MUA, CYP2J2-ND, and ebastine is shown in Figure 4.7 (b). All three color channels follow a similar pattern showing an overall intensity increase. Figure 4.7 (c) shows the intensity percentage, calculated as the average

intensity of each color channel divided by the sum of the average intensity for each color channel. It can be seen that from MUA to CYP there is a detectable increase in the red and green intensity percentages and a detectable decrease in the blue intensity percentage between the images. These changes in the intensity percentages of the red, green, and blue color channels match what would be predicted for a spectral red shift on the nanoLCA device, corresponding to the spectral data we collected for CYP binding to immobilized MUA. From CYP2J2 to Ebastine, there is a detectable decrease in the red intensity percentage and a detectable increase in the green intensity percentage. The changes in the color channel intensity percentages indicate that a blue shift is occurring on the nanoLCA device, confirming the spectral data we collected for Ebastine binding to CYP2J2. The potential use of the nanoLCA sensor for detecting drug binding to P450s by image analysis alone could drastically improve assay speed allowing high-throughput screening of hundreds of drugs binding to P450s simultaneously.

4.3.7 Discussion of detection of substrate binding to CYP2J2-ND on nanoLCA

Overall, these results suggest that the nanoLCA sensor allows spectral and colorimetric analysis of substrate binding to CYP2J2-ND that can be carried out using a brightfield microscope, camera, and portable spectrometer. The development of a platform for high-throughput screening of drug binding to P450s will require a device with a small footprint, low cost, sensitive detection, and that can allow parallel detection of hundreds of different drugs at different concentrations. Nanoplasmonic sensors are an excellent candidate since they can be easily miniaturized. In particular, nanohole sensors only require a light source and portable spectrometer for data acquisition. The spectral reliability of the nanoLCA sensor that we have reported here potentially allows quantitative detection of the binding of different substrates at different concentrations to P450s. A FDTD simulation study confirmed the spectral blueshift of type I binding on the

nanoLCA device. In addition, we have also presented the potential to use the nanoLCA device to perform colorimetric detection of substrate binding to CYP2J2-ND due to its distinct spectral properties.

4.4 Conclusion

Here we have reported the application of a nanoLCA sensor to the detection of substrate binding to CYP2J2-NDs. The nanoLCA fabrication method relies on wafer-scale nanoreplica molding, which results in low defect highly uniform sensors. We found the spectral properties of the nanoLCA sensor to be highly reliable, which allowed the detection of substrate dependent and concentration dependent blue shifts, corresponding to the binding of type I substrates to CYP2J2-NDs. Our results were confirmed by traditional solution-based absorption spectroscopy and a FDTD simulation study. We also demonstrated the ability to use brightfield microscope images alone to extract spectral information, based on the fact that the nanoLCA spectrum consists of a single transmission peak in the visible. This study indicates that the nanoLCA sensor has a strong potential for the future development of a high-throughput spectroscopic on-chip method for detecting drug binding to cytochrome P450 proteins.

4.5 Figures and tables

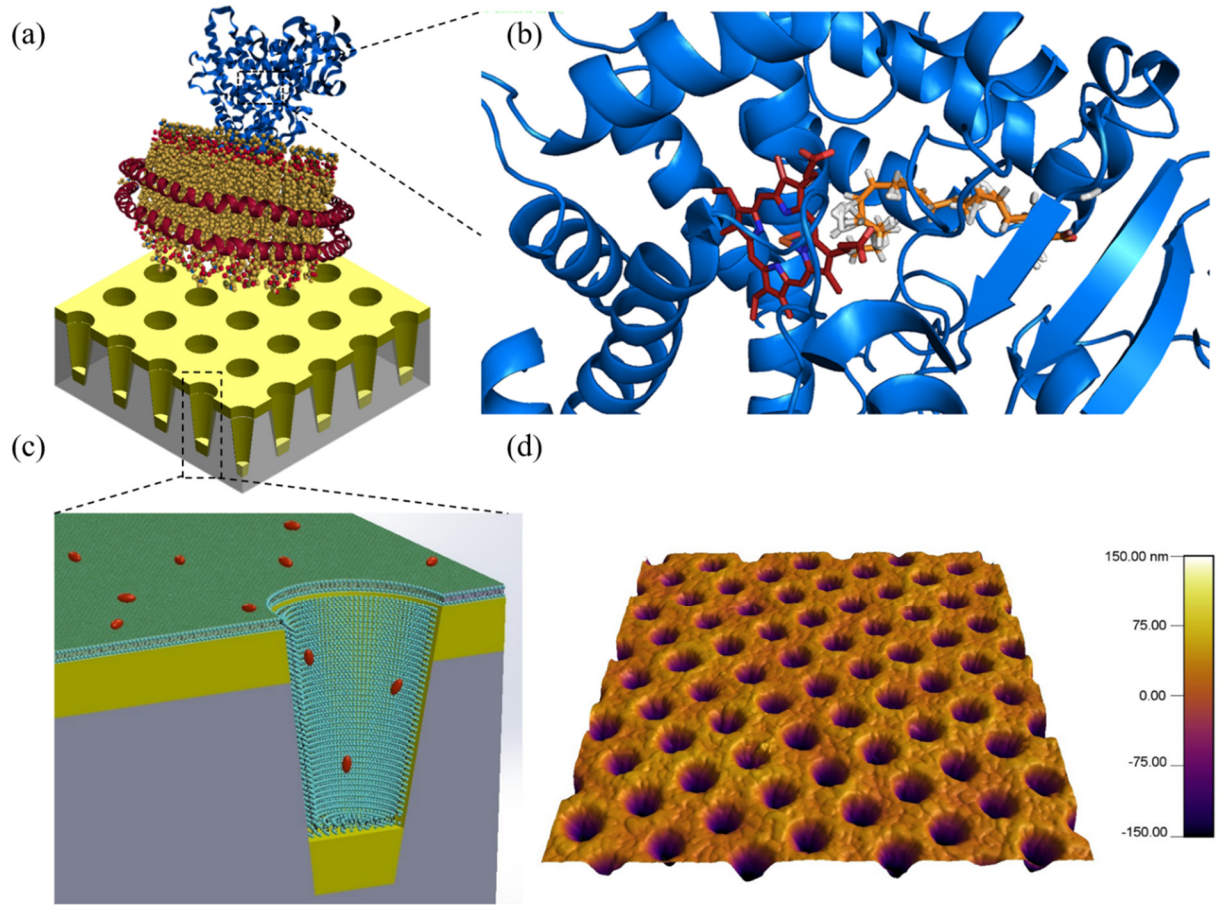

Figure 4.1 A schematic of the CYP2J2-ND system (a) with CYP2J2 protein (blue) incorporated into the Nanodisc, which consists of a phospholipid bilayer (gold) and two membrane scaffold proteins (red) is also shown along with a schematic showing binding of arachidonic acid to CYP2J2's active site (b). A schematic of the cross section of a single nanocup with MUA monolayer (light blue) and CYP2J2-ND (red) bound is also shown (c). The morphology of the nanoLCA device was confirmed by AFM imaging as shown in (d).

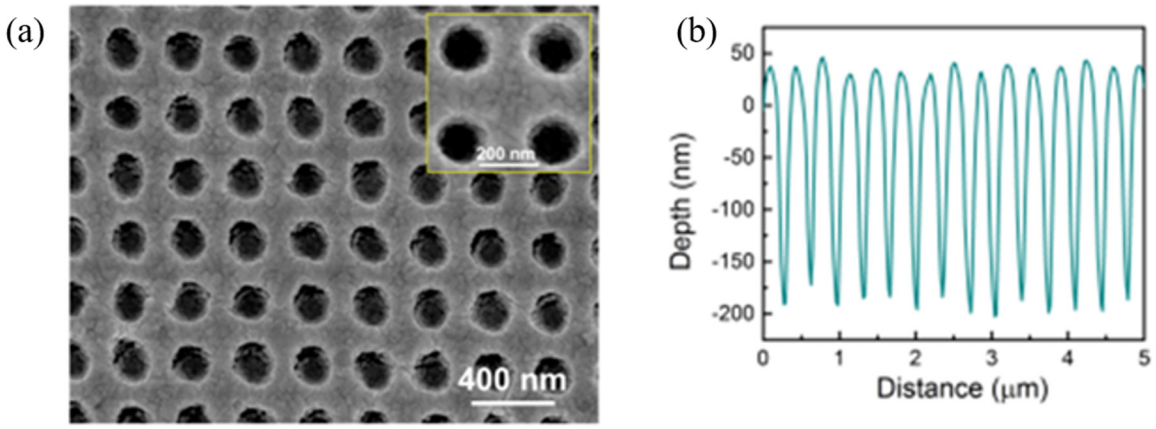

Figure 4.2 A top view SEM image (a) of the nanoLCA device is shown along with representative AFM line scan data (b). After metal deposition, the nanoLCA device was characterized by SEM and AFM in order to determine the uniformity, nanohole diameter, and nanohole periodicity. A representative top view SEM image is shown in (Fig. 4.2 (a)) and representative AFM line scan data is shown in (Fig 4.2 (b)). The nanohole diameter was determined to be 180nm and the periodicity was 350nm.

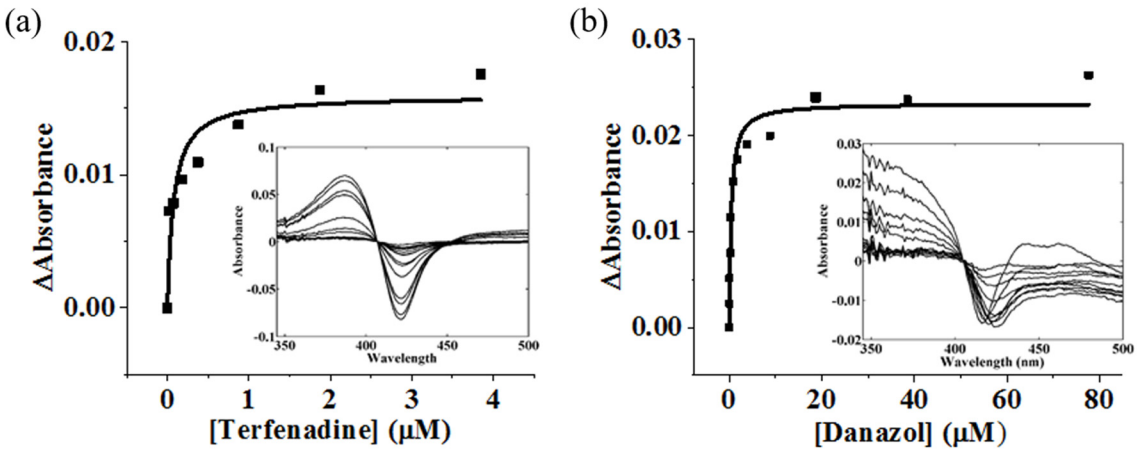

Figure 4.3 Binding titration data for TFN (a) and DAN (b) is shown. Each plot is the difference of the peaks and troughs of the difference spectra (inserts) at each corresponding concentration of substrate. The K_D of each substrate was determined by fitting the plots to the Michaelis-Menten equation.

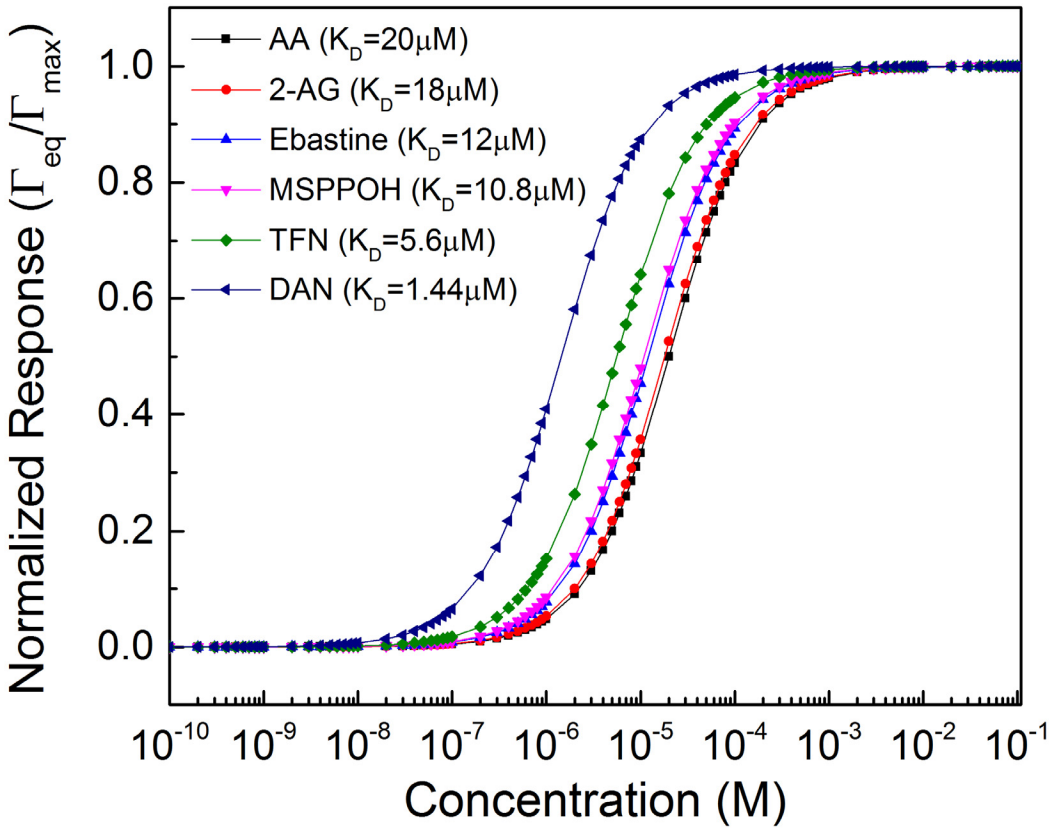

Figure 4.4 The response curve for number of molecules on the nanoLCA surface as a function of concentration is shown for the six different substrates with measureable dissociation constants used in this study. The curve is normalized to the maximum number of bound molecules possible.

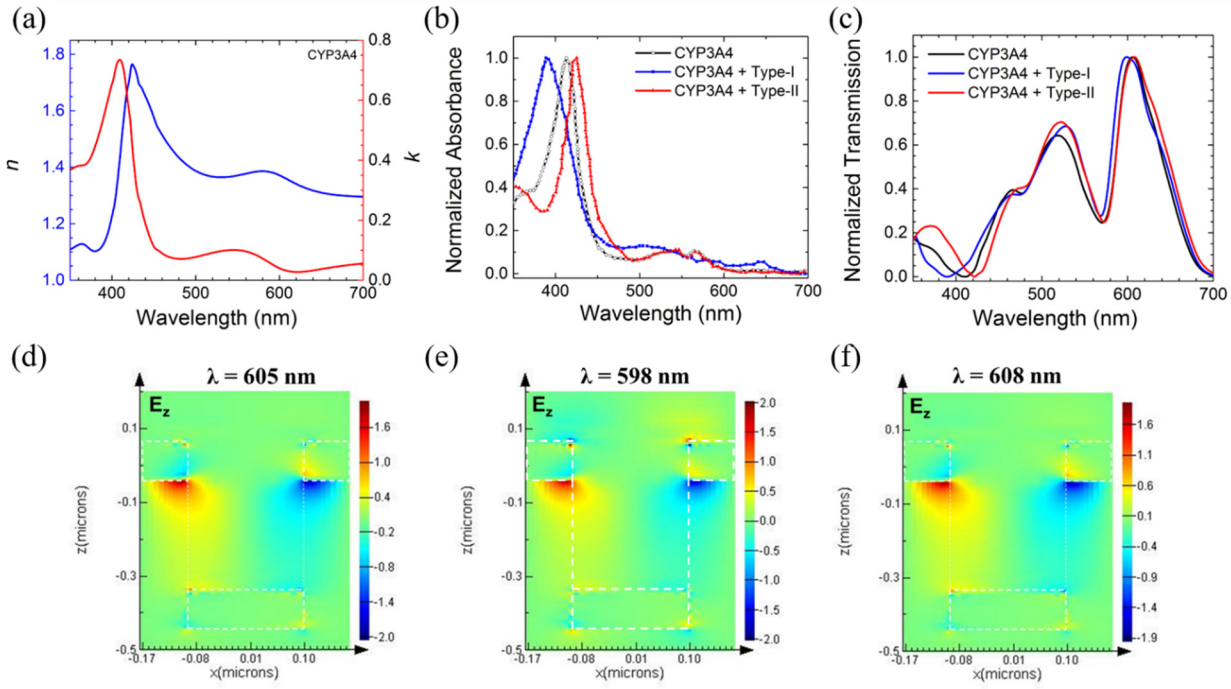

Figure 4.5 FDTD simulation of P-450 and drug system (Type-I and Type-II) on top of the nanoLCA. (a) Real (n) and imaginary (k) part of the refractive index of CYP3A4 used for the electromagnetic (FDTD) simulation. (b) Normalized absorbance spectra of CYP3A4 obtained experimentally, before and after drug binding. The black spectrum is for CYP3A4 without any drug, the blue spectrum is for CYP3A4 with Type-I drug showing blue shift of peak resonance wavelength position, and the red spectrum is for CYP3A4 with Type-II drug showing red shift of peak resonance wavelength position. (c) Transmission spectra obtained from FDTD simulation showing CYP3A4 before (black), and after drug binding (blue curve is for Type-I drug and red curve is for Type-II drug). (d-f) Calculated electric field in z-direction for CYP3A4 (d), for CYP3A4 with Type-I drug (e), and for CYP3A4 with Type-II drug (f).

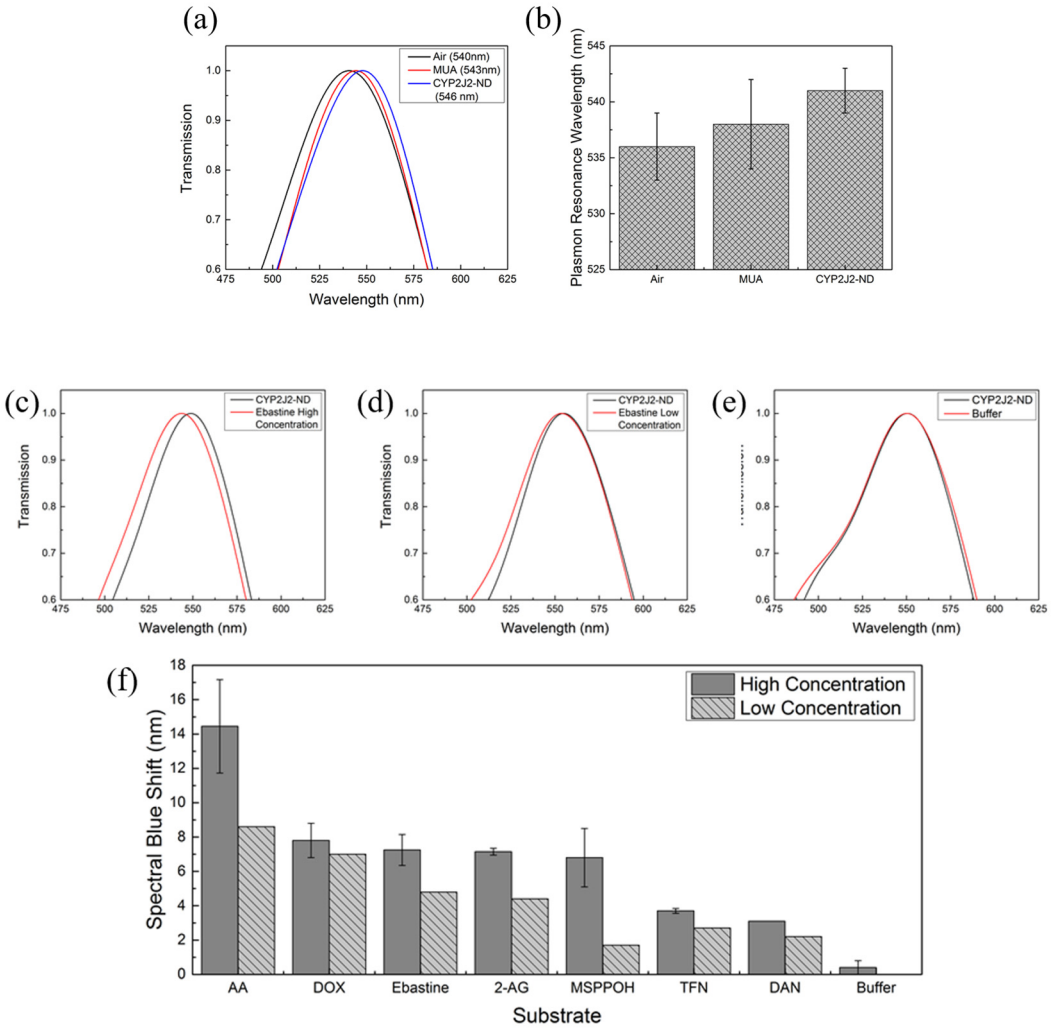

Figure 4.6 A representative red shift in the transmission spectra following MUA immobilization and CYP2J2-ND binding is shown in (a), with the peak wavelength at each step noted in the Figure legend, and the average plasmon resonance peak wavelength across all wells is shown in (b). The spectral blue shift from a high (c) and low (d) concentration of Ebastine binding with immobilized CYP2J2-ND along with the shift corresponding to 10mM KPi buffer alone (e) is shown. The lower panel shows a bar graph of the shifts on the nanoLCA corresponding to seven different type I substrates at high and low concentrations (f). The high concentration bar corresponds to the average of the two wells with an error bar denoting the standard deviation.

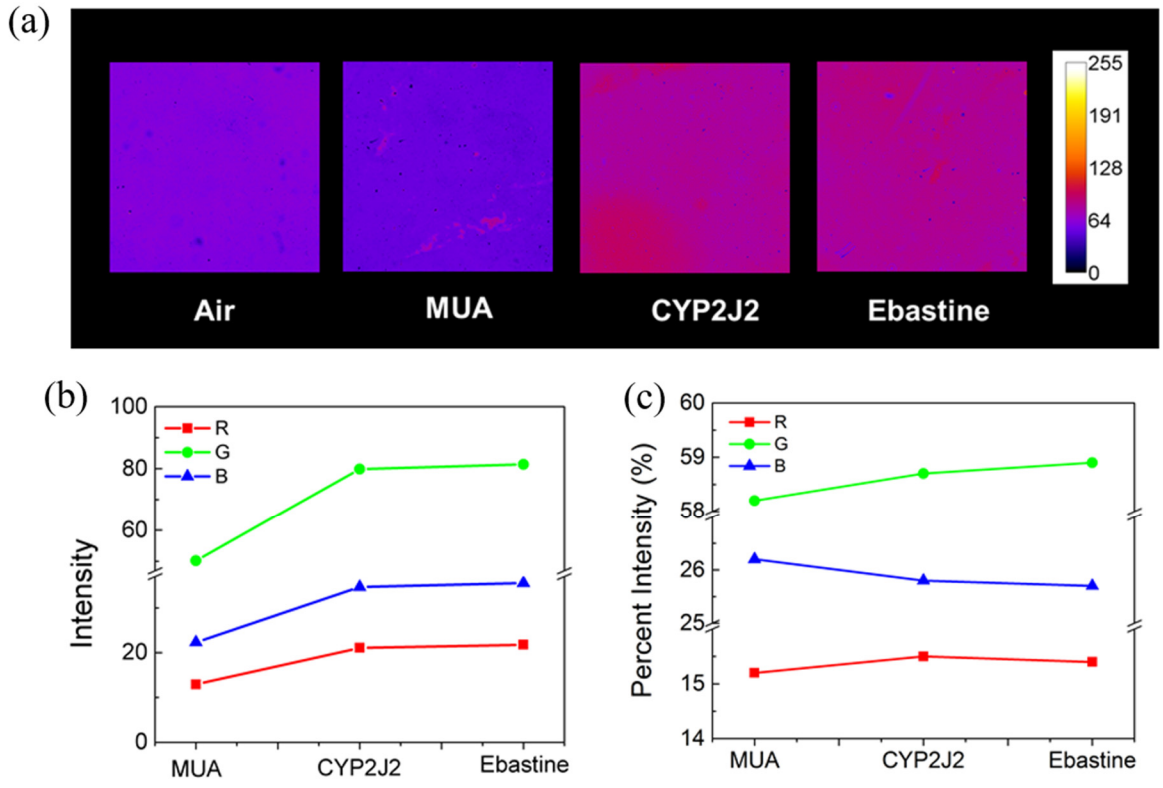

Figure 4.7 Images of the green channel intensity for Air, MUA, CYP2J2-ND, and Ebastine are shown (a). The changes in average intensity for the three color channels for MUA, CYP2J2-ND, and Ebastine is plotted in (b) and the percent intensity, calculated as the average intensity of the color channel divided by the total average intensity for the image, is also plotted in (c).

Table 4.1 Substrate Binding to CYP2J2-ND in Solution and on NanoLCA Sensor.

Drug	*Binding type*	*Dissociation constant (μM)*	*Direction of plasmonic shift*	*Plasmonic shift (High conc.)*	*Plasmonic shift (Low conc.)*
AA	Type I	20	Blue	14.5±5	8.6
2-AG	Type I	18	Blue	7.2±0.2	4.4
Ebastine	Type I	12	Blue	7.3±0.9	4.8
MSPPOH	Type I	10.8	Blue	6.8±1.7	1.7
TFN	Type I	5.6	Blue	3.7±0.1	2.7
DAN	Type I	1.44	Blue	3.1	2.2
DOX	Type I	Unknown	Blue	7.8±1	7

CHAPTER 5

3D PLASMONIC NANO-CAVITY STRUCTURES ON PERIODIC NANOCUP ARRAYS

In this chapter, we report a new sensor design and sensing method based on plasmonic-photonic interactions that occur when a nanocavity array is embedded in a 3D tapered nanocup plasmonic substrate. This device enables highly sensitive detection of refractive index changes based on changes to the transmission peak intensity without shift in the resonance wavelength. Unlike conventional plasmonic sensors, there is a consistent and selective change in the transmission intensity at the resonance peak wavelength with no spectral shift. In addition, there are wavelength ranges that show no intensity change, which can be used as reference regions. We describe the fabrication and characterization of the plasmonic nanocavity sensor and also demonstrate advanced biosensing. Simulations and a theoretical analysis are carried out to better understand the plasmon-photonic coupling mechanism. The sensor device is fabricated by thin film semiconductor material such as cadmium sulfide (CdS) layer, which has high refractive index (n~2.53) and very low extinction coefficient, sandwiched between two Au layers. The Au-CdS-Au nanocup array structure allows sensing based on the transmission intensity change with the help of simple bandpass filter to allow certain wavelength to be transmitted in a visible region at normal incidence illumination. Due to the high refractive index of the sandwiched layer, CdS thin film which acts as a resonant cavity, electric field is confined at the interface of Au and CdS layer at lower surrounding refractive index. An increase in the surrounding refractive index causes a decrease in the electric field intensity at the interface but an increase in out-coupling of electric field on the topmost Au layer, hence, enhancement in overall transmission intensity is observed.

5.1 Introduction

As discussed earlier, surface plasmon is a collective oscillation of surface-bound free electrons at the interface of a dielectric and a metal layer and the free electrons are oscillating at certain wavelength which is referred as plasmon resonance wavelength.[164] This plasmon resonance wavelength is very sensitive to nearby di-electric changes that's why this property can be used to detect different events on the surface of the device due to their tight binding at the interface.[165] Another optical property of the surface plasmon is the localized electric field induces near the surface of metal with the strong absorption of light. This optical property can also effect the optical properties of the nearby molecules which can also be used for sensing.

There are different types of plasmonic waveguides are analyzed for high sensitive detection. One example of such devices is stripe waveguides, based on a single thin metallic film to provide comparatively high propagation length which decrease the modal loses, however, there is very low field confinement.[166, 167] In order to overcome these problems, hybrid plasmonic waveguides have been studied that combine thin metal film with semiconductor and dielectric layers with higher refractive index to improve the gain medium and to decrease the modal losses.[168-172] A device structure, where a dielectric layer with higher refractive index is sandwiched between two metal layers with lower refractive index, is very promising as it can provide higher field confinement within the core layer.[173, 174] There are many promising characteristics of these type of plasmonic waveguide devices, such as metal layers can also be used as electrodes for electrical pumping of the active core material, which enable simplified integration.[175, 176]

Alternatively, plasmonic sensors based on LSPR [177, 178] and extraordinary optical transmission EOT [179] are of considerable theoretical and experimental interest. In EOT devices,

the transmission of incident light through a nanohole array in an optically thick metal sheet is orders of magnitude greater than that predicted by classical aperture theory.[166] The optical transmission of EOT devices has a strong dependence on the excitation of plasmonic resonances.[164] This includes LSPR resonances at the rims of the nanoholes that depend strongly on the nanohole shape and size along with surface plasmon polariton (SPP) resonances excited by diffraction and scattering, which have a strong dependence on the nanohole periodicity. EOT sensors are currently under rapid development for point-of-care biosensing since excitation can be done with an incoherent light source and detection can be done with a portable spectrometer.[180, 181] However, the sensitivity is an order of magnitude lower than SPR sensing in the Kretschmann configuration. In addition, the fabrication of large-area sensors with repeatable spectral properties remains an ongoing challenge.

The EOT sensor that we utilize here is the nano Lycurgus cup array (nanoLCA) device, which unlike conventional EOT devices consists of a 3D tapered nanocup structure that is plasmonically active due to a gold (Au) layer on the top and bottom of the cups in addition to Au nanoparticles lining the cup sidewalls.[64] On top of the nanoLCA we then deposit a thin film of CdS, which has a high refractive index (RI) and low extinction coefficient, followed by a second Au layer in order to form a nanocavity in combination with the plasmonic structure. The spectral features and near field of the nanoLCA device alone have already been studied in detail by experiment and 3D-FDTD simulation in our previous work.[182-184] The nanoLCA spectrum in the visible range consists of two main peaks: the first, which occurs at a lower wavelength, corresponds to a LSPR resonance at the rims of the nanocups. The second, which occurs at a longer wavelength, corresponds to the excitation of the SPP-Bloch waves (SPP-BW) at the Au-superstrate

and Au-substrate interfaces. In the case of air, the two peaks couple to form a single peak in the visible range while for higher refractive indices of the superstrate there are two distinct peaks.

In our multilayer nanoLCA (ML-nanoLCA) device a transmission peak occurs in the visible or NIR (depending on the thickness of CdS) due to the excitation of SPP-BW at the Au-CdS interface, while the nanocavity confines the optical energy between the Au layers. When there is a change in the refractive index of the surrounding medium, there is an increased in the measured transmission intensity of the peak resonance wavelength, representing out coupling from the mode confined between the Au layers to the superstrate. However, no change in RI is occurring at the Au-CdS interface and therefore there is no shift in the peak. Detection can be done by simply monitoring the change in transmitted intensity at the resonance wavelength. In addition, our sensor contains a reference point where no intensity change occurs with increasing RI. Therefore, the sensor is self-referencing and the changing intensity value of the resonance peak can be read directly without any corrections. Other groups have reported intensity based detection of molecular binding events using EOT devices where binding events typically result in a decrease in transmission intensity (increase in absorbance).[69, 185] However, complex experimental setups and substantial post-processing of the data are required to obtain consistent results since these spectral features also contain shifts and no reference points.

In this chapter, we describe the fabrication, optical characterization, and principle of operation of the ML-nanoLCA device. In our hybrid nanocavity plasmon resonance sensor, a resonance occurs with a significant intensity change, but no spectral shift, with increasing RI. This phenomenon, which is being reported here for the first time, allows for a new type of plasmonic sensor where illumination and detection can occur using only a LED or broadband light source with a bandpass filter and photodetector. In this case, the illumination wavelength can be chosen

to optimally couple with the plasmon resonance wavelength. The two wavelengths will remain coupled through the detection since there is no shift and an optimum sensitivity can be maintained. This type of sensor is ideal for low concentration label-free biosensing where increasing accessibility is crucial. The device is robust in that the results are independent of angle and polarization of the incident light. In addition, no high end spectrometer or other specialized equipment is required.

5.2 Materials and methods

5.2.1 ML-nanoLCA device fabrication

The device fabrication of ML-nanoLCA is started with the fabrication of nanoLCA device and then multilayers of cadmium sulfide (CdS) and gold (Au) are deposited on top of it. As we have discussed earlier, the master mold consisting of the tapered nanopillar pattern, made with laser interference lithography, is first cleaned and silanized followed by evenly spreading UV-curable polymer (UVcP) (NOA-61, Sigma Aldrich) on the top of it. A PET sheet is then carefully put on top of the polymer to avoid bubble formation and to act as a substrate, and exposed to UV-light (105 mW cm^{-2}). The PET substrate with nanohole arrays was peeled off carefully from the master mold and then first layer of Au is deposited to make the surface of the device active. In case of ML-nanoLCA, we have deposited a semiconductor layer of CdS and followed by another Au layer to make a cavity like structure.

5.2.2 Material depositions

Titanium (Ti), as an adhesion layer, with top and bottom Au layers is deposited using Temescal six pocket electron beam evaporation system at the rate of 0.3 Å/s and 0.5 Å/s to deposit uniform and smooth layers. Whereas, sandwiched layers, CdS and SiO_2 are deposited using sputter

deposition using RF plasma. The power of the RF plasma is carefully ramp up and down such as 10-20 watts per minute, as fast ramping of the RF power will cause the target to be broken. We have used 100W and 250W of RF plasma power to deposit CdS and SiO_2 respectively, at the rate of 0.3 Å/s.

5.2.3 Spectral and sensitivity measurements

The transmission spectra through ML-nanoLCA are measured by using Cary 5G UV-Vis spectroscopy with single increment in the wavelength range from 400nm to 800nm. The setup is used as zero baseline correction in which the output spectrum is normalized with light source of the system. The device sensitivity is measured as the relative change in the transmission (T) intensity at specific wavelength which corresponds to the maximum intensity in the unit of Δ%T/RIU. Sucrose (Sigma-Aldrich) solution with different concentrations 0% to 60% mixed in milli-Q water, which corresponds to RI variation from 1.33 to 1.45. Different concentrations of sucrose solutions are added on the top of the ML-nanoLCA device and measured the respective output transmission intensity by using Cary-5G spectrophotometer.

5.2.4 3D-FDTD simulation for ML-nanoLCA

The 3D-FDTD simulation was performed using a commercial software package (Lumerical Solutions, Inc.). Periodic boundary conditions were imposed in x- and y-boundaries with a single nanocup modeled at the center of the FDTD region. The periodicity of the nanocup array was 320 nm. The cup was embedded in a dielectric material with the RI of 1.56, which is the RI of the NOA-61. The radius and the depth of the nanocup are 100 nm and 500 nm, respectively. The angle of the sidewall of the cup is 85 degrees with respect to the x-axis A continuous 9 nm Ti layer was then positioned along the surface of the dielectric followed by 90 nm Au, 40 nm CdS or SiO_2 and 90 nm Au layers. Each of the material properties (RI and k) were taken from the

Handbook of Optical Constants of Solids.[186] A 2 nm mesh was used, a plane wave was placed below the ML-nanoLCA structure with the propagation direction of +z, and a 1D monitor above the ML-nanoLCA structure was used for a transmission spectral calculation. 2D monitors in xz- and yz-planes were placed to obtain the electric field distributions. Perfectly matched layers were applied along the z-axis boundaries to avoid reflection and interference by the presence of the boundary.

5.2.5 Ellipsometry measurements

Initially the thickness of deposited materials, from e-beam evaporation and sputter system, is optimized by the crystal monitor installed in the equipments. Then the thickness is verified using Ellipsometry (Gartner Scientific Corporation), which is the optical method to measure thickness of the thin film with known optical properties (refractive index 'n' and extinction coefficient 'k') at single wavelength of 632.8nm. The ellipsometry measurement are consistent with the crystal monitor readings.

5.3 Results and discussion

In this work a new design of a nanohole structure is introduced by adding a multilayer structure on top of the nanoLCA device. The process is started with the fabrication of nanoLCA device which is discussed earlier (Figure 5.1 (a)). Figure 5.1 (b) shows a schematic of the ML-nanoLCA device which consists of a 40 nm layer of CdS sandwiched between two Au layers (bottom layer 90 nm and top layer 50 nm) on a substrate made from UV-curable polymer on a PET sheet. The surface morphology of the device, obtained by an AFM scan, is shown in Figure 5.2 (a) with a graph that shows the depth of the periodic hole structure on the device. Figure 5.2 (b) shows the SEM image of the top view of the device and the inset shows a cross-sectional view, which is

taken by a focused ion beam (FIB) technique. All three stacked layers of the ML-nanoLCA device are clearly distinguishable in the cross-sectional view.

The spectra in air (n=1), water (n=1.33), and isopropyl alcohol IPA (n=1.37) are shown for the nanoLCA sensor in Figure 5.3 (a). In air the nanoLCA device has a single peak in the visible range corresponding to coupling between the LSPR resonance and the SPP-BW resonance of the tapered nanocup array. In water and IPA these two resonances become distinguishable peaks. Characteristic of EOT sensors, when the RI (RI) of the superstrate increases, a red shift in the resonance wavelength λ_{peak} is observed. However, as shown in Figure 5.3 (b), once the multilayered structure is introduced on the nanoLCA, an increase in RI causes an increase in intensity, but no shift for the prominent peak around 700 nm. This resonance at 700 nm corresponds to the red shifted SPP-BW on the nanoLCA due to the deposited materials.

In order to assess the sensitivity of the ML-nanoLCA structure, we added different concentrations of sucrose solutions (from 0% to 60% mixed in Milli-Q water) on the superstrate. This change in concentration of the sucrose corresponds to a bulk RI change of 1.33 to 1.44. As expected, with increasing RI there is an increase in the intensity of the resonance peak in the transmission spectrum as shown in Figure 5.4 (a). In order to compare the material properties of the device, the layer of CdS was replaced by a 40 nm dielectric layer of silicon dioxide (SiO_2). For this modified multilayer structure, the transmission intensity also consistently increased with an increase in the RI of the superstrate as shown in Figure 5.4 (b). To verify this experimental finding, a 3D-FDTD study was carried out and the entire spectrum was simulated for both structures with increasing values of the RI of the superstrate as shown in Figures 5.4 (c) and (d). As can be seen, the simulation results agree very well with the experimental spectra. Although the SiO_2 layer shows

a similar variation in the transmission intensity to the CdS layer, the increase in the transmission intensity is relatively small when compared to the CdS device.

The sensitivity of the devices is calculated by the relative change in the transmission (*T*) intensity at the resonance wavelength, which corresponds to the maximum intensity, per RI unit (RIU) such that the final unit for sensitivity is Δ%T/RIU. The calculated sensitivity of the ML-nanoLCA device with CdS is 660 Δ%T/RIU (4000 Δ%T/RIU with respect to air at λ = 695nm) while the calculated sensitivity for the device with SiO_2 is 340 Δ%T/RIU (2000 Δ%T/RIU with respect to air at λ = 672nm). Therefore, by using CdS instead of SiO_2 the sensitivity is approximately doubled as shown in Figure 5.5 (c).

In order to better understand the operating principle for the ML-nanoLCA device the electric field (E-field) distribution was solved for by a 3D-FDTD simulation study with light propagation in the z-direction and polarization in the x-direction. First, we have performed 3d-FDTD simulation on simplified array of nanohole structure to observe the change in E-field on Au-CdS-Au layers. Figure 5.6 shows, the intensity of the E-field is increasing by changing the refractive index of the surrounding medium from 1.0 to 1.45, which is indicated by red arrow. In order to further investigate the operating principal, we have performed 3D-FDTD simulation on multilayer nanocavity structure. Figure 5.7 shows the E-field distribution on the cross-section of the nanocavity at the transmission peak for increasing RI values. Due to the higher RI of the sandwiched material compared to the superstrate, the E-field is confined at the interface of the Au and CdS layer as indicated by the red arrow. Furthermore, the multilayered structure serves as a resonant cavity with the two Au layers acting as mirrors to reflect the incident light back and forth contributing to the confined mode in the CdS layer. The oppositely-moving waves form standing waves in the cavity and the cavity stores electromagnetic energy which provides coupling to the

incident light.[187, 188] As the RI of the superstrate is increased, the intensity of the E-field is decreased at the interface between the CdS and the bottom Au layer but is increased in the top Au layer (indicated by white arrow) which enables the out-coupling of the E-field to the top Au layer; hence, the overall transmission intensity is enhanced.

The 3D-FDTD simulation study is also used to examine the material properties that give rise to higher sensitivity. Further investigation of materials for the sandwiched layer having different optical constants i.e. index of refraction (n) and the extinction constant (k), is executed. All of the geometrical parameters of the ML-nanoLCA device structure are kept same for an accurate comparison. The study suggests that any materials which has a high RI and low extinction coefficient (nearly zero) in the wavelength range of 600 nm to 800 nm will exhibit the similar increase in the transmission intensity with the increase of superstrate RI (simulated spectra are shown in the SI). This also explains our experimental results where a CdS thin film as the sandwiched layer (n=2.529 and k~0) results in higher overall intensity increment compared to SiO2 (n=1.45 and k=0).

The ML-nanoLCA device is further analyzed for better sensitivity to detect surface binding events at lower concentration. For plasmonic application, in terms of metal selection, silver (Ag) has lowest loss in the visible and near-IR region and has higher device sensitivity, however, Ag is unstable as it can be easily oxidized and degraded in terms of device fabrication.[189, 190] Gold (Au) is the next best material in terms of loss in the visible and near-IR region and it is more chemically stable and continues uniform film that can be formed even with smaller thickness (e.g 1.5-7nm). However, the device sensitivity is lower as compared to Ag plasmonic device.[191, 192] ML-nanoLCA device as hybridized structure which consists of Ag as a bottom layer followed by thin layer of CdS and Au is deposited on the surface of the device ca also be studied for higher

sensitivity. With this structure, Ag will be more stable as it will be covered by other materials and sensitivity of the device is expected to increase. Moreover, as in the current structure where top and bottom layers are of Au material, the desired area for sensing is in visible to near-IR (600nm to 800nm) as Au-nanoLCA has a resonant wavelength ~530nm compare to Ag-nanoLCA which has resonant wavelength ~450nm. Therefore, by replacing the bottom layer of ML-nanoLCA with Ag, it is expected that the resonance wavelength of the new ML-nanoLCA device will be shifted in the visible region.

Thickness of the metal layers and core layer (dielectric/semiconductor) in ML-nanoLCA structure is another parameter to play with, to improve the plasmonic coupling efficiency and overall transmission intensity. The details of the modified thicknesses will be discussed in next chapter where we will demonstrate the detection of cancer biomarker CEA binding to its antibody immobilized on the device surface with high sensitivity and at lower concentration. The thickness of the metal layers, for the current structure, is 90nm and 50nm on bottom and top gold layers respectively with 40nm CdS sandwiched layer. Most of the light is blocked with these metal layers which cause lower in the overall intensity of the transmitted signal. If the thickness of the layers will be reduced, significant increase in the intensity of the transmitted light is expected. However, decrease in the thickness will affect the coupling efficiency as the E-field will be confined closer to the metal surface instead of the sandwiched layer as shown in Figure 5.8.[193] Therefore, thickness of the layers in ML-nanoLCA will be optimized using FDTD simulation to achieve the highest sensitivity of the device.

5.4 Conclusion

This work has presented a new method for plasmonic RI sensing with significant improvements over current SPR systems. Unlike conventional SPR sensors, the ML-nanoLCA achieves RI sensing through the transmission peak intensity variation with no resonance peak shift; thus, a spectrometer that has high spectral resolution is not required. Due to the spectral features of this plasmonic nanocavity device, we anticipate that excitation and detection can be carried out using an LED and photodiode, respectively. However, further analysis on acceptable noise levels and signal integrity will need to be carried out to see if the same sensitivity and LOD can be maintained. In this chapter, we have demonstrated a new design, fabrication and characterization of label-free biosensor using 3D plasmonic nano cavity structure known as ML-nanoLCA device. In ML-nanoLCA device, we have combined optical resonance cavity with the plasmon resonance all together to improve the sensitivity with simplified detection mechanism to detect surface binding events on top of the device. In general, this nanocup array substrate achieves refractive index sensing through a transmission peak shift with the extraordinary transmission phenomena. The ML-nanoLCA device is fabricated by thin film semiconductor material such as cadmium sulfide (CdS) layer, which has high refractive index (n~2.53) and very low extinction coefficient, sandwiched between two Au layers. The Au-CdS-Au nanocup array structure (ML-nanoLCA) allows sensing based on the transmission intensity change with the help of simple bandpass filter to allow certain wavelength to be transmitted in a visible region at normal incidence illumination. The sensitivity of the ML-nanoLCA structure, is measured by adding different concentrations of sucrose solutions (from 0% to 60% mixed in Milli-Q water) on top of the device which cause a change in bulk refractive index from 1.33 to 1.44. The calculated sensitivity of the ML-nanoLCA device with CdS is 660 Δ%T/RIU (4000 Δ%T/RIU with respect to air at λ = 695nm) while the

calculated sensitivity for the device with SiO2 is 340 Δ%T/RIU (2000 Δ%T/RIU with respect to air at λ = 672nm). These results further verified with 3D-FDTD simulation.

5.5 Figures

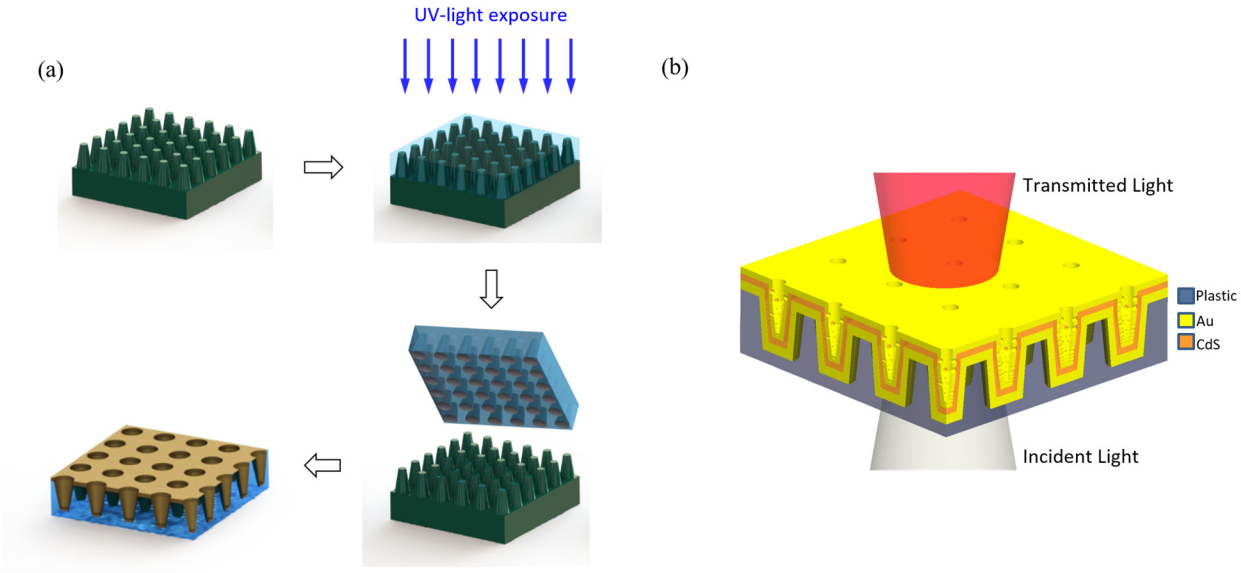

Figure 5.1 Schematic illustration of ML-nanoLCA device. (a) Schematics showing the fabrication process of nanoLCA device as discussed earlier in chapter 2 and 4. (b) Schematic showing the ML-nanoLCA device; the semiconductor layer consist of Cadmium Sulfide (CdS) is sandwiched between two gold (Au) layers on the Polyethylene terephthalate (PET) sheet and each layer is shown by different color marker. The schematic also shows that when the incident light is passed through the ML-nanoLCA device, the intensity of the transmitted light is increased and in red wavelength range with the presence of different refractive index material on the superstrate.

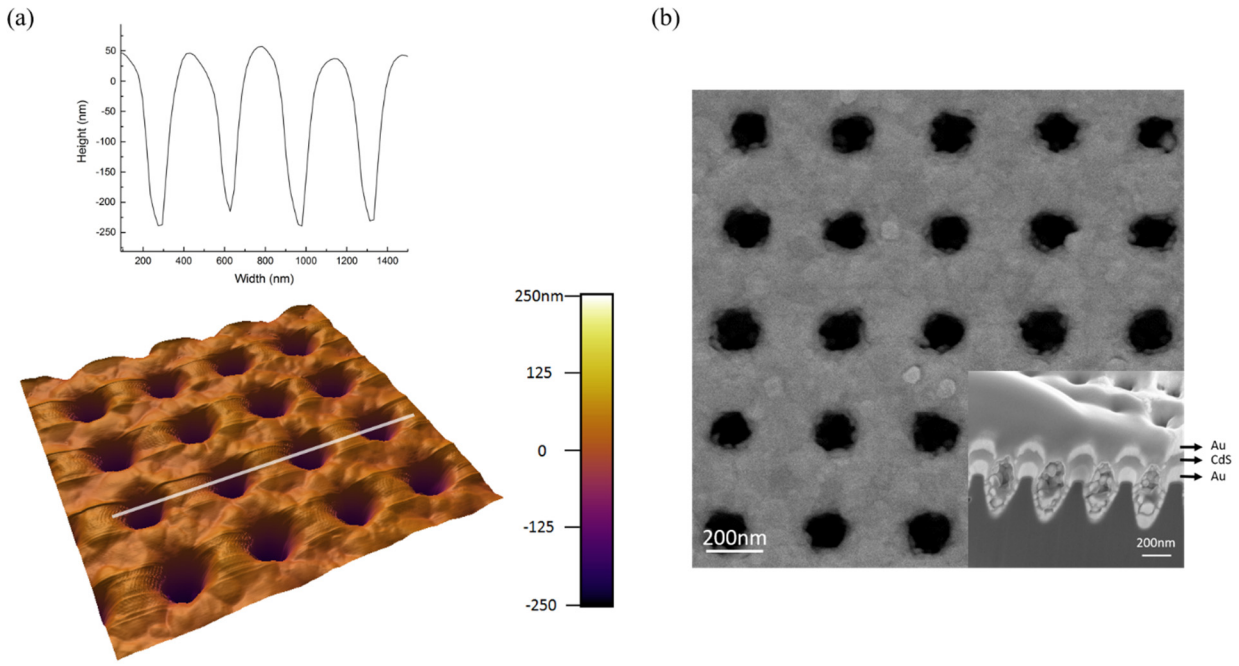

Figure 5.2 (a) Shows the AFM scan of the ML-nanoLCA device to show the surface morphology. The graph on the top and color scale bar shows the depth of the periodic hole structure on the device. (b) Shows the SEM image of the top view of the device and inset shows cross-sectional view using focused ion beam (FIB) image, where all three stacked layers are clearly visible of ML-nanoLCA device.

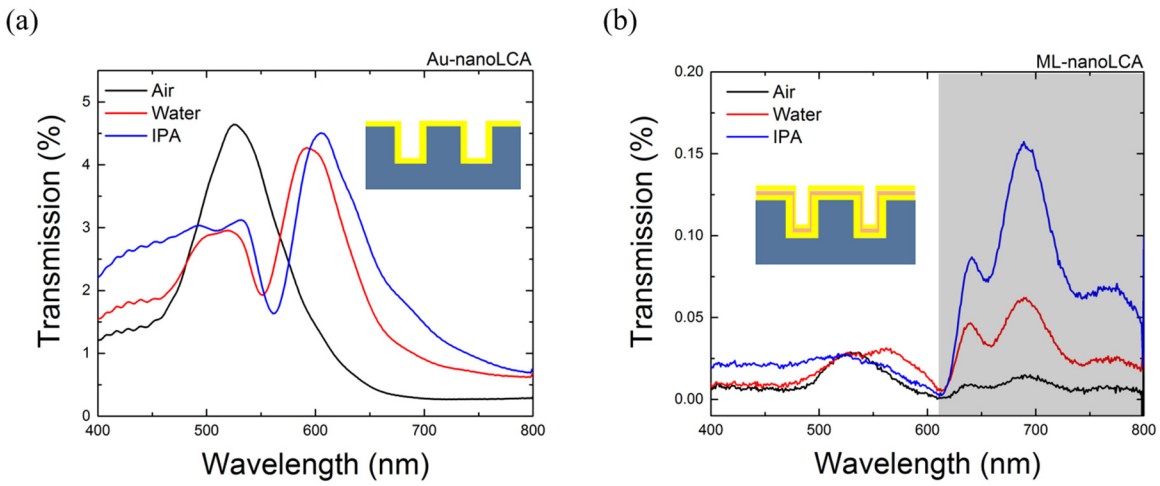

Figure 5.3 The comparison of transmission spectra for normal Au-nanoLCA device (a) and ML-nanoLCA device (b) with three different refractive index materials on the superstrate such as air (n=1), water(n=1.33) and Isopropyl alcohol (IPA, n=1.37). It is observed that with Au-nanoLCA device the peak wavelength position shifts in the transmission spectrum with respect to different refractive indices, however, in-case of ML-nanoLCA device, there is only intensity change with no peak wavelength shift.

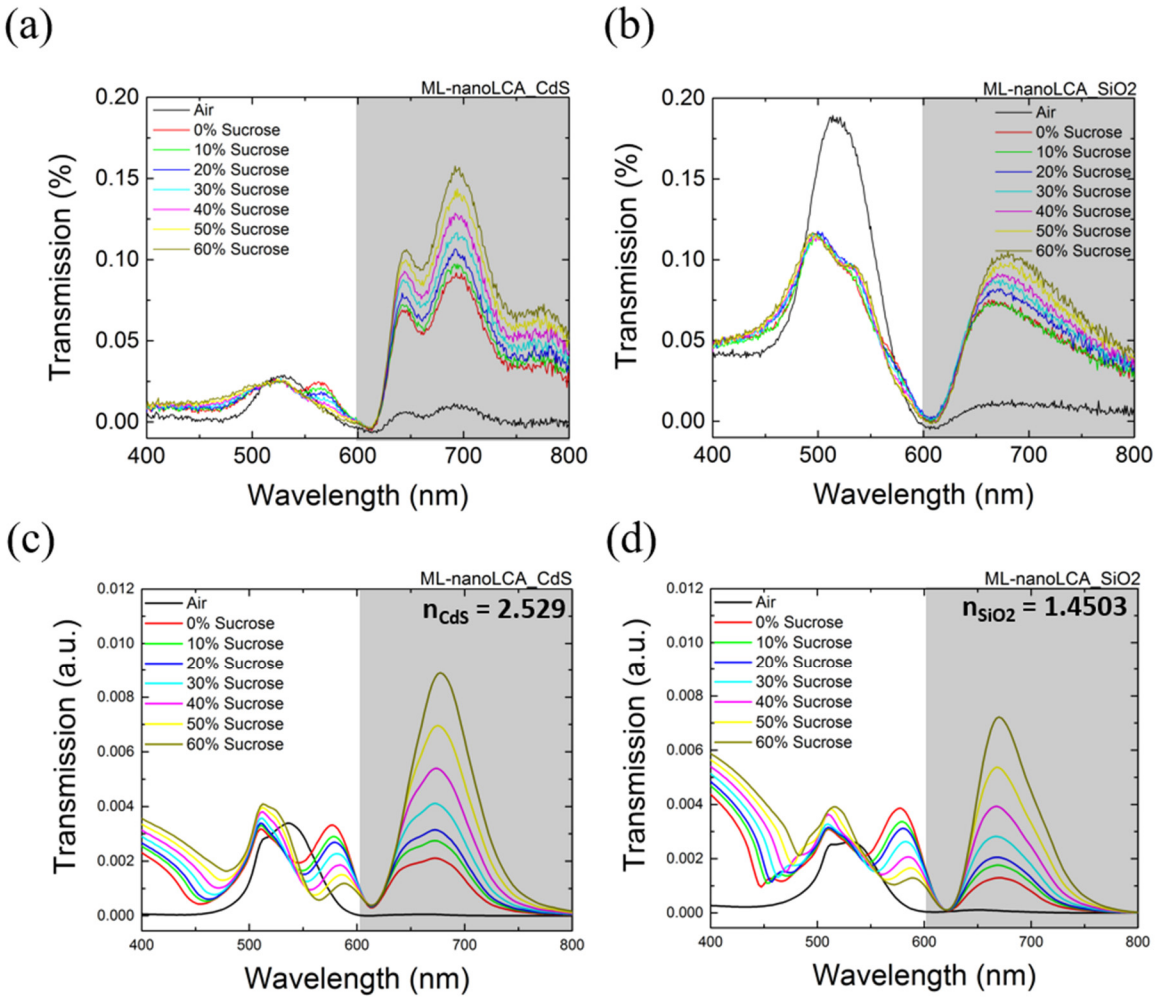

Figure 5.4 Comparison between the optical properties of ML-nanoLCA for SiO_2 and CdS as a sandwiched layer with respect to the different concentration of the sucrose solution (from 0% to 60%). (a) and (b) are the experimental results, whereas (c) and (d) are the FDTD simulation respectively. In SiO_2 case; the peak position of the transmission spectrum is changing with respect to the higher concentration of the sucrose solution. The spectrum also shows a small increase in the intensity as compare to the ML-nanoLCA device (b), where there is no shift in the peak position.

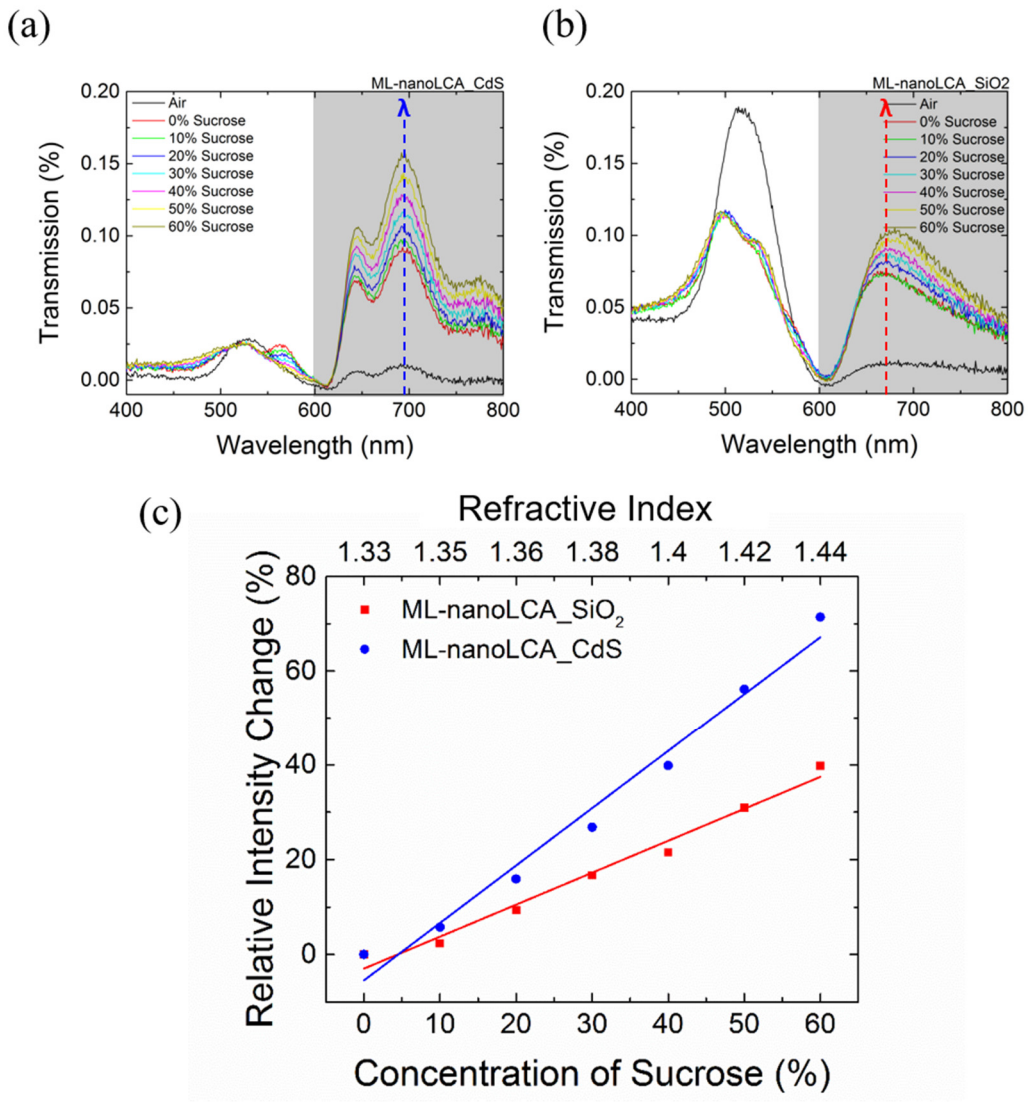

Figure 5.5 Sensitivity analysis of ML-nanoLCA devices by using CdS (a) and SiO_2 (b) respectively as a sandwiched layers. (c) Shows the graph by comparing the relative intensity change of ML-nanoLCA device between CdS (a) and SiO_2 (b) with respect to the different concentration of the sucrose solution. The sensitivity of the devices is calculated by the relative change in the transmission (*T*) intensity at specific wavelength in the unit of Δ%T-nm/RIU. In case of CdS, the device sensitivity is significantly improved and calculated as 660 Δ%T-nm/RIU (with respect to air, 4000 Δ%T-nm/RIU) at λ = 695nm as compare to SiO_2 device which is 340 Δ%T-nm/RIU (with respect to air, 2000 Δ%T-nm/RIU) at λ = 672 nm.

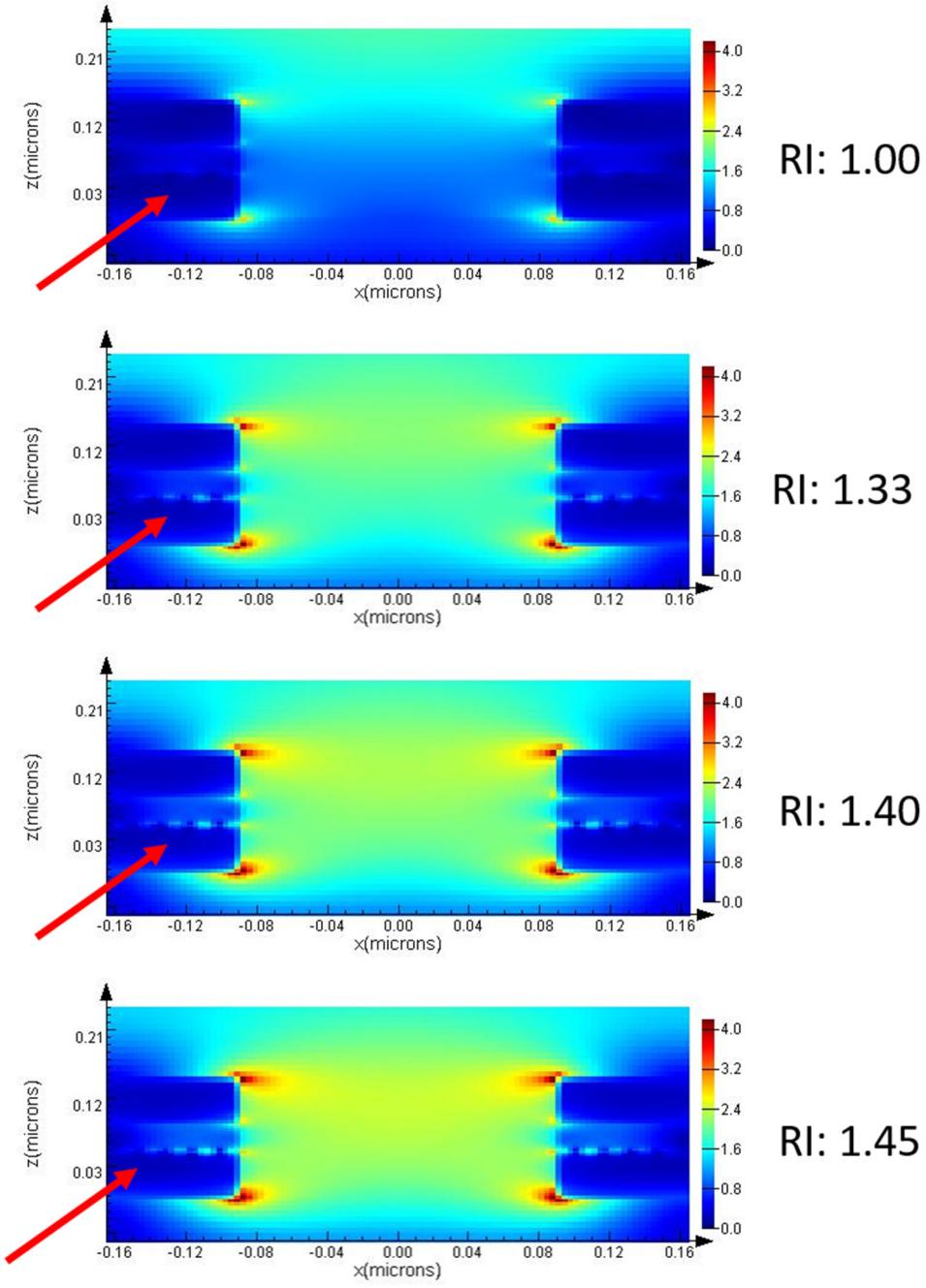

Figure 5.6 Shows the 3D-FDTD simulation for electric field (E-field) distribution on the cross-section of the simplified arrays of nanohole structure. As the refractive index of the material on the superstrate increases, the E-field intensity between the Au and CdS interface increases, which is indicated by red arrow.

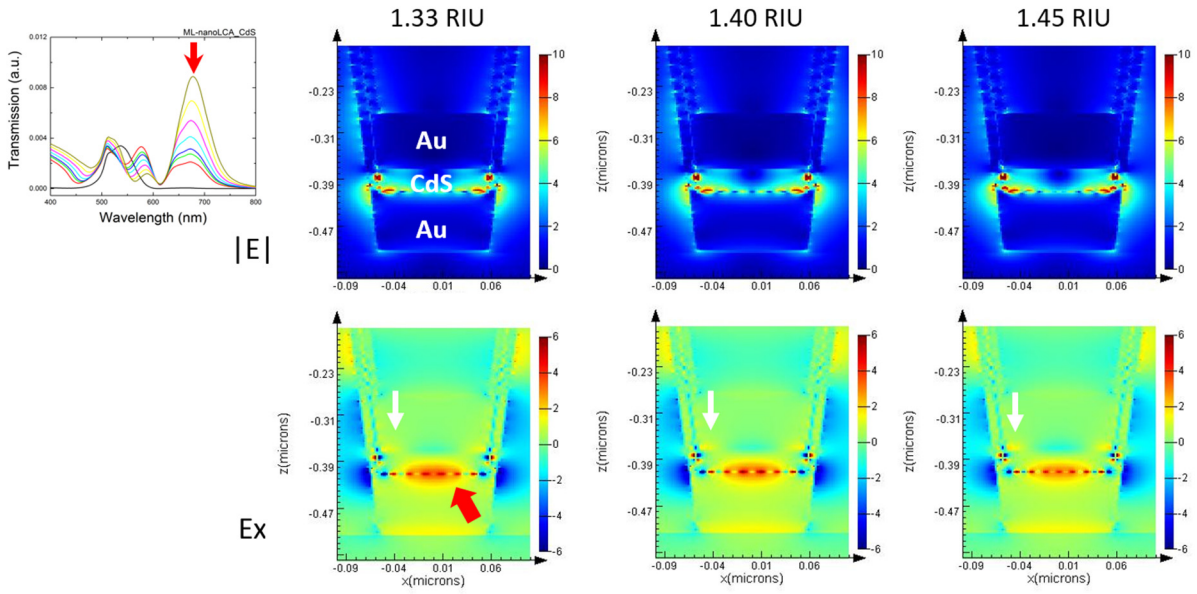

Figure 5.7 Shows the FDTD simulation for electric field (E-field) distribution on the cross-section of the device at the bright mode. Due to the higher refractive index of the sandwiched material, the E-field is confined at the interface of Au and CdS layer as indicated by the red arrow. As the RI of the superstrate is increased, the intensity of the E-field is decreased at the interface between the dielectric and the bottom Au layer but is increased in the top Au layer (indicated by white arrow) which enables the out-coupling of electric field to the top Au layer; hence, the overall transmission intensity is enhanced.

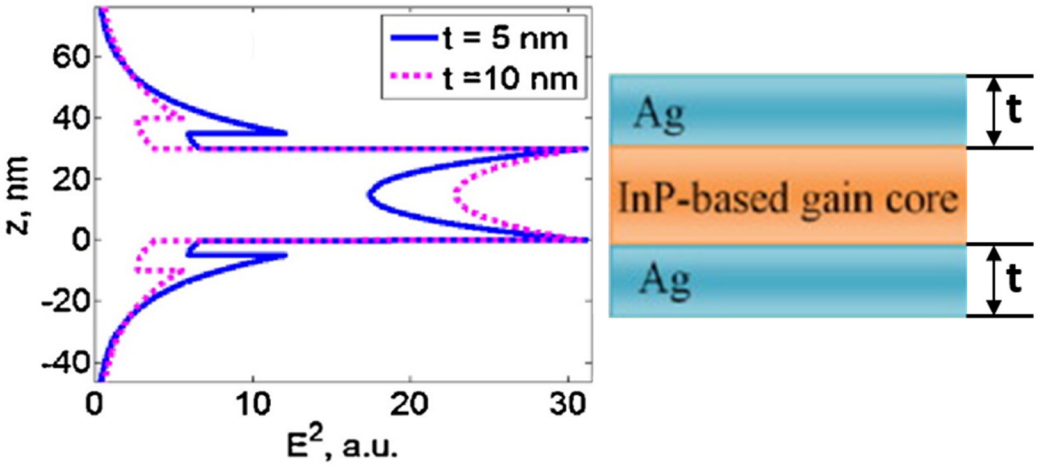

Figure 5.8 Shows the Electric field distribution in the case of Multilayer device. From the left Figure, we can see that with smaller thickness of the top and bottom metal layers, more E-field is confined closer to the metal surfaces and less E-field is confined inside the sandwiched layer, which may increase the out coupling of the light. Adopted from [193].

CHAPTER 6

LABEL FREE BIOMOLECULAR DETECTION USING 3D PLASMONIC NANO-CAVITY STRUCTURES ON PERIODIC NANOCUP ARRAYS

6.1 Introduction

Development in the research efforts to optimize materials, mechanics and fabrication techniques enable the use of label free biosensing for the analysis of interactions between small molecules/peptides and proteins. Label-free sensors for detection of low concentrations of biomolecules, such as cancer biomarkers, are highly sought after for applications including drug discovery research and point-of-care diagnostics. Clinical biomarker level measurements are currently done using the ELISA or fluoroimmunoassay techniques, which are time consuming methods that require sophisticated instrumentation available only to those working in specialized laboratory settings.[194] Towards development of portable label-free sensors, optical devices such as the photonic crystal [195], ring resonator [196], interferometer [197], and surface plasmon resonance (SPR) sensor [198] which rely on molecular binding at a surface are especially promising for miniaturized devices that require a low sample amount. While these devices provide ultrasensitive detection, specialized equipment including large external optical setups with precise alignment are required, which limits widespread applications.

Here, we report the combination of a sensor based on EOT with a multilayer nanocavity structure for the detection of the cancer biomarker carcinoembryonic antigen (CEA). Multilayered plasmonic structures have been increasingly investigated for on-chip photonic devices, such as multilayered plasmonic waveguides.[173, 193, 199, 200] The LSPR effect, which results in

increased absorption, has been used to increase light-induced catalytic activity of materials such as palladium and CdS where the coupling between the plasmon resonance of a metallic nanoparticle and the catalytic material is controlled by a dielectric spacer.[201, 202] The surface plasmon effect in metal-insulator-metal (MIM) and metal-semiconductor-metal (MSM) waveguides has also been studied for refractometric detection.[203, 204] The study of dielectric films and MIM structures combined with an EOT substrate has been reported previously.[205-208] However, these works primarily focused on the extinction peak instead of the transmission peak in nanohole arrays. The sensitivity of these structures was not compatible with detection of a low concentration of biomolecules. In addition, the cavity mode resulting from the nanocavity structure was not utilized in the distinct method presented here.

In our multilayer nanoLCA (ML-nanoLCA) device, a transmission peak occurs in the visible or NIR (depending on the thickness of CdS) due to the excitation of SPP-BW at the Au-CdS interface, while the nanocavity confines the optical energy between the Au layers. Biomolecules binding at the interface between the water superstrate and top Au layer will result in an increase in the RI at this interface. This then causes an increase in the measured transmission intensity of the peak resonance wavelength, representing out coupling from the mode confined between the Au layers to the superstrate. However, no change in RI is occurring at the Au-CdS interface and therefore there is no shift in the peak. Detection can be done by simply monitoring the change in transmitted intensity at the resonance wavelength. In addition, our sensor contains a reference point where no intensity change occurs with increasing RI. Therefore, the sensor is self-referencing and the changing intensity value of the resonance peak can be read directly without any corrections. Other groups have reported intensity based detection of molecular binding events using EOT devices where binding events typically result in a decrease in transmission intensity

(increase in absorbance).[69, 185] However, complex experimental setups and substantial post-processing of the data are required to obtain consistent results since these spectral features also contain shifts and no reference points.

In this chapter, we describe the fabrication, optical characterization, and principle of operation of the ML-nanoLCA device along with demonstration of biomolecular detection. In particular, DNA hybridization and biotin-streptavidin binding are demonstrated as a proof of concept. The device design is then further optimized by theoretical analysis of the cavity mode in order to obtain higher mode confinement with stronger out coupling as the RI of the superstrate increases. We then apply this optimized sensor to the detection of the cancer biomarker CEA. CEA is produced during fetal development and its production terminates before birth. The normal level of CEA for a healthy person is around 3-5 ng/mL.[209] However, there is a considerable increase (>10 ng/mL) in its concentration in conditions like lung cancer [210], colorectal carcinoma [211], and breast carcinoma.[212, 213] Moreover, when CEA levels are heightened due to cancer, they return to normal levels following successful therapy.[214]

CEA can then be used as a biomarker for both detection and prognosis of cancer. Due to scarcity of both rapid and sensitive diagnostics, CEA related cancers cannot be detected at an early stage, which is crucial for improved anticancer therapy.[194] Here we report a label-free limit of detection (LOD) of 1 ng/mL (5 pM) for CEA on our ML-nanoLCA device simply by monitoring the change in the intensity value at the resonance peak wavelength. In contrast, the LOD is 1 µg/mL for CEA on the nanoLCA device with no cavity structure. In addition, a LOD of 100 ng/mL for CEA was reported for the commercially available SPR system (Biacore 3000).[215] In this case, a secondary antibody label was required to reduce the LOD to 3 ng/mL.

As discussed earlier, in our hybrid nanocavity plasmon resonance sensor, a resonance occurs with a significant intensity change, but no spectral shift, while increasing RI. The device is robust in that the results are independent of angle and polarization of the incident light. In addition, no high end spectrometer or other specialized equipment is required. We demonstrate sensitive detection in the dynamic range relevant for cancer biomarkers. As we report here, the resonance can be tuned to occur in the visible range. Therefore, there is high potential for this device to operate in a large array where detection is done by an image and simple image processing can be used to detect the change in intensity due to molecular binding events. We anticipate that these advantages of our device will allow for the full development of a portable port-of-care biosensor for early detection of low concentrations of disease biomarkers.

6.2 Materials and methods

6.2.1 DNA hybridization

DNA-1 (5' thiol-GTT GTG TCC TGC TAA GTC CT), which is a ssDNA modified with a thiol group, was mixed with tris(2-carboxythyl)phosphine hydrochloride. The solution was incubated on the ML-nanoLCA surface at a concentration of 10 μM for 16 hours at 37 ºC to break the S-S bond and immobilize the DNA-1 on the top Au surface. The device was then incubated in a blocking thiol solution MCH (6-mercapto-1-hexanol) at a concentration of 1 μM for 1 hour at room temperature. For the final hybridization step, the ML-nanoLCA device was immersed in a 1 μM DNA-2 (3' complimentary base pair) solution for 16 hours at 37 ºC. Following each incubation step, the device was washed with Milli-Q water, dried with nitrogen (N_2), and the transmission spectrum was taken in water. (All materials were purchased from Sigma-Aldrich).

6.2.2 Streptavidin-biotin binding

The ML-nanoLCA device was incubated in a 1 mM solution of thiolated biotin at 37 ºC followed by immersion in a 1 mM MCH (6-mercapto-1-hexanol) blocking solution for 2 hours at room temperature. In order to assess streptavidin binding to the immobilized biotin, the ML-nanoLCA device was immersed in a 1 µg/mL (18.9 nM) streptavidin solution at room temperature. Following each incubation step, the device was washed with Milli-Q water, dried with nitrogen (N_2), and the transmission spectrum was taken in water. The binding of streptavidin was also monitored with respect to time by taking the transmission spectrum during the incubation. (All materials were purchased from Sigma-Aldrich).

6.2.3 CEA detection

The devices were first incubated in a MUA solution in ethanol for 24 hours at room temperature. The devices were then cleaned in 70% ethanol, dried in N_2, and the transmission spectra were taken in Milli-Q water. The devices were then dried in N_2 followed by incubation in a 1:1 mixture of 400 mM EDC and 100 mM NHS (both in Milli-Q water) at room temperature for 30 minutes. The devices were then rinsed in PBS and immediately incubated with 30 µg/mL monoclonal anti-CEA antibody at room temperature for two hours. In the case of the antibody control, the device was incubated with 30 µg/mL mouse IgG for two hours at room temperature. The sensors were then rinsed in PBS, dried with N_2, and the transmission spectra were taken in water. The sensors were then incubated for 30 minutes at room temperature in a 30 µg/mL BSA blocking solution followed by incubation for 30 minutes at room temperature in a 10% ethanolamine solution to cap the non-reacted NHS esters. The devices were then rinsed in Milli-Q water and the transmission spectra were taken. Finally, the devices were immersed in different concentrations of CEA for two hours and the transmission spectra were taken in order to detect

binding of CEA at the ML-nanoLCA surface. (All materials were purchased from Sigma-Aldrich). Detection of CEA was also carried out in human serum samples. Devices were functionalized as described previously, but for the final incubation 1 μg/mL and 100 ng/mL of CEA were spiked in human blood serum samples (Zen-Bio) and incubation was done for two hours before cleaning in Milli-Q water and taking the transmission spectra.

6.3 Results and discussion

As discussed in previous chapter that the device will be optimized to detect surface binding events at lower concentration with high sensitivity. First, for a proof of concept for label-free detection of biomolecular interaction on the surface of the ML-nanoLCA, we performed hybridization of single-stranded DNA (ssDNA). A schematic of the hybridization process is illustrated in Figure 6.1. The ML-nanoLCA device is first immersed in a 10 μM solution of ssDNA probes (DNA-1), which are modified by a thiol group and therefore can be immobilized onto the top Au layer.[216] The device is then immersed into a 1 μM thiol blocking solution (MCH) followed by immersion in a 1 μM DNA-2 (3' complimentary base pair) solution and the hybridization reaction occurs. Figure 6.2 (a) shows the transmission spectra measured after each processing step and Figure 6.2 (b) shows the percentage change in transmission intensity following each step. There is an increase in the transmission intensity due to surface adsorption of DNA-1. A very small decrease in intensity is observed following MCH incubation, in agreement with the blue shift that occurs on conventional EOT sensors following incubation in blocking solutions. The hybridization reaction is detected by an increase in transmission intensity at the resonance wavelength following immersion in the DNA-2 solution.

In an additional proof of concept study, the ML-nanoLCA structure was evaluated for detection of streptavidin-biotin binding as illustrated in Figure 6.3 (a). The streptavidin-biotin system has high affinity ($K_a \sim 10^{15}\ M^{-1}$), which has been exploited to functionalize biomolecules such as proteins, nucleic acids, antibodies.[217, 218] The surface of the ML-nanoLCA sensor was functionalized with a self-assembled monolayer formed by incubation in a 1 mM biotinylated thiol solution followed by immersion in a 1 mM MCH blocking solution. The device was then immersed in a 1 μg/mL (18.9 nM) streptavidin solution and the binding was monitored. The transmission spectra for each processing step is shown in Figure 6.3 (b) with the percentage change in the transmission at the resonance wavelength shown in Figure 6.3 (c). As expected, immobilization of the biotinylated thiol resulted in an increase in the transmission intensity at the peak wavelength, immersion in the MCH solution resulted in a small decrease in the transmission intensity at the peak wavelength, and binding of streptavidin to the surface resulted in a transmission increase at the resonance wavelength. The transmission measurement was performed over time to monitor streptavidin binding as shown in Figure 6.3 (b). From both the experiments, it is verified that ML structure is sensitive in detecting surface binding events.

The detection of DNA hybridization and streptavidin-biotin binding shows that the ML-nanoLCA is well-equipped to detect the RI change occurring at the Au-superstrate interface due to molecules binding onto the device surface. This was accomplished by simply monitoring the percent change in intensity at the transmission peak resonance wavelength. Before carrying out detection of the cancer biomarker CEA, we optimized the nanocavity structure in order to further improve the sensitivity of the ML-nanoLCA device to achieve a low LOD. Figure 6.4 (a) shows the sensitivity measurement of the modified ML-nanoLCA structure, we added different concentrations of sucrose solutions (from 0% to 60% mixed in Milli-Q water) on the superstrate,

similar to the sensitivity measurement in previous chapter. Here, we have used higher thickness of the core layer (CdS~80nm). This change in concentration of the sucrose corresponds to a bulk RI change of 1.33 to 1.44. As expected, with increasing RI there is a higher increase in the relative intensity of the resonance peak in the transmission spectrum. The comparison of the sensitivity measurement is shown in Figure 6.4 (b). Furthermore, as we have discussed in the last chapter, thickness of the metal layers in ML-nanoLCA structure is another parameter to play with the plasmonic coupling efficiency and overall transmission intensity. The thickness of the metal layers, for the current structure, is 90nm and 25nm on bottom and top respectively. By decreasing the thickness of the top Au layer, there is no significance change in the output intensity, however, by changing the thickness of the sandwiched layer (CdS), the resonance is shifted to 760nm instead of 700nm with previous device. Moreover, the sensitivity of the device is almost double as compare to the previous device structure. These results are further verified with the 3D-FDTD simulation

The schematic of the detection of the CEA biomarker is illustrated in Figure 6.5. In order to functionalize the surface of the ML-nanoLCA for CEA detection, we first immersed the device in a 10 mM 11-mercaptuoudecanoic acid (MUA) solution, which formed a self-assembled monolayer on the Au surface. The CEA antibody (30 µg/mL) was then covalently bound to the MUA by activation in a mixture of 1-ethyl-3-(3dimethylaminopropyl)-carbodiimide (EDC) and N-hydroxysuccinimide (NHS). The device was then incubated in a BSA thiol blocking solution followed by incubation in an ethanolamine solution, which reacts with any remaining NHS. Finally, the ML-nanoLCA devices were incubated in different concentrations of CEA in PBS solutions from 0.1 ng/mL to 1 µg/mL. A vehicle control (PBS containing no CEA) was also used in addition to an antibody control. In the case of the antibody control, the non-specific binding

between 1 μg/mL of CEA to anti-mouse IgG was measured. We also prepared nanoLCA devices containing no cavity structure with the same surface functionalization and detected the binding of 100 ng/mL and 1 μg/mL CEA to immobilized anti-CEA and compared to the vehicle control and antibody control.

A LOD for the nanoLCA with no cavity structure, where conventional EOT detection is carried out by measuring the red shift in the transmission peak wavelength, is 1 μg/mL. This is consistent with our previous results of biomolecule detection on the nanoLCA device.[184] Both controls resulted in no peak shift. A bar graph showing the percent intensity increase for the different concentrations of CEA along with the controls is shown in Figure 6.6 (a). As can be seen, the LOD for the ML-nanoLCA was 1 ng/mL, where detection was done by measuring the change in intensity at the resonance transmission peak wavelength. There was a small percentage increase in intensity for the antibody control (less than 1%) and a small percentage decrease in intensity for the vehicle control (less than 0.5%). Figure 6.6 (b) shows a plot of the percent intensity increase as a function of CEA concentration on a log scale. The data was fitted to a linear model and showed good agreement over the dynamic range tested (1 ng/mL to 1000 ng/mL). A plot of the intensity values as a function of time is shown in Figure 6.7 during the immobilization steps and the binding of 10 ng/mL CEA on ML-nanoLCA device.

6.4 Conclusion

In this chapter, we describe the fabrication, optical characterization, and principle of operation of the ML-nanoLCA device along with demonstration of biomolecular detection. First, for a proof of concept for label-free detection of biomolecular interaction on the surface of the ML-nanoLCA, we performed hybridization of single-stranded DNA (ssDNA). Then, an additional

proof of concept study is performed as the ML-nanoLCA structure is evaluated for detection of streptavidin-biotin binding. We have successfully demonstrated the binding detection of 18.9nM streptavidin molecules with biotin molecules immobilized on the surface of ML-nanoLCA. The device design is then further optimized by theoretical analysis of the cavity mode in order to obtain higher mode confinement with stronger out coupling as the RI of the superstrate increases. We then apply this optimized sensor to the detection of the cancer biomarker CEA. The device also provides a greatly improved LOD (5 pM for CEA) over typical EOT sensors and commercially available SPR systems and has a dynamic range in the concentrations relevant for human cancer biomarker detection.DNA We studied the molecular binding kinetics on the ML-nanoLCA sensing surface with respect to time and calculated the important kinetic parameters (i.e., K_D). In this work, the sensitivity of the plasmonic nanocavity device was almost doubled by adjusting the thickness of the cavity layer. It is expected that further optimization of the coupling between the EOT plasmonic sensor and nanocavity will improve the LOD even further enabling highly sensitive, portable, and robust detections of biomolecular binding events.

6.5 Figures

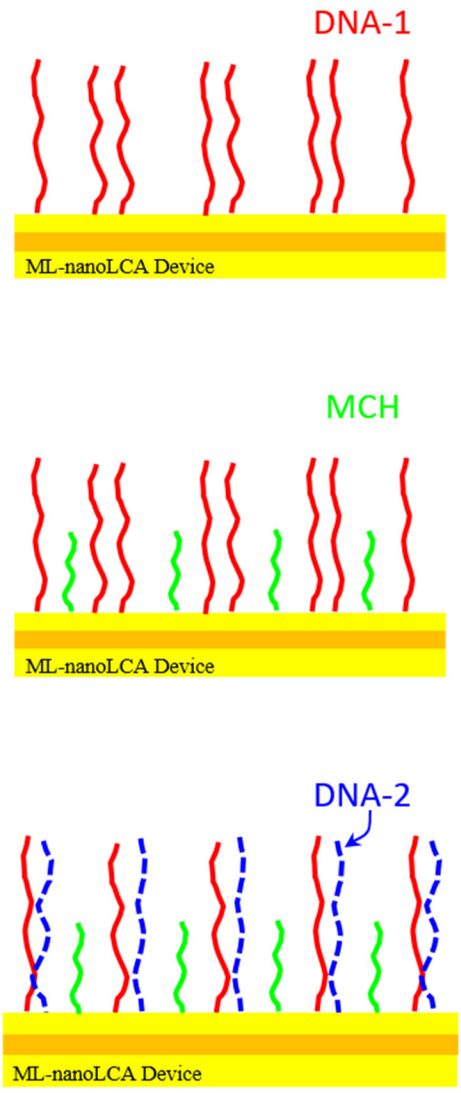

Figure 6.1 Schematic illustration of single-stranded DNA-hybridization on ML-nanoLCA device. Starting from top to bottom. First, the ML-nanoLCA device is immersed in the DNA-1 (5' thiol-GTT GTG TCC TGC TAA GTC CT) for immobilization. Then the device is immersed in the MCH (6-mercapto-1-hexanol) solution which is blocking thiol to cover the surface where there is no immobilization of DNA-1 molecules. Finally, the device is immersed in the DNA-2 (3' complimentary base pair) solution to bind with DNA-1 molecules.

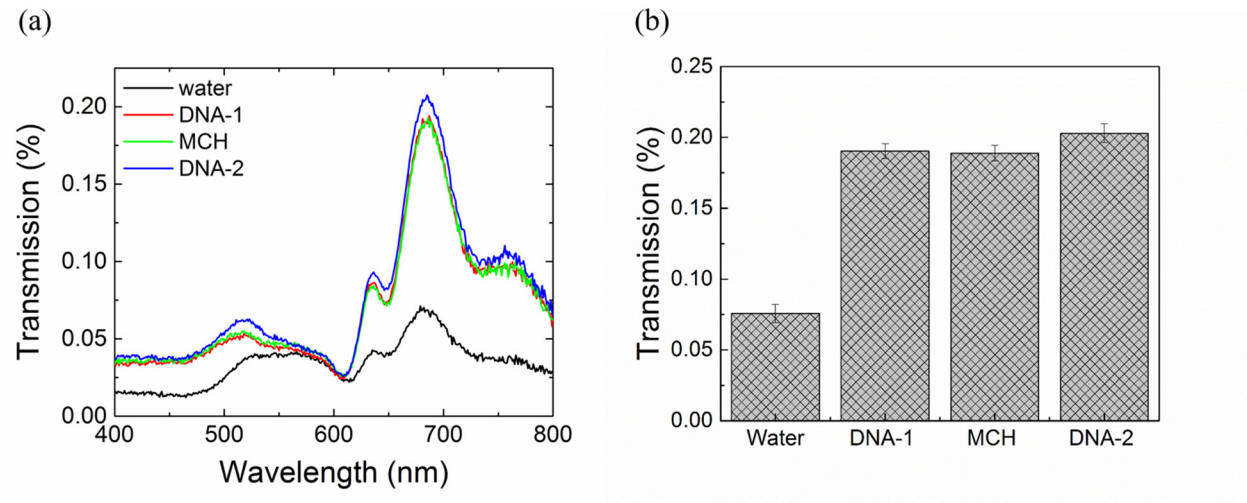

Figure 6.2 Optical transmission response of the ML-nanoLCA device to detect DNA-hybridization. (a) Transmission spectra of the device to detect hybridization of ssDNA following each processing step. (b) Shows the percentage change in the transmission intensity during the process of DNA-hybridization with respect to time. The reaction on the surface of the device with different incubation steps is identified with the increase in the transmission intensity of the device as expected. A very small decrease in intensity is observed following MCH incubation, in agreement with the blue shift that occurs on conventional EOT sensors following incubation in blocking solutions.

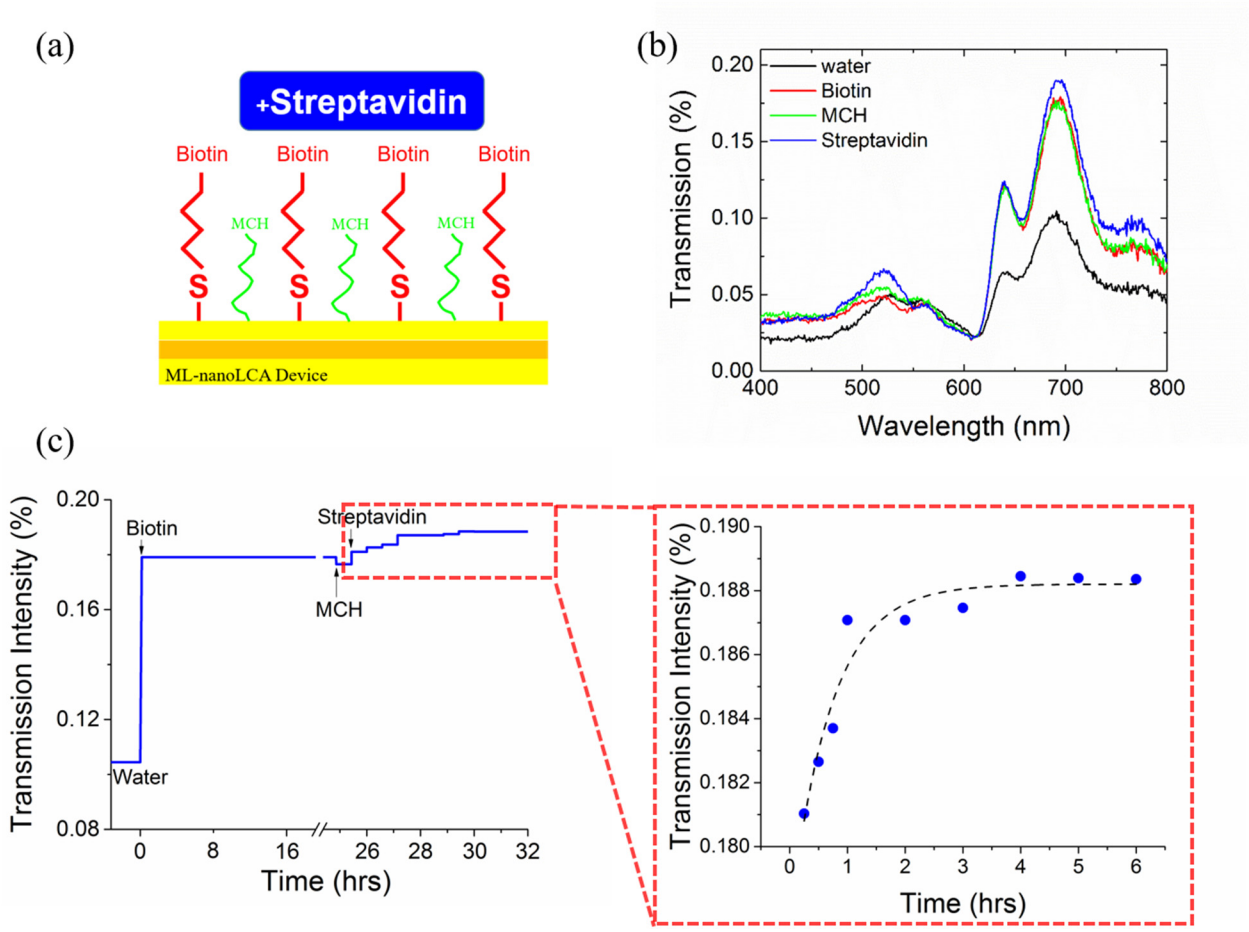

Figure 6.3 Optical response of the ML-nanoLCA device to detect biotin-streptavidin binding. (a) Schematic of biotin immobilization and streptavidin binding onto the ML-nanoLCA surface. The process is similar to the DNA-hybridization detection as it starts with incubation in the biotin solution followed by MCH solution and finally incubation in streptavidin solution. (b) Transmission spectra of the device during biotin-streptavidin binding. (c) (left) Binding of biotin with streptavidin with respect to time detected by the change of the peak transmission intensity of the device and on the right plot shows, the percent change in transmission at the peak wavelength with respect to time during streptavidin binding.

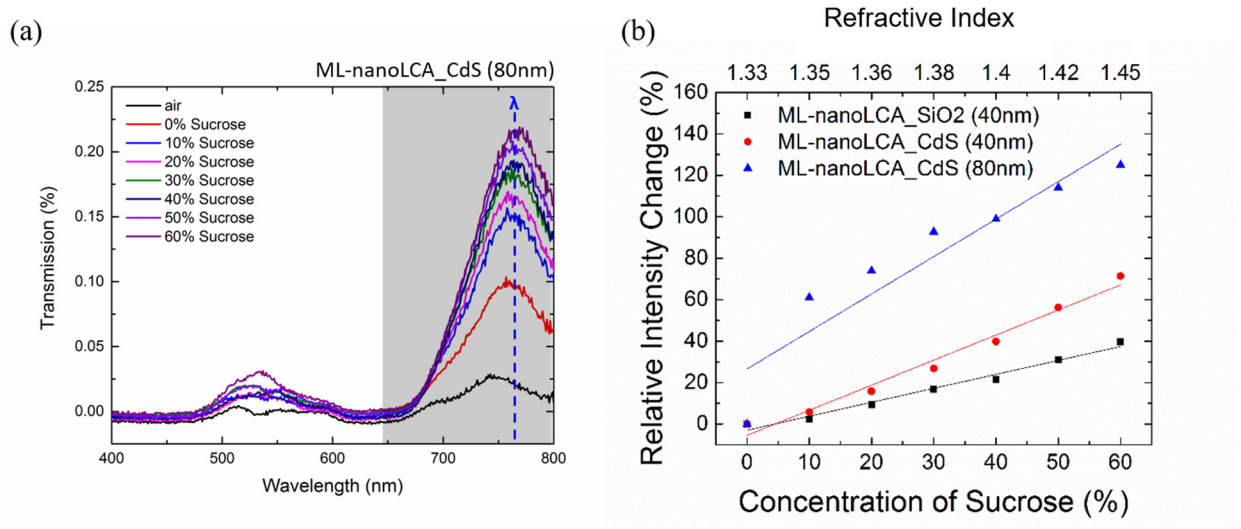

Figure 6.4 (a) Shows the sensitivity analysis of the modified ML-nanoLCA structure with respect to the different concentration of the sucrose solution (from 0% to 60%). (b) Shows the graph by comparing the relative intensity change of old design of ML-nanoLCA device between with 40nm thickness of CdS (660 Δ%T-nm/RIU) and SiO_2 (340 Δ%T-nm/RIU) and comparing the sensitivity with the modified ML-nanoLCA with 80nm of CdS (1150 Δ%T-nm/RIU) with respect to the different concentration of the sucrose solution.

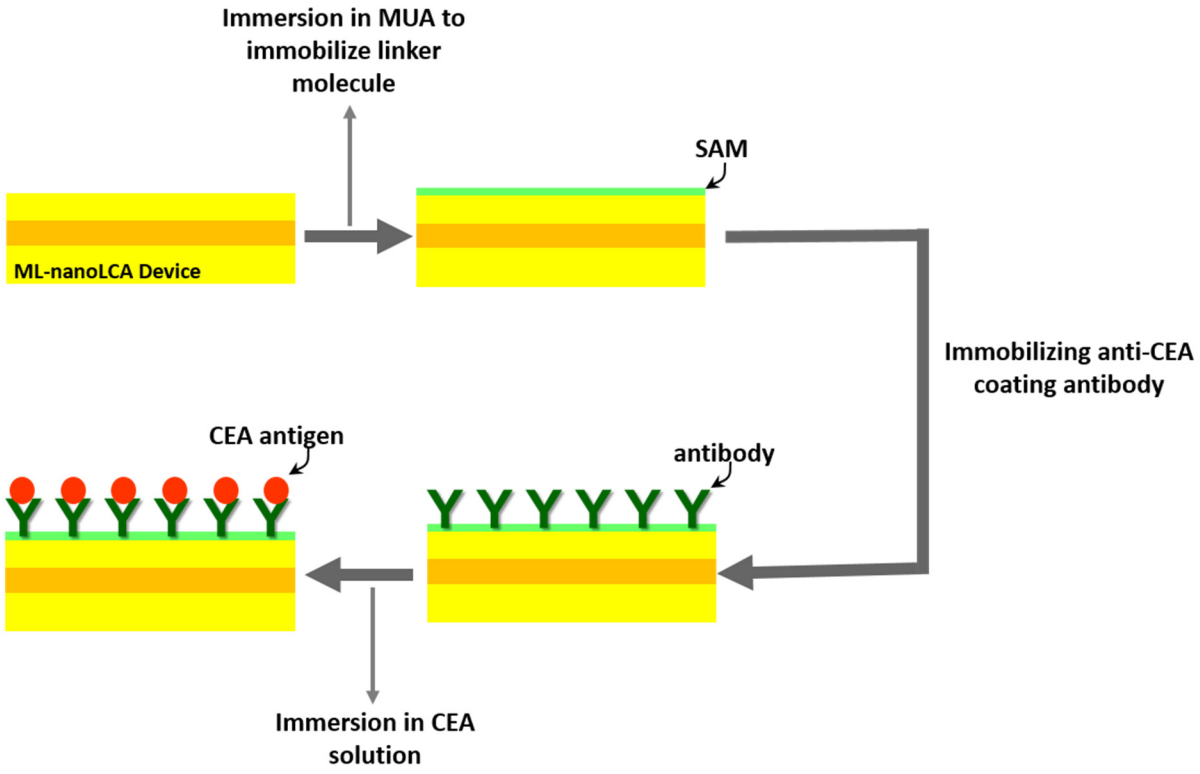

Figure 6.5 Shows the schematic illustration of the detection of cancer biomarker, Carcinoembryonic Antigen (CEA), on ML-nanoLCA device. The ML-nanoLCA device will be immersed in the 11-mercaptuoudecanoic acid (MUA) solution, which formed a self-assembled monolayer on the top Au surface. The CEA antibody (30 µg/mL) was then covalently bound to the MUA by activation in a mixture of 1-ethyl-3-(3dimethylaminopropyl)-carbodiimide (EDC) and N-hydroxysuccinimide (NHS). The device was then incubated in a BSA thiol blocking solution followed by incubation in an ethanolamine solution, which reacts with any remaining NHS. Finally, the ML-nanoLCA devices were incubated in different concentrations of CEA for detection.

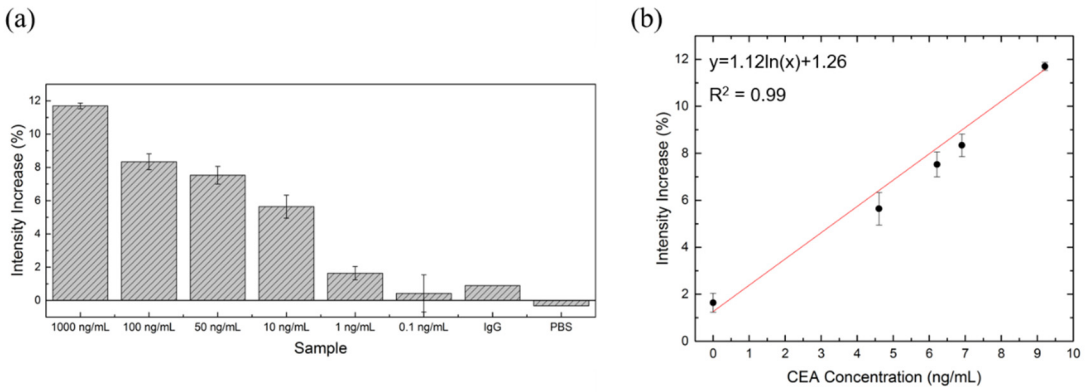

Figure 6.6 Detection of CEA on the ML-nanoLCA device. (a) Bar graph showing the percent intensity increase for six different CEA concentrations along with the antibody control (IgG) and the vehicle control (PBS). As can be seen, the LOD is 1 ng/mL. (b) Plot of percent intensity increase as a function of CEA concentration (log scale). The data is fit to a linear model.

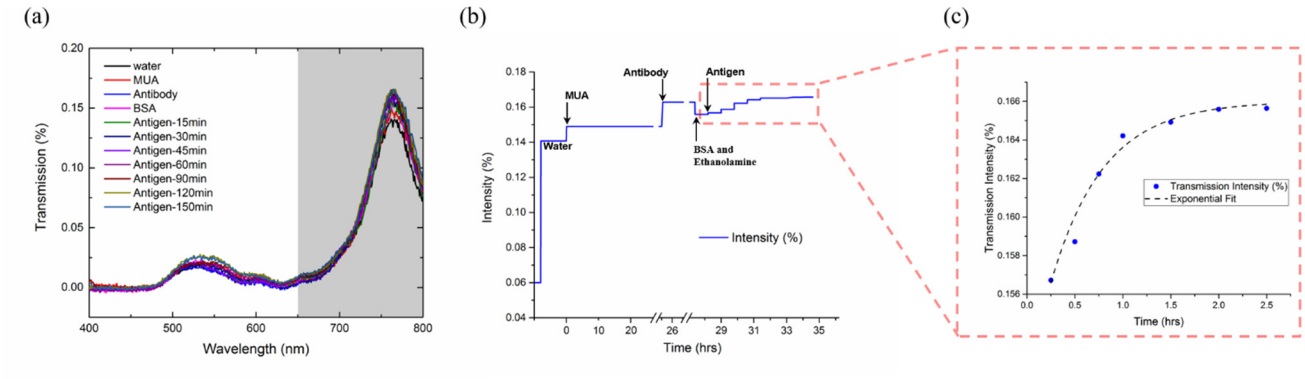

Figure 6.7 Detection of 10ng/mL CEA on the ML-nanoLCA device. (a) Transmission spectra of the device during CEA antibody-antigen binding. (b) Plot of percentage intensity change with respect to time for CEA binding to the anti-CEA immobilized on the ML-nanoLCA device surface and (c) shows the CEA and anti-CEA binding kinetics.

CHAPTER 7

SUMMARY AND FUTURE OUTLOOK

7.1 Summary

As discussed, colorimetric sensing, a method that enables the detection of target analytes via 'color change', lays the foundation of a user-friendly, economical and most of all, it's accessibility to draw inference for the detection of notorious critical conditions such as, carcinomas, and other significant environmental monitoring. Therefore, the impact of colorimetric sensing on the clinical detection of diseases at earlier stages can be enormous, provided the gap between the accuracy of lab-equipment to point-of-care testing tools is approximated. The optical properties of the plasmonic sensor are very similar to the Lycurgus Cup of the ancient Romans, therefore, this plasmonic sensor is referred as nanoscale Lycurgus cup array (nanoLCA). The fabrication techniques of the nanoLCA device, integration to portable microfluidic devices for lab on chip applications, demonstration of highly sensitive refractive-index sensing, DNA hybridization detection, protein-protein interaction and different drugs binding with Cytochrome P450-2J2, which is the most common P450 protein found in the human heart, are discussed. We anticipate that the colorimetric sensor can be applied to point-of-care diagnostics by utilizing proper surface functionalization techniques, which seems to be one of the current limiting factors.

In order to increase limit of detection to detect lower concentration of biomarker, further modification is done on nanoLCA to obtain 3D-plasmonic nano cavity structure also referred as ML-nanoLCA device. The ML-nanoLCA device is fabricated by thin film semiconductor material such as cadmium sulfide (CdS) layer, which has high refractive index (n~2.53) and very low

extinction coefficient, sandwiched between two Au layers on a nanostructured PET sheet. The Au-CdS-Au nanocup array structure allows sensing based on the transmission intensity change with the help of simple bandpass filter to allow certain wavelength to be transmitted in a visible region at normal incidence illumination. Due to the excitation of a plasmon resonance at the Au CdS interface and high refractive index of the sandwiched layer, CdS thin film which acts as a resonant cavity, electric field is confined at the interface of Au and CdS layer at lower surrounding refractive index. An increase in the surrounding refractive index causes a decrease in the electric field intensity at the interface but an increase in out-coupling of electric field on the topmost Au layer, hence, enhancement in overall transmission intensity is observed.

A brief Summary of each chapter is given as follows:

- Chapter 2: The chapter starts with the fabrication of different plasmonic devices and their optical properties. Then, a recent developed plasmonic sensing platform (nanoLCA) is discussed with its design, fabrication and characterization. A brief review on micro fluidic device integration, optical illumination and detection on nanoLCA is discussed. Furthermore, we have discussed the method of analysis for detection of different molecules on top of the nanoLCA device is discussed.
- Chapter 3: Further characterization of the nanoLCA device is performed in this chapter. First, we have discussed the influence of superstrate and substrate on the optical properties of the device. The influence of superstrate is determined by changing the refractive index of the surrounding medium, whereas, the effect of substrate is observed by changing the thickness of adhesion layer, Ti, on both spectral and colorimetric properties of the nanoLCA device in transmission and reflection mode. 3D-FDTD simulation is performed to investigate the localized electric field confinement at different interfaces of the nanoLCA device and

presented the optimized thickness for better sensitivity. Furthermore, in this chapter, LBL deposition of alternating polyelectrolyte layers, at 2nm resolution, is used to determine the sensing depth (decay length) of the nanoLCA plasmonic device as ~193 nanometers.

- Chapter 4: Application of nanoLCA device to detect the substrate binding with Cytochrome P450-2J2 with incorporation of Nanodiscs to stabilize the cytochrome protein in the solution. We found the spectral properties of the nanoLCA device to be highly reliable, which allowed the detection of substrate dependent and concentration dependent blue shifts, corresponding to the binding of type I substrates to CYP2J2-NDs. The results are confirmed by traditional solution-based absorption spectroscopy and a FDTD simulation study. Colorimetric measurements are also performed which indicates that the nanoLCA device has a strong potential for the future development of a high-throughput spectroscopic on-chip method for detecting drug binding to cytochrome P450 proteins.
- Chapter 5: In this chapter, we have demonstrated a new design, fabrication and characterization of label-free biosensor using 3D plasmonic nano cavity structure known as ML-nanoLCA device. In ML-nanoLCA device, we have combined optical resonance cavity with the plasmon resonance all together to improve the sensitivity with simplified detection mechanism to detect surface binding events on top of the device. The sensitivity of the ML-nanoLCA structure, is measured by adding different concentrations of sucrose solutions (from 0% to 60% mixed in Milli-Q water) on top of the device which cause a change in bulk refractive index from 1.33 to 1.44. The calculated sensitivity of the ML-nanoLCA device with CdS is 660 Δ%T/RIU (4000 Δ%T/RIU with respect to air at λ = 695nm). These results further verified with 3D-FDTD simulation.

- Chapter 6: After optimization of the ML-nanoLCA device, for a proof of concept for label-free detection of biomolecular interaction on the surface of the ML-nanoLCA, we performed hybridization of single-stranded DNA (ssDNA). Then, an additional proof of concept study is performed as the ML-nanoLCA structure is evaluated for detection of streptavidin-biotin binding. We have successfully demonstrated the binding detection of 18.9nM streptavidin molecules with biotin molecules immobilized on the surface of ML-nanoLCA. The device design is then further optimized by theoretical analysis of the cavity mode in order to obtain higher mode confinement with stronger out coupling as the RI of the superstrate increases, to detect cancer biomarker, CEA. CEA is extensively used in clinical analysis as a tumour biomarker and is produced during foetal development. The normal level of the CEA for a healthy person is around 3 to 5 ng ml^{-1}. In this chapter, we report a label-free limit of detection (LOD) of 1 ng/mL (5 pM) for CEA on our ML-nanoLCA device simply by monitoring the change in the intensity value at the resonance peak wavelength which indicates that the ML-nanoLCA device has a strong potential for the future development of a high-throughput point of care sensors.

7.2 Future outlook

Label-free plasmonic sensors, based on surface plasmon resonance (SPR) and localized surface plasmon resonance (LSPR), their microfabrication, instrumentations, integration to microfluidics, and applications for biofluids detection have been reviewed. The advancement of 3D nanohole fabrication techniques led to three-order of magnitude improvement in the FOM compared to colloidal nanoparticles.[64] The nanoimprint-based fabrication method enabled formation of 3D nanohole array with footprint of four-inch wafers with a lower cost.[64] Nanohole

array (i.e. nanoLCA substrate) has been designed for both spectroscopic and color imaging-based on-chip biosensing applications. It has been shown that a flow-through microfluidic integrated nanoLCA device can improve the response time by 14-fold compared to same sensor with flow-over sensing methods.[32] The nanohole array sensor, due to its advantages, will help realize portable, inexpensive, label-free, plasmon-based sensors with high sensitivity and high usability point-of-care diagnostics. Especially, colorimetric nanoplasmonic sensor combined with microfluidics can be integrated with existing mobile electronics such as cell phones and tablets or with existing bedside equipment such as drug infusion and blood transfusion apparatus. Multiplexed molecular detections in biofluidic samples including blood plasma, urine and saliva can be done with a simple colorimetric sensing on the nanoplasmonic sensor and yet at a much higher sensitivity and surface specificity in comparison with a choromophore-based colorimetric assay. Furthermore, the available point of care sensors can only detect a single and relatively high concentration analytes. Due to the lower sensitivity, there is no such point of care sensor available to detect the lower concentration of different biomarker. In the thesis, we have presented a new platform of sensing using ML-nanoLCA device, which enables the detection of target analytes using intensity based measurements at particular wavelength and can be detected using photodetector. There is no need of complex spectrophotometer to detect the change in the output intensity of the device, which enable its portability and ease of use with single wavelength light illumination or LED light and a photodetector. The nearly equipment-free nanoplasmonic sensing will completely transform the applications of SPR technology into new territories such as point-of-care diagnostics and telemedicine.

REFERENCES

[1] C. Sander, Science **287**, 1977-1978 (2000).

[2] H. F. Willard, M. Angrist and G. S. Ginsburg, **360**, 1543-1550 (2005).

[3] Lung Cancer's Impact, Lung Cancer Foundation of America (2015).

[4] A. Imran, W. Waseem A. and S. Kishwar, Cancer Therapy **8**, 56-70 (2011).

[5] American Cancer Society, Cancer Facts and Figures (2015).

[6] R. M. Lequin, Clinical Chemistry **51**, 2415-2418 (2005).

[7] H. K. Hunt and A. M. Armani, Nanoscale **2**, 1544-1559 (2010).

[8] Nature Publishing Group, a division of Macmillan Publishers Limited., Nature Photonics **6**, 707 (2012).

[9] J. N. Anker, W. P. Hall, O. Lyandres, N. C. Shah, J. Zhao and R. P. Van Duyne, Nat Mater **7**, 442-453 (2008).

[10] S. Singh, S. Gupta, A. K. Gupta, M. Singh and A. Kumar, Proceedings of the National Academy of Sciences India Section B-Biological Sciences **83**, 551-560 (2013).

[11] B. Liedberg, C. Nylander and I. Lunström, Sensors and Actuators **4**, 299-304 (1983).

[12] A. Aube, J. Breault-Turcot, P. Chaurand, J. N. Pelletier and J. Masson, Langmuir **29**, 10141-10148 (2013).

[13] W. Qi, J. Zhao, W. Zhang, Z. Liu, M. Xu, S. Anjum, S. Majeed, and G. Xu, Analytica Chimica Acta **787**, 126-131 (2013).

[14] Y. Yanase, T. Hiragun, T. Yanase, T. Kawaguchi, K. Ishii and M. Hide, Allergol. Int. **62**, 163-169 (2013).

[15] J. Byun, Y. Shin, T. Li, J. Park, D. Kim, D. Choi and M. Kim, Chem. communications (Cambridge, England) **49**, 9497-9499 (2013).

[16] Y. Xia, J. Ye, K. Tan, J. Wang and G. Yang, Anal. Chem. **85**, 6241-6247 (2013).

[17] S. Chen, M. Svedendahl, R. P. Van Duyne and M. Kall, Nano Letters **11**, 1826-1830 (2011).

[18] Z. Xu, Y. Chen, M. R. Gartia, J. Jiang and G. L. Liu, Appl. Phys. Lett. **98**, 241904 (2011).

[19] Z. Xu, M. R. Gartia, C. J. Choi, J. Jiang, Y. Chen, B. T. Cunningham and G. L. Liu, J. Raman Spectrosc. **42**, 1939-1944 (2011).

[20] P. K. Roy, Y. Huang and S. Chattopadhyay, J. Biomed. Opt. **19**, 011002 (2014).

[21] A. F. Chrimes, K. Khoshmanesh, S. Tang, B. R. Wood, P. R. Stoddart, S. S. E. Collins, A. Mitchell and K. Kalantar-zadeh, Biosens. Bioelectron. **49**, 536-541 (2013).

[22] J. N. Anker, W. P. Hall, O. Lyandres, N. C. Shah, J. Zhao and R. P. Van Duyne, Nature Materials **7**, 442-453 (2008).

[23] P. Howes D., S. Rana and M. Stevens M., Chem. Soc. Rev. **43**, 3835-3853 (2014).

[24] K. M. Mayer and J. H. Hafner, Chem. Rev. **111**, 3828-3857 (2011).

[25] B. Sepúlveda, P. C. Angelomé, L. M. Lechuga and L. M. Liz-Marzán, **4**, 244-251 (2009).

[26] E. Petryayeva and U. J. Krull, Anal. Chim. Acta **706**, 8-24 (2011).

[27] T. Chung, S. Lee, E. Y. Song, H. Chun and B. Lee, **11**, 10907-10929 (2011).

[28] M. -. Estevez, M. A. Otte, B. Sepulveda and L. M. Lechuga, Anal. Chim. Acta **806**, 55-73 (2014).

[29] K. A. Willets and R. P. Van Duyne, Annu. Rev. Phys. Chem. **58**, 267-297 (2007).

[30] J. Homola, Chem. Rev. **108**, 462-493 (2008).

[31] G. Spoto and M. Minunni, J. Phys. Chem. Lett. **3**, 2682-2691 (2012).

[32] C. Escobedo, Lab Chip, **13**, 2445-2463 (2013).

[33] O. Tokel, F. Inci and U. Demirci, Chem. Rev. **114**, 5728-5752 (2014).

[34] A. Krishnan, T. Thio, T. J. Kim, H. J. Lezec, T. W. Ebbesen, P. A. Wolff, J. Pendry, L. Martin-Moreno and F. J. Garcia-Vidal, Opt. Commun. **200**, 1-7 (2001).

[35] H. F. Ghaemi, T. Thio, D. E. Grupp, T. W. Ebbesen and H. J. Lezec, Physical Review B **58**, 6779-6782 (1998).

[36] C. Genet and T. W. Ebbesen, Nature **445**, 39-46 (2007).

[37] W. L. Barnes, A. Dereux and T. W. Ebbesen, Nature **424**, 824-830 (2003).

[38] C. Genet and T. W. Ebbesen, Nature **445**, 39-46 (2007).

[39] R. Sergio G., Optical Properties of Nanostructured Metallic Systems, Berlin, Heidelberg: Springer Berlin Heidelberg, 37–75 (2012).

[40] C. Escobedo, Lab on a Chip, 2445 (Mar. 2013).

[41] A. Ameen, M. R. Gartia, A. Hsiao, T. Chang, Z. Xu and G. L. Liu, Journal of Nanomaterials **2015**, 21 (2015).

[42] J. Junesch and T. Sannomiya, ACS Appl. Mater. Interfaces **6**, 6322-6331 (2014).

[43] A. B. Dahlin, Analyst **140**, 4748-4759 (2015).

[44] F Przybilla and A Degiron and J-Y Laluet and C Genet and,T.W.Ebbesen, **8**, 458 (2006).

[45] File:Sketch of surface plasmon. png, Wikipedia, the free encyclopedia **20-MAR-2016**.

[46] T. W. Ebbesen, H. J. Lezec, H. F. Ghaemi, T. Thio and P. A. Wolff, Nature **391**, 667-669 (1998).

[47] Q. Chen and D. R. S. Cumming, Optics Express **18**, 14056-14062 (2010).

[48] Q. Chen, D. Das, D. Chitnis, K. Walls, T. D. Drysdale, S. Collins and D. R. S. Cumming, **7**, 695-699 (2012).

[49] N. G. Khlebtsov and L. A. Dykman, J. Quant. Spectrosc. Radiat. Transfer **111**, 1-35 (2010).

[50] Y. Xia, X. Xia, Y. Wang and S. Xie, MRS Bull **38**, 335-344 (2013).

[51] J. Henzie, J. Lee, M. H. Lee, W. Hasan and T. W. Odom, Annu. Rev. Phys. Chem. **60**, 147-165 (2009).

[52] W. CHEN and H. AHMED, Appl. Phys. Lett. **62**, 1499-1501 (1993).

[53] H. Im, S. H. Lee, N. J. Wittenberg, T. W. Johnson, N. C. Lindquist, P. Nagpal, D. J. Norris and S. Oh, Acs Nano **5**, 6244-6253 (2011).

[54] K. Kumar, H. Duan, R. S. Hegde, S. C. W. Koh, J. N. Wei and J. K. W. Yang, Nature Nanotechnology **7**, 557-561 (2012).

[55] N. C. Lindquist, P. Nagpal, K. M. McPeak, D. J. Norris and S. Oh, Reports on Progress in Physics **75**, 036501 (2012).

[56] B. Gates, Q. Xu, J. Love, D. Wolfe and G. Whitesides, Annual Review of Materials Research **34**, 339-372 (2004).

[57] B. Gates, Q. Xu, M. Stewart, D. Ryan, C. Willson and G. Whitesides, Chem. Rev. **105**, 1171-1196 (2005).

[58] Y. Xia and G. Whitesides, Annual Review of Materials Science **28**, 153-184 (1998).

[59] A. Boltasseva, Journal of Optics A-Pure and Applied Optics **11**, 114001 (2009).

[60] P. Nagpal, N. C. Lindquist, S. Oh and D. J. Norris, Science **325**, 594-597 (2009).

[61] A. Fernandez, H. T. Nguyen, J. A. Britten, R. D. Boyd, M. D. Perry, D. R. Kania and A. M. Hawryluk, Journal of Vacuum Science & Technology B **15**, 729-735 (1997).

[62] M. R. Gartia, A. Hsiao, A. Pokhriyal, S. Seo, G. Kulsharova, B. T. Cunningham, T. C. Bond and G. L. Liu, Advanced Optical Materials **1**, 68-76 (2013).

[63] S. Y. Lee, S. Kim, S. G. Jang, C. Heo, J. W. Shim and S. Yang, Anal. Chem. **83**, 9174-9180 (2011).

[64] M. R. Gartia, A. Hsiao, A. Pokhriyal, S. Seo, G. Kulsharova, B. T. Cunningham, T. C. Bond and G. L. Liu, Advanced Optical Materials **1**, 68-76 (2013).

[65] L. S. Jung, C. T. Campbell, T. M. Chinowsky, M. N. Mar and S. S. Yee, Langmuir **14**, 5636-5648 (1998).

[66] A. J. Haes, S. Zou, G. C. Schatz and R. P. Van Duyne, J Phys Chem B **108**, 109-116 (2004).

[67] K. A. Willets and R. P. Van Duyne, Annu. Rev. Phys. Chem. **58**, 267-297 (2007).

[68] A. Cattoni, P. Ghenuche, A. Haghiri-Gosnet, D. Decanini, J. Chen, J. Pelouard and S. Collin, Nano Lett. **11**, 3557-3563 (2011).

[69] M. E. Stewart, N. H. Mack, V. Malyarchuk, J. A. N. T. Soares, T. Lee, S. K. Gray, R. G. Nuzzo and J. A. Rogers, Proceedings of the National Academy of Sciences **103**, 17143-17148 (2006).

[70] Benjamin M Ross and Luke,P.Lee, Nanotechnology **19**, 275201 (2008).

[71] Y. Lu, G. L. Liu, J. Kim, Y. X. Mejia and L. P. Lee, Nano Letters **5**, 119-124 (2005).

[72] E. Prodan, C. Radloff, N. J. Halas and P. Nordlander, Science **302**, 419-422 (2003).

[73] T. W. Ebbesen, H. J. Lezec, H. F. Ghaemi, T. Thio and P. A. Wolff, Nature **391**, 667-669 (1998).

[74] J. Kim, Lab on a Chip **12**, 3611-3623 (2012).

[75] A. G. Brolo, R. Gordon, B. Leathem and K. L. Kavanagh, Langmuir **20**, 4813-4815 (2004).

[76] D. Sinton, R. Gordon and A. Brolo, Microfluidics and Nanofluidics **4**, 107-116 (2008).

[77] V. Kodoyianni, BioTechniques **50**, 32-40 (2011).

[78] C. J. Choi, I. D. Block, B. Bole, D. Dralle and B. T. Cunningham, IEEE Sensors Journal **9**, 1697-1704 (2009).

[79] C. F. Carlborg, K. B. Gylfason, A. Kazmierczak, F. Dortu, M. J. Banuls Polo, A. Maquieira Catala, G. M. Kresbach, H. Sohlstrom, T. Moh, L. Vivien, J. Popplewell, G. Ronan, C. A. Barrios, G. Stemme and d. W. van, **10**, 281-290 (2010).

[80] C. J. Choi, A. R. Belobraydich, L. L. Chan, P. C. Mathias and B. T. Cunningham, Anal. Biochem. **405**, 1-10 (2010).

[81] C. Escobedo, A. G. Brolo, R. Gordon and D. Sinton, Anal. Chem. **82**, 10015-10020 (2010).

[82] J. N. Lee, C. Park and G. M. Whitesides, Anal. Chem. **75**, 6544-6554 (2003).

[83] G. M. Whitesides, Nature **442**, 368-373 (2006).

[84] D. Qin, Y. Xia and G. M. Whitesides, Nature protocols **5**, 491-502 (2010).

[85] S. Bhattacharya, A. Datta, J. M. Berg and S. Gangopadhyay, J Microelectromech Syst **14**, 590-597 (2005).

[86] S. Satyanarayana, R. N. Karnik and A. Majumdar, J Microelectromech Syst **14**, 392-399 (2005).

[87] S. H. Lee, N. C. Lindquist, N. J. Wittenberg, L. R. Jordan and S. Oh, Lab on a Chip **12**, 3882-3890 (2012).

[88] A. De Leebeeck, L. K. S. Kumar, V. de Lange, D. Sinton, R. Gordon and A. G. Brolo, Anal. Chem. **79**, 4094-4100 (2007).

[89] M. Huang, B. C. Galarreta, A. E. Cetin and H. Altug, **13**, 4841-4847 (2013).

[90] S. Wu, K. Lee, A. Chiou, X. Cheng and P. Wei, **9**, 3532-3540 (2013).

[91] C Escobedo and S Vincent and A I K Choudhury and J Campbell and A G Brolo and D Sinton and,R.Gordon, J Micromech Microengineering **21**, 115001 (2011).

[92] J. Henzie, M. H. Lee and T. W. Odom, Nat Nano **2**, 549-554 (2007).

[93] A. A. Yanik, A. E. Cetin, M. Huang, A. Artar, S. H. Mousavi, A. Khanikaev, J. H. Connor, G. Shvets and H. Altug, Proceedings of the National Academy of Sciences **108**, 11784-11789 (2011).

[94] P. Nagpal, N. C. Lindquist, S. Oh and D. J. Norris, Science **325**, 594-597 (2009).

[95] S. Koynov, M. S. Brandt and M. Stutzmann, Appl. Phys. Lett. **88**, 203107 (2006).

[96] S. Kalem, P. Werner, O. Arthursson, V. Talalaev, B. Nilsson, M. Hagberg, H. Frederiksen and U. Sodervall, Nanotechnology **22**, 235307 (2011).

[97] C. Escobedo, Y. Chou, M. Rahman, X. Duan, R. Gordon, D. Sinton, A. G. Brolo and J. Ferreira, Analyst **138**, 1450-1458 (2013).

[98] Y. Sun and Y. Xia, Anal. Chem. **74**, 5297-5305 (2002).

[99] S. Lee, K. Lee, J. Ahn, J. Lee, M. Kim and Y. Shin, Acs Nano **5**, 897-904 (2011).

[100] K. Lee and M. A. El-Sayed, J Phys Chem B **110**, 19220-19225 (2006).

[101] E. M. Larsson, J. Alegret, M. Kall and D. S. Sutherland, Nano Letters **7**, 1256-1263 (2007).

[102] N. Verellen, P. Van Dorpe, C. Huang, K. Lodewijks, G. A. E. Vandenbosch, L. Lagae and V. V. Moshchalkov, Nano Letters **11**, 391-397 (2011).

[103] H. Im, J. N. Sutherland, J. A. Maynard and S. Oh, Anal. Chem. **84**, 1941-1947 (2012).

[104] A. Lesuffleur, H. Im, N. C. Lindquist and S. Oh, Appl. Phys. Lett. **90**, 243110 (2007).

[105] S. Y. Lee, S. Kim, S. G. Jang, C. Heo, J. W. Shim and S. Yang, Anal. Chem. **83**, 9174-9180 (2011).

[106] R. Lequin, Clin. Chem. **51**, 2415-2418 (2005).

[107] H. K. Hunt and A. M. Armani, Nanoscale **2**, 1544-1559 (2010).

[108] W. L. Barnes, A. Dereux and T. W. Ebbesen, Nature **424**, 824-830 (2003).

[109] S. H. Lee, T. W. Johnson, N. C. Lindquist, H. Im, D. J. Norris and S. Oh, Advanced Functional Materials **22**, 4439-4446 (2012).

[110] T. W. Ebbesen, H. J. Lezec, H. F. Ghaemi, T. Thio and P. A. Wolff, Nature **391**, 667-669 (1998).

[111] B. A. Sexton, B. N. Feltis and T. J. Davis, Sensors and Actuators A: Physical **141**, 471-475 (2008).

[112] G. L. Liu, J. C. Doll and L. P. Lee, Optic Express **13**, 8520-8525 (2005).

[113] A. Le, S. Kang, L. B. Thompson, S. S. Rubakhin, J. V. Sweedler, J. A. Rogers and R. G. Nuzzo, Journal of Physical Chemistry B **117**, 13069-13081 (2013).

[114] M. E. Stewart, J. Yao, J. Maria, S. K. Gray, J. A. Rogers and R. G. Nuzzo, Analytical Chemistry **81**, 5980-5989 (2009).

[115] G. Chen, N. Kawazoe and T. Tateishi, Open Biotechnology Journal **2**, 133-137 (2008).

[116] S. Kidambi, I. Lee and C. Chan, Advanced functional materials **18**, 294-301 (2008).

[117] S. Löfås, B. Johnsson, K. Tegendal and I. Rönnberg, Colloids and Surfaces B: Biointerfaces **1**, 83-89 (1993).

[118] S. Löfås, Pure and Applied Chemistry **67**, 829 (2009).

[119] M. Couture, L. S. Live, A. Dhawan and J. Masson, Analyst **137**, 4162-4170 (2012).

[120] S. Wu, P. Guo, W. Huang, S. Xiao and Y. Zhu, J. Phys. Chem. C **115**, 15205-15209 (2011).

[121] A. Hsiao, PhD dissertation (2014).

[122] A. J. Haes, S. Zou, G. C. Schatz and R. P. Van Duyne, J. Phys. Chem. B **108**, 109-116 (2004).

[123] M. D. Malinsky, K. L. Kelly, G. C. Schatz and R. P. Van Duyne, J. Am. Chem. Soc. **123**, 1471-1482 (2001).

[124] S. Wu, C. R. Moomaw, K. B. Tomer, J. R. Falck and D. C. Zeldin, J. Biol. Chem. **271**, 3460-3468 (1996).

[125] T. C. Delozier, G. E. Kissling, S. J. Coulter, D. Dai, J. F. Foley, J. A. Bradbury, E. Murphy, C. Steenbergen, D. C. Zeldin and J. A. Goldstein, Drug Metab. Dispos. **35**, 682-688 (2007).

[126] A. A. Spector, X. Fang, G. D. Snyder and N. L. Weintraub, Prog. Lipid Res. **43**, 55-90 (2004).

[127] D. C. Zeldin, J. Biol. Chem. **276**, 36059-36062 (2001).

[128] A. Nath, W. M. Atkins and S. G. Sligar, Biochemistry (N. Y.) **46**, 2059-2069 (2007).

[129] I. G. Denisov, Y. V. Grinkova, A. A. Lazarides and S. G. Sligar, J. Am. Chem. Soc. **126**, 3477-3487 (2004).

[130] F. P. Guengerich, Annu. Rev. Pharmacol. Toxicol. **39**, 1-17 (1999).

[131] F. P. Guengerich, Chem. Res. Toxicol. **21**, 70-83 (2008).

[132] J. Rittle and M. T. Green, Science **330**, 933-937 (2010).

[133] J. P. Whitlock J., S. T. Okino, L. Dong, H. P. Ko, R. Clarke-Katzenberg, Q. Ma and H. Li, FASEB J. **10**, 809-818 (1996).

[134] E. M. Gillam, T. Baba, B. R. Kim, S. Ohmori and F. P. Guengerich, Arch. Biochem. Biophys. **305**, 123-131 (1993).

[135] T. H. Bayburt and S. G. Sligar, Proc. Natl. Acad. Sci. U. S. A. **99**, 6725-6730 (2002).

[136] S. G. Sligar, Biochem. Biophys. Res. Commun. **312**, 115-119 (2003).

[137] A. Luthra, I. G. Denisov and S. G. Sligar, Arch. Biochem. Biophys. **507**, 26-35 (2011).

[138] A. V. Wells, P. Li, P. M. Champion, S. A. Martinis and S. G. Sligar, Biochemistry (N. Y.) **31**, 4384-4393 (1992).

[139] D. R. Davydov and J. R. Halpert, **4**, 1523-1535 (2008).

[140] E. M. Isin and F. P. Guengerich, J. Biol. Chem. **281**, 9127-9136 (2006).

[141] E. M. Isin and F. P. Guengerich, **392**, 1019-1030 (2008).

[142] L. Malic, D. Brassard, T. Veres and M. Tabrizian, **10**, 418-431 (2010).

[143] N. Ganesh, W. Zhang, P. C. Mathias, E. Chow, J. A. Soares, V. Malyarchuk, A. D. Smith and B. T. Cunningham, **2**, 515-520 (2007).

[144] M. Iqbal, M. A. Gleeson, B. Spaugh, F. Tybor, W. G. Gunn, M. Hochberg, T. Baehr-Jones, R. C. Bailey and L. C. Gunn, **16**, 654-661 (2010).

[145] V. S. Lin, K. Motesharei, K. P. Dancil, M. J. Sailor and M. R. Ghadiri, Science **278**, 840-843 (1997).

[146] M. Piliarik, H. Vaisocherova and J. Homola, Methods Mol. Biol. **503**, 65-88 (2009).

[147] R. L. Rich and D. G. Myszka, Curr. Opin. Biotechnol. **11**, 54-61 (2000).

[148] J. N. Anker, W. P. Hall, O. Lyandres, N. C. Shah, J. Zhao and R. P. Van Duyne, **7**, 442-453 (2008).

[149] C. L. Baciu, J. Becker, A. Janshoff and C. Sonnichsen, **8**, 1724-1728 (2008).

[150] A. J. Haes and R. P. Van Duyne, **379**, 920-930 (2004).

[151] T. R. Jensen, M. D. Malinsky, C. L. Haynes and R. P. Van Duyne, J Phys Chem B **104**, 10549-10556 (2000).

[152] G. Barbillon, J. -. Bijeon, J. Plain, l. C. de, P. -. Adam and P. Royer, Surf. Sci. **601**, 5057-5061 (2007).

[153] R. Gordon, D. Sinton, K. L. Kavanagh and A. G. Brolo, Acc. Chem. Res. **41**, 1049-1057 (2008).

[154] J. Ji, J. C. Yang and D. N. Larson, Biosens. Bioelectron. **24**, 2847-2852 (2009).

[155] H. Im, H. Shao, Y. I. Park, V. M. Peterson, C. M. Castro, R. Weissleder and H. Lee, Nat. Biotechnol. **32**, 490-495 (2014).

[156] A. A. Yanik, M. Huang, O. Kamohara, A. Artar, T. W. Geisbert, J. H. Connor and H. Altug, **10**, 4962-4969 (2010).

[157] A. J. Haes, S. Zou, J. Zhao, G. C. Schatz and R. P. Van Duyne, J. Am. Chem. Soc. **128**, 10905-10914 (2006).

[158] J. Zhao, A. Das, X. Zhang, G. C. Schatz, S. G. Sligar and R. P. Van Duyne, J. Am. Chem. Soc. **128**, 11004-11005 (2006).

[159] A. Das, J. Zhao, G. C. Schatz, S. G. Sligar and R. P. Van Duyne, Anal. Chem. **81**, 3754-3759 (2009).

[160] R. Karlsson and R. Stahlberg, Anal. Biochem. **228**, 274-280 (1995).

[161] S. Zeng, K. Yong, I. Roy, X. Dinh, X. Yu and F. Luan, **6**, 491-506 (2011).

[162] D. R. McDougle, A. Kambalyal, D. D. Meling and A. Das, J. Pharmacol. Exp. Ther. **351**, 616-627 (2014).

[163] S. Zelasko, A. Palaria and A. Das, Protein Expr. Purif. **92**, 77-87 (2013).

[164] W. L. Barnes, A. Dereux and T. W. Ebbesen, Nature **424**, 824-830 (2003).

[165] A. V. Zayats, I. I. Smolyaninov and A. A. Maradudin, Phys. Rep. **408**, 131-314 (2005).

[166] T. W. Ebbesen, H. J. Lezec, H. F. Ghaemi, T. Thio and P. A. Wolff, Nature **391**, 667-669 (1998).

[167] P. Berini, Adv. Opt. Photonics **1**, 484-588 (2009).

[168] T. Holmgaard, J. Gosciniak and S. I. Bozhevolnyi, Opt. Express **18**, 23009-23015 (2010).

[169] X. -. Zhang, A. Hu, J. Z. Wen, T. Zhang, X. -. Xue, Y. Zhou and W. W. Duley, Opt. Express **18**, 18945-18959 (2010).

[170] D. Dai and S. He, Opt. Express **17**, 16646-16653 (2009).

[171] D. Dai, Y. Shi, S. He, L. Wosinski and L. Thylen, Opt. Express **19**, 12925-12936 (2011).

[172] K. Leosson, **6**, 061801-061801 (2012).

[173] R. Zia, M. D. Selker, P. B. Catrysse and M. L. Brongersma, **21**, 2442-2446 (2004).

[174] J. A. Dionne, L. A. Sweatlock, H. A. Atwater and A. Polman, Phys. Rev. B **73**, 035407 (2006).

[175] J. A. Dionne, K. Diest, L. A. Sweatlock and H. A. Atwater, Nano Lett. **9**, 897-902 (2009).

[176] Z. Lu, W. Zhao and K. Shi, IEEE Photon. J. **4**, 735-740 (2012).

[177] A. J. Haes, W. P. Hall, L. Chang, W. L. Klein and R. P. Van Duyne, **4**, 1029-1034 (2004).

[178] A. J. Haes and R. P. Van Duyne, J. Am. Chem. Soc. **124**, 10596-10604 (2002).

[179] A. G. Brolo, R. Gordon, B. Leathem and K. L. Kavanagh, Langmuir **20**, 4813-4815 (2004).

[180] V. Canalejas-Tejero, S. Herranz, A. Bellingham, M. Moreno-Bondi and C. A. Barrios, **6**, 1005-1010 (2014).

[181] J. C. Sharpe, J. S. Mitchell, L. Lin, N. Sedoglavich and R. J. Blaikie, Anal. Chem. **80**, 2244-2249 (2008).

[182] T. W. Chang, X. H. Wang, A. Hsiao, Z. D. Xu, G. H. Lin, M. R. Gartia, X. R. Liu and G. L. Liu, **3**, 1397-1404 (2015).

[183] A. Hsiao, M. R. Gartia, T. W. Chang, X. Wang, P. Khumwan and G. L. Liu, **5**, 24-32 (2015).

[184] L. Plucinski, M. Ranjan Gartia, W. R. Arnold, A. Ameen, T. Chang, A. Hsiao, G. Logan Liu and A. Das, **75**, 337-346 (2016).

[185] A. Blanchard-Dionne, L. Guyot, S. Patskovsky, R. Gordon and M. Meunier, **19**, 15041-15046 (2011).

[186] E. D. Palik, Handbook of Optical Constants of Solids **ISBN: 978-0-12-544415-6** (1997).

[187] A. B. Dahlin, Analyst (2015).

[188] A. B. Dahlin, M. Mapar, K. Xiong, F. Mazzotta, F. Höök and T. Sannomiya, **2**, 556-564 (2014).

[189] H. Wei and H. Eilers, **70**, 459-465 (2009).

[190] T W H Oates and,A.Mücklich, Nanotechnology **16**, 2606 (2005).

[191] Y. Yagil, P. Gadenne, C. Julien and G. Deutscher, Physical Review B **46**, 2503-2511 (1992).

[192] D. D. Smith, Y. Yoon, R. W. Boyd, J. K. Campbell, L. A. Baker, R. M. Crooks and M. George, Journal of Applied Physics **86**, 6200-6205 (1999).

[193] V. E. Babicheva, R. Malureanu and A. V. Lavrinenko, **11**, 323-334 (2013).

[194] I. E. Tothill, Semin. Cell Dev. Biol. **20**, 55-62 (2009).

[195] Y. B. Guo, J. Y. Ye, C. Divin, B. H. Huang, T. P. Thomas, J. R. Baker and T. B. Norris, Anal. Chem. **82**, 5211-5218 (2010).

[196] M. Iqbal, M. A. Gleeson, B. Spaugh, F. Tybor, W. G. Gunn, M. Hochberg, T. Baehr-Jones, R. C. Bailey and L. C. Gunn, **16**, 654-661 (2010).

[197] V. S. Y. Lin, K. Motesharei, K. P. S. Dancil, M. J. Sailor and M. R. Ghadiri, Science **278**, 840-843 (1997).

[198] B. Liedberg, C. Nylander and I. Lundstrom, **4**, 299-304 (1983).

[199] H. Choo, M. K. Kim, M. Staffaroni, T. J. Seok, J. Bokor, S. Cabrini, P. J. Schuck, M. C. Wu and E. Yablonovitch, **6**, 837-843 (2012).

[200] A. Hosseini and Y. Massoud, **24**, 221-224 (2007).

[201] H. L. Duan and Y. M. Xuan, **43**, 1475-1480 (2011).

[202] C. Wadell, T. J. Antosiewicz and C. Langhammer, **12**, 4784-4790 (2012).

[203] Y. F. Liu and J. Kim, **148**, 23-28 (2010).

[204] A. Syahir, K. Kajikawa and H. Mihara, **7**, 1867-1874 (2012).

[205] D. Chanda, K. Shigeta, T. Truong, E. Lui, A. Mihi, M. Schulmerich, P. V. Braun, R. Bhargava and J. A. Rogers, **2** (2011).

[206] T. Cao, C. Wei and L. Zhang, **4**, 1526-1534 (2014).

[207] J. Junesch, T. Sannomiya and A. B. Dahlin, **6**, 10405-10415 (2012).

[208] A. B. Dahlin, M. Mapar, K. L. Xiong, F. Mazzotta, F. Hook and T. Sannomiya, **2**, 556-564 (2014).

[209] J. S. Macdonald, Semin. Oncol. **26**, 556-560 (1999).

[210] L. Hernandez, A. Espasa, C. Fernandez, A. Candela, C. Martin and S. Romero, Lung Cancer **36**, 83-89 (2002).

[211] M. J. Duffy, A. van Dalen, C. Haglund, L. Hansson, R. Klapdor, R. Lamerz, O. Nilsson, C. Sturgeon and O. Topolcan, Eur. J. Cancer **39**, 718-727 (2003).

[212] K. Bremer, S. Micus and G. Bremer, Eur. J. Cancer **31**, S262 (1995).

[213] R. Molina, J. Jo, X. Filella, G. Zanon, J. Pahisa, M. Mu noz, B. Farrus, M. L. Latre, C. Escriche, J. Estape and A. M. Ballesta, Breast Cancer Res. Treat. **51**, 109-119 (1998).

[214] Z. Mujagic, H. Mujagic and B. Prnjavorac, Med. Arh. **58**, 23-26 (2004).

[215] Z. Altintas, Y. Uludag, Y. Gurbuz and I. E. Tothill, Talanta **86**, 377-383 (2011).

[216] X. Chong, L. Liu, Z. Liu, S. Ma, J. Guo, Y. Ji and Y. He, **8**, 1185-1191 (2013).

[217] O. Livnah, E. A. Bayer, M. Wilchek and J. L. Sussman, Proceedings of the National Academy of Sciences of the United States of America **90**, 5076-5080 (1993).

[218] B. G. Nidumolu, M. C. Urbina, J. Hormes, C. S. S. R. Kumar and W. T. Monroe, Biotechnology progress **22**, 91-95 (2006).

APPENDIX

A.1. Replica molding protocols for nanoLCA device fabrication

1. Turn ON the UV cure oven at-least **10 min before** starting the replication process to warm up the lamp.
2. Make sure the vacuum pump is working fine
    a. Place the 4” Test Si Wafer on the mask holder
    b. Turn ON the vacuum pump
    c. Now try to move the wafer with tweezer to make sure it is secure with vacuum
    d. After Verification, turn OFF the vacuum pump
    e. Carefully remove the Si wafer by applying pressure from the back of the wafer
3. Now place your Glass Mold on the Mask Carrier and make sure it is flat and Mold is secure
4. Take the 1000µL Pipette and put the NOA-61 polymer on the center of the glass Mold
5. Repeat the previous step. The total NOA solution should be 2000µL
6. Now peal the protective cover from the PET sheet and carefully put the PET sheet on the polymer to avoid the bubble formation.
7. Wait until the polymer is completely spread between the PET sheet and glass Mold
8. Now carefully transfer the carrier with glass mold and PET sheet on the UV oven tray
    a. Please wear UV protective glasses

9. Open the UV shutter to expose the polymer and set the timer for 1m 30sec (90sec) and close the shutter.
10. Carefully remove the carrier with glass mold and PET sheet from the oven.
11. Take the glass mold (very carefully) with PET sheet and place it on the mask holder (as described in step 2) and make sure the vacuum is properly seal the Mold
12. Now slowly remove the PET sheet with CURED polymer from the glass Mold while the glass mold is vacuum sealed.
13. Remove the glass Mold (as described in step 2)
14. Clean the glass mold after ~20 replication to remove the organic products left of the mold from the polymer.
    a. Clean mold with Piranha (H_2SO_4:H_20_2 3:1) for 10min at 100ºC
    b. RCA 1 Clean (H_2O:NH_4OH:H_2O_2 5:1:1) for 10min at 75ºC (Optional)
    c. RCA 2 Clean (H_2O:HCl:H_2O_2 5:1:1) for 10min at 75ºC (Optional)
    d. Salinized the mold in silane solution for 30 min
    e. Wash with milli-Q water and dry with nitrogen

A.2. Multi-spectral system for transmission measurement of nanoLCA

1. Turn ON the system power
    a. Power the light source (press the white rectangle button on the metallic box to the left of the microscope)

b. Set the power level at 60 using the knob (maximum at 80 – the bulb will burn out quickly!)

c. Power the camera (power switch placed on top of the camera)

d. Power the Monochromator (power switch placed on the power brick at the back of the bench)

2. Measurement in Labview

a. Run the program and wait for the "Ready" light to turn green (You will have to wait a few minutes for the system to initialize)

b. Mirror = all wavelengths (broadband light), grating (set wavelength and set exposure time based on the image)

c. To designate a folder to save files, choose select folder, navigate to the folder, and select "**Current folder**" button

3. IN SCAN WINDOW

a. Start wavelength = 400 nm

b. End Wavelength = 800 nm

c. Increment Wavelength = 1 nm

4. Take the spectrum of the light source for normalization

a. Set exposure to 20msec for light spectrum (background)

b. Set magnification to 5 (optical lens magnification)

c. Make sure you have selected the select "**Current folder**"

d. Press “SCAN”

5. Sample transmission spectrum measurements

a. Set the position of the sample using EYE PIECE

b. Set Focus using Camera Image on screen

c. To set exposure try to guess the value where spectrum will not saturates

d. Specify the saturation value from the image around the peak wavelength.

e. Make sure intensity reading at the bottom of the image on screen does not exceed 2^8=256=8bit

f. Set exposure ~ 300 to 500ms

g. Set magnification 5 5

h. Make sure you have selected the select “**Current folder**”

i. Press “SCAN”

A.3. PDMS microfluidic channels using SU-8

In order to make microfluidic channels, first we need to make SU-8 mold with specific height, width and periodicity. In this particular case, 50um height, 500um width and 500um periodicity for each channel, SU-8 2025 is used. The photomask is designed using auto CAD software.

1. Spin coat SU-8 2025

a. 500rpm, 5sec (at rate: 100rpm/sec)

b. 3000rpm, 30sec (at rate: 300rpm/sec)

2. Pre-bake
    a. 65°C, 3min
    b. 95°C, 5min
3. Align mask and expose
4. Post-bake
    a. 65°C, 1min
    b. 95°C, 6min
5. Develop with SU-8 developer
6. Clean with IPA
7. Hard bake
    a. After the pattern is fully developed, hard bake the wafer at 150°C, 5min
8. PTFE Coating
    a. To protect the pattern for multiple usage, PTFE (Teflon film) is deposited using Deep RIE
9. Trichlorosilane treatment
    a. Incubate the wafer in the trichlorosilane solution for 30min for silane treatment to make the surface hydrophobic
10. Place the wafer with the channel pattern in the petri dish
11. Pore PDMS (10:1) solution on the wafer and place the petri dish in the degassing chamber to remove the bubbles

12. Leave the petri dish at room temperature overnight to cure the PDMS

13. Carefully remove the PDMS stamp from the wafer with imprinted channel pattern

A.4. NanoLCA device integration with PDMS (microfluidic channels) using UV-cure polymer

1. Prepare the PDMS pieces by making inlet and outlet holes on the channels
    a. -Clean with scotch tape
2. Prepare the nanoLCA devices by rinsing with IPA, Water, and then IPA
    a. -Blow dry with Nitrogen gun
3. Oxygen plasma both the PDMS pieces (feature side up) and the nanoLCA devices for 1 minute
4. Spin-coat a thin layer of UVc Polymer at 4000 RPM for 1 min on bare wafer
5. Stamp the treated PDMS pieces on the spin-coated UVc Polymer
6. Gently place the stamped PDMS pieces on the nanoLCA surface
    a. Tape the nanoLCA device down if it's not flat enough
7. Pre-cure by exposing for 300 seconds on 9999 x100 uJ/cm^2 UV lamp
8. Fully cure by exposing another UV lamp for 120 seconds
9. Age the bond by leaving it overnight at 60 degrees Celsius hot plate
10. After curing flow through IPA, Water, and IPA to clean the surface again
11. Insert the piping in the holes (inlet and outlets) to flow the solution through channels